October 2021

MAGNITUDE AND RATES OF AGRICULTURALLY-INDUCED SOIL EROSION IN THE MIDWESTERN UNITED STATES

Evan Thaler
University of Massachusetts Amherst

MAGNITUDE AND RATES OF AGRICULTURALLY-INDUCED SOIL EROSION IN THE MIDWESTERN UNITED STATES

Evan Thaler

MAGNITUDE AND RATES OF AGRICULTURALLY-INDUCED SOIL EROSION IN THE MIDWESTERN UNITED STATES

A Dissertation Presented

by

EVAN AUSTIN THALER

Submitted to the Graduate School of the
University of Massachusetts Amherst in partial fulfillment
of the requirements for the degree of

DOCTOR OF PHILOSOPHY

September 2021

Geosciences

MAGNITUDE AND RATES OF AGRICULTURALLY-INDUCED SOIL EROSION IN THE MIDWESTERN UNITED STATES

A Dissertation Presented

by

EVAN AUSTIN THALER

Approved as to style and content by:

_____
Isaac J. Larsen, Chair

_____
Qian Yu, Member

_____
Jonathan D. Woodruff, Member

_____
Marco Keiluweit, Member

_____
Stephen Burns, Department Head
Department Name

DEDICATION

To my family.

ACKNOWLEDGEMENTS

Properly thanking all the folks who have supported, encouraged, and helped me throughout my life and academic career would require more pages than the rest of my dissertation, so for now I will settle with the highlights. Special thanks to my fellow lab mates, Karin Lehnigk, Scott David, Jeffrey Kwang, Brendon Quirk, and Caroline Lauth Quarrier for keep me motivated to pursue science and for being tremendous fun to be around during long field and lab days. Without the expertise of Qian Yu, much of the work presented here would not have been possible. I am appreciative of her approachability, kindness, and advice for not only science but also career paths. Bill Clement has provided years of hilarious and insightful conversation on a large variety of topics; he genuinely cares about the success of each student, and his career advice has been crucial to beginning my career after my PhD. I am enormously grateful for my adviser Isaac Larsen. He has provided funding for my projects and my RA appointments and brought me on to work on a fruitful project. Isaac taught me how to become a better science writer and his encouragement to pursue remote sensing projects allowed me to dramatically expand my skillset.

I would be nothing without my family and friends. Nick Venti, Francois Lapointe, Brendan Moran, Laurel Jones, Timothy Dennis, Alex Harber, Keith Cox, and Ed Sherman have all been fantastically supportive—listening to me rant about my work and laughing at me when I got frustrated because analysis wasn't work out or when I couldn't get code to work. The light-heartedness of my friends has kept me grounded and happy throughout my time in school. Allison Swartz has been my sturdy lifeline throughout the last several years of my PhD. She always reminds me to go play outside when I am grumpy or frustrated and she constantly told me to "Never give up." I would not have made it to the end of this without her. My brother, Adam first got me interested in geology by taking me into caves and onto cliffs in the Ozarks. I would not have taken this career path without his influence. Finally, I am beyond grateful and fortunate for my wonderful parents, Cathy and Pat. Their support and encouragement have never wavered, even during time periods of my life when I was seemingly going nowhere. Everyone would have a better life if they had similarly amazing parents. I will never be able to properly express my gratitude for them.

The field work presented here required assistance from numerous people and agencies. They are fully named and thanked at the end of Chapter 5.

ABSTRACT

MAGNITUDE AND RATES OF AGRICULTURALLY-INDUCED SOIL EROSION IN THE MIDWESTERN UNITED STATES

SEPTEMBER 2021

EVAN AUSTIN THALER, B.S., UNIVERSITY OF ARKANSAS

M.S., UNIVERSITY OF ARKANSAS

Ph.D., UNIVERSITY OF MASSACHUSETTS AMHERST

Directed by: Professor Isaac J. Larsen

Fertile, agricultural productive soils are essential for producing food for a growing global population. Soil erosion diminishes soil quality, threatens food security by decreasing crop productivity, and degrades ecosystem health through increased rates of sedimentation and runoff. Despite decades and thousands of soil erosion studies, robust scalable methods for estimating the magnitude and rates of soil erosion have been elusive. In this dissertation, we develop a remote sensing method for quantifying the areal extent of historical loss in an agricultural landscape and provide a method for estimating the total thickness of soil loss and rates of historical soil loss in agricultural systems. First, we develop a remote sensing index for estimating soil organic carbon concentrations, which is the primary chemical difference between fertile A-horizon and less fertile B-horizon soils. Because the index only relies on the visible spectrum, it can be used to map soil organic carbon variability at the field scale. We test the index in a field in Iowa and find that the index predicts organic carbon concentrations with a root mean square error of 0.54%. Soil moisture can confound the spectral signature of soil organic carbon, but we quantify the effect of soil moisture on the remote sensing index by

measuring changes in the index for wet and dry soils with a range of soil organic carbon concentrations. Moisture has the largest influence on soils with higher soil organic carbon concentrations than soils with lower organic carbon concentrations. We also performed a laboratory experiment to quantify the time for the surface layer of a soil to dry and find that the surface dries after ~27 hours, indicating that moisture has little influence on the spectral signal of the surface soil around one day following precipitation. We use the soil organic carbon index calculated from high-resolution satellite imagery to map soil organic carbon in agricultural fields at 28 locations throughout the midwestern U.S. We then used high-resolution satellite and LiDAR data to develop a relationship between A-horizon loss and topographic curvature, and then use topographic data to scale-up soil loss predictions across 3.9×10^5 km^2 of midwestern U.S. Our results indicate that 35±11% of the cultivated area has lost A-horizon soil, and that prior estimates of soil degradation from soil survey-based methods have significantly underestimated A-horizon soil loss. Finally, we quantify the historically averaged soil erosion rate and the total depth of soil loss throughout the Midwestern U.S. In the Midwestern U.S., erosion has caused native prairie remnants to become perched above surrounding farmland, providing an opportunity to measure historical soil loss. We used high-resolution topographic surveys conducted across erosional escarpments at the boundary between 20 prairies and adjacent fields and show the median depth of soil loss ranges from 0.04-0.69 m, corresponding to erosion rates of 0.2–4.3 mm yr^{-1}.

TABLE OF CONTENTS

LIST OF TABLES

Table Page

LIST OF FIGURES

Figure Page

CHAPTER 1

INTRODUCTION

Fertile, agricultural productive soils are essential for producing food for a growing global population (Amundson et al., 2015). Conventional agricultural practices degrade soil quality by eroding the carbon-rich soil which is the foundation of agricultural productivity (Montgomery, 2007). Widespread adoption of synthetic fertilizer application offsets declines in crop productivity caused by decreased soil fertility (Tilman et al., 2002); however, excessive fertilizer use causes pollution of hydrologic systems, harming ecosystems and negatively impacting human health (Pimentel et al., 1995; Schilling and Spooner, 2006). The global soil organic carbon reservoir is three times the atmospheric reservoir (Pries et al., 2017) and given that nearly 40% of the world's land is used for agriculture (Foley et al., 2005), understanding the dynamics of soil carbon mobilization within agricultural systems is vital to understanding the global carbon cycle (Lal, 2004). Despite the negative consequences of soil erosion on ecosystems services and human societies, robust methods for quantifying soil erosion at various spatial scales have been elusive (Poesen, 2017).

Assessments of soil erosion in the U.S. rely on models developed from experimental erosion plots and field surveys (Agriculture, 2018). The accuracy of scaling estimates from surveys and plot experiments has been debated (Nearing et al., 2000; Trimble and Crosson, 2000) and these approaches do not provide insight on the overall magnitude of post-cultivation erosion. In this dissertation, we fill a major gap in soil erosion research by developing methods for quantifying the areal extent, the total thickness of soil loss, and rates of historical soil loss in agricultural systems.

Remote sensing analysis has been demonstrated to be a rapid and powerful approach to estimating physical and chemical soil properties at various spatial scales (Stoner et al., 1986; Rossel et al., 2006; Gomez et al., 2008), yet a remote sensing approach for estimating soil organic carbon concentrations at the scale of a single agricultural field has not been developed. In Chapter 2, we use the USDA Rapid Carbon Assessment database of soil organic carbon and hyperspectral measurements from soil samples collected across the U.S. (Staff, 2013; Wills et al., 2014) to develop a new remote sensing index for soil organic carbon, which we term the soil organic carbon index (SOCI). The index is based only on wavelengths in the visible spectrum and predicts soil organic carbon for the nationwide dataset with a root mean squared error (RMSE) of 1.5% organic carbon. The index performs as well or better than previous indices for soil organic carbon, but unlike other indices, the SOCI relies only on the visible spectrum. Hence it can be calculated from any true color image, which are often high spatial resolution. We tested the transferability of the SOCI from laboratory to satellite-based sensors by applying the index to a satellite image of a bare soil field in Iowa where 228 soil samples we collected and find that the SOCI predicts soil carbon with a RMSE of 0.54%, indicating that the SOCI provides the ability to assess field-scale variability in soil organic carbon concentrations.

Because increases in either soil organic carbon or soil moisture cause the spectral reflectance of soil to decrease, soil moisture can confound the spectral signature of soil organic carbon (Minasny et al., 2011) and can therefore decrease the effectiveness of the SOCI to estimate organic carbon concentrations using imagery. In Chapter 3 we quantify the effect of soil moisture on the SOCI by measuring changes in the SOCI for wet and

dry soils with a range of soil organic carbon concentrations. We find that moisture has a larger influence on soils with higher soil organic carbon concentrations than on soils with lower soil organic carbon concentrations. We also performed an infiltration experiment to quantify the time for the surface layer of a soil column with high organic carbon concentrations, collected from a hollow in an agricultural field in Iowa, and low organic carbon concentrations, collected from a hilltop in the same field, to return to dry SOCI value after being wetted. For both soils, we find that within 27 hours, the soil surface returned to the dry SOCI values, indicating that any effect of soil moisture is removed from the soil surface as soon as one day following precipitation. Hence, if imagery is acquired more than one day following a precipitation event, then the SOCI can be used to estimate organic carbon concentrations from that image.

With the ability provided by the SOCI to map in-field variations in soil organic carbon concentrations, we estimated the extent of degraded soil in the Midwestern U.S. In Chapter 4, we used the SOCI calculated from high-resolution satellite imagery to map soil organic carbon in agricultural fields at 28 locations throughout the midwestern U.S. We relate the soil organic carbon concentrations to the soil horizon exposed at the surface using soil organic carbon, SOCI, and horizon data from the RaCA. We use high-resolution satellite and LiDAR data to develop a relationship between A-horizon loss and topographic curvature, and then use topographic data to scale-up soil loss predictions across 3.9×10^5 km^2 of midwestern U.S. Our results indicate that 35±11% of the cultivated area has lost A-horizon soil, and that prior estimates of soil degradation from soil survey-based methods have significantly underestimated A-horizon soil loss. The analysis and methodology presented in Chapter 4 provided the first quantitative estimate of the extent

of A-horizon loss in the Midwestern U.S. Further, the method is the first scalable approach to quantifying soil loss across various spatial scales.

The estimates of soil loss provided by the remote-sensing analysis presented in Chapter 4 provides an estimate of the areal extent of soil loss but does not provide information on the depth of soil loss. In Chapter 5, we leverage remnants of the anthropogenically unaltered landscape to quantify the historically averaged soil erosion rate and the total depth of soil loss throughout the Midwestern U.S. In the Midwestern U.S., agriculturally accelerated soil erosion has caused native prairie remnants, which erode at slower geologic rates, to become perched above surrounding farmland, generating an erosional escarpment at the boundary between the prairies and the fields. The erosional escarpments provide a record of the magnitude of soil loss that has occurred since cultivation began. We used high-resolution topographic surveys conducted across erosional escarpments at the boundary between 20 prairies and adjacent fields and show the median depth of soil loss ranges from 0.04-0.69 m, corresponding to erosion rates of 0.2–4.3 mm yr^{-1}. The results presented in Chapter 5 provides the first estimates of the historically averaged soil erosion rates in the Midwestern U.S since the initiation of cultivation in the mid-1800s. Further, by comparing the historical erosion rates to modern erosion rates predicted by the USDA, we find that >60% of the cultivated land in the Midwestern U.S. is currently eroding at rates greater than the historical average, indicating that greater soil conservation measures must be taken to decrease soil erosion rates and preserve the remaining soil.

In the final chapter of this dissertation (Chapter 6), we provide a brief summary of the main findings of the overall work and provide closing thoughts on the measures that

must be taken to reduce soil erosion and conserve soil. Chapter 2 of this dissertation has been published in the *Soil Science Society of American Journal* (Thaler et al., 2019) with my co-authors Isaac J. Larsen and Qian Yu. The results from Chapter 4 have been published in the *Proceedings of the National Academy of Sciences* (Thaler et al., 2021) also with my co-authors Isaac J. Larsen and Qian Yu. A manuscript based on the results in Chapter 5 and co-authored by Isaac J. Larsen, Jeffrey S. Kwang, Brendon J. Quirk, and Caroline A. Lauth Quarrier has been submitted to *Science Advances*.

CHAPTER 2

A NEW INDEX FOR REMOTE SENSING OF SOIL ORGANIC CARBON BASED SOLELY ON VISIBLE WAVELENGTHS

Abstract

Remote sensing is a powerful method for mapping soil properties, such as soil organic carbon (SOC), a key property of soil quality. Spectral remote sensing indices that rely on shortwave-infrared (SWIR) or near-infrared (NIR) wavelengths have been developed to quantify spatial patterns in SOC. However, the application of SWIR- and NIR-based indices for quantifying fine scale patterns of SOC is limited due to the requirement of high-resolution multi- or hyperspectral imagery. Visible wavelengths, however, are measured by virtually all sensors, often at high resolution; hence development of a visible wavelength-based index can greatly increase the ability to remotely estimate SOC. Here we develop such an index by assessing the relationship between laboratory measured SOC and spectral reflectance using 7,916 SOC and hyperspectral measurements from the nationwide USDA Rapid Carbon Assessment. Our new soil organic carbon index (SOCI) predicts SOC concentrations for the 7,916 samples with a root mean square error (RMSE) of 1.5%, which is comparable to predictions from the SWIR/NIR ratio (RMSE=1.3%) and outperforms the predictions of an index based on NIR and Red wavelengths (RMSE=2.8%). We applied the index to a high-resolution satellite image and tested the ability of the image-based SOCI to predict measured SOC concentrations for a plowed field in Iowa; regression models with and without local calibration data well-predict measured SOC, with RMSE values of ~0.5%. Given the widespread availability of

imagery with spectral data in the visible wavelengths, there is potential to use the SOCI to address a range of soil-agronomic problems.

Introduction

Soil organic carbon (SOC) is vital for soil fertility and agricultural productivity (Reeves, 1997; Lal, 2005). Soil erosion causes declines in SOC, which result in economic losses due to decreased crop productivity (West and Post, 2002; Lal, 2004) and the need to supplement degraded soils with chemical fertilizers (Pimentel et al., 1995). The influence of SOC on agricultural productivity has, in part, driven interest in the development of digital soil mapping techniques (Frazier and Cheng, 1989; Chen et al., 2000; Mishra et al., 2009; Mulder et al., 2011; Dogan and Kılıç, 2013; Bachofer et al., 2015). Digital soil mapping techniques use diffuse reflectance spectroscopy, which has been demonstrated to accurately and non-destructively relate spectral reflectance to soil properties (Bachofer et al., 2015; Ben-Dor and Banin, 1995; Gomez et al., 2008; Peón et al., 2017). Digital soil mapping has been used to qualitatively assess the degree of soil degradation in agricultural landscapes by categorizing the degradation into severity classes (Chikhaoui et al., 2005) and to quantitatively predict SOC concentrations (Frazier and Cheng, 1989; Chen et al., 2000; Rossel et al., 2006; Gomez et al., 2008). The use of spectrographic analysis to digitally map soil characteristics has been utilized in precision agriculture, as rapid, field-scale assessments of soil properties allow farmers to efficiently identify and treat soils in which nutrients are limited (Mulla, 2013).

Linear regression models developed from laboratory hyperspectral reflectance and chemical measurements of soil samples have often been used to calibrate spectral indices

for predicting soil properties based on soil color (Bachofer et al., 2015; Ben-Dor and Banin, 1995; Frazier and Cheng, 1989; Gomez et al., 2008; Mulder et al., 2011; Nanni and Demattê, 2006). Soil color often varies due to changes in SOC and soil moisture (Escadafal, 1993; Schulze et al., 1993). Soils with higher SOC concentrations are typically darker-colored and therefore have lower spectral reflectance than soils with lower SOC content (Rossel et al., 2006). Similarly, increasing soil moisture causes soils to appear darker, as the reflectance of incident radiation in the visible spectrum uniformly decreases with increasing moisture (Weidong et al., 2002; Nocita et al., 2013). However, unlike reflectance changes due to SOC content, the uniform decrease in reflectance across the visible wavelengths with increasing soil moisture indicates that use of band ratios can remove the impact of soil moisture on spectral reflectance (Stoner and Baumgardner, 1981; Nocita et al., 2013).

Wavelengths in the short-wave infrared (SWIR, 1300-2500 nm) and near infrared (NIR, 700-1300 nm) regions have been shown to be sensitive to SOC, with the reflectance in both regions decreasing with increasing SOC (Bartholomeus et al., 2008). Several spectral indices that are sensitive to changes in SOC have been derived using laboratory and field measurements of SWIR and NIR reflectance (Rossel et al., 2006; Peón et al., 2017). For example, the band ratio SWIR/NIR (1608 nm / 833 nm) was correlated with SOC (R^2=0.98) for 32 soil samples and used to examine the extent of SOC-rich topsoil erosion in the Palouse region of eastern Washington (Frazier and Cheng, 1989). For most satellite sensors, measurements of wavelengths in the SWIR region is limited in pixel resolution or, where SWIR is measured at high pixel resolution, in the coverage and availability of images. Hence there are limitations to implementing

SWIR-based indices at fine-spatial scales. Because visible wavelengths are measured by most sensors and can rapidly be measured at the field-scale using satellites, unmanned aerial vehicles (drones), or other platforms, the development of a SOC index based solely on the visible spectrum would allow variations in SOC to be efficiently assessed without the use of multispectral or hyperspectral imagery that include data in the SWIR-NIR wavelengths.

Spectral methods that use combinations of visible (VIS, 400-700 nm) and NIR bands (Chen et al., 2000; Peón et al., 2017) have been developed for small geographical areas but have not been calibrated using data from larger spatial scales. For example, image intensity values in the VIS wavelengths calculated from an aerial image of a 115 ha field in Georgia were used to develop a multiple linear regression model that predicted SOC with an R^2 of 0.93; however the regression was calibrated using only 28 soil samples (Chen et al., 2000). A spectral index (SI) with the form of the normalized difference vegetation index ($SI_{1001\text{-}679\ nm}$= (1001 nm - 679 nm)/ (1001 nm + 679 nm)), which is typically used in phenological studies of vegetation, has been shown to be useful as a SOC index (Peón et al., 2017). A maximum R^2 value of 0.56 was observed for the correlation between SOC and the $SI_{1001\text{-}679\ nm}$ calculated from satellite hyperspectral measurements from 39 soil samples collected in northwestern Spain (Peón et al., 2017). Though SOC has been shown to be well-correlated with the SWIR/NIR and $SI_{1001\text{-}679\ nm}$ indices, such studies have used a relatively small number of soil samples collected from a limited geographic extent. Hence the utility of such indices at regional to global scales remains untested.

In addition to using diffuse reflectance spectroscopy to develop spectral indices, the application of multivariate statistical techniques or machine learning algorithms, such as principal component analysis (Chang et al., 2001), regression trees (Peón et al., 2017), support vector machines (Aldana-Jague et al., 2016), artificial neural networks (Rossel and Behrens, 2010), and partial least squares regression (Rossel et al., 2006) are also used for SOC estimation. For example, artificial neural networks were used with hyperspectral data from ~20,000 soil samples collected by the USDA Rapid Carbon Assessment (RaCA) to develop models for predicting SOC (Soil Survey Staff, 2013). Incorporating land use, master horizon, and textural class information into the models resulted in SOC predictions with RMSE values between 0.5 and 1.5% (Wijewardane et al., 2016). However, transferring such multivariate statistical models between sensors is complex because wavelength position, bandwidth, and number of bands vary between sensors (Li et al., 2012). Multivariate and machine learning techniques are hence specific to the sensors for which they are derived and require re-calibration for use with different sensors (Bartholomeus et al., 2008).

Although multiple approaches have been used to predict SOC from spectral data, there remains a need for development of a spectral index for SOC, based on wavelengths in the visible range, that can be applied to multi- and hyperspectral imagery at high-spatial resolution (Peón et al., 2017). Here we use SOC measurements and hyperspectral reflectance data for soil samples collected across the United States to compare a newly-developed index that relies only on the VIS wavelengths to the SWIR/NIR and the $SI_{1001-679\ nm}$ indices. We then validate the new index using a satellite image to generate a map of

predicted SOC values for a field in Iowa and compare the predictions against measured SOC concentrations.

Data and Methods

Laboratory data

The RaCA, undertaken by the Soil Science Division of the USDA National Resource Conservation Service, collected 144,833 soil samples to 1 m depth at 6,148 sites in the conterminous United States (Soil Survey Staff, 2013; Wills et al., 2014). Soil samples were air-dried, sieved to < 2 mm, and hyperspectral reflectance was measured from 350-2500 nm for all samples using an ASD Labspec Spectrometer (Analytical Spectral Devices, Inc., PANalytical NIR Excellent Center). SOC concentration was measured for a subset of samples as the difference between total carbon and inorganic carbon (Wijewardane et al., 2016). To evaluate the ability of existing SOC indices and a new index based solely on the visible spectrum to predict SOC, we used 7,916 measurements of SOC and hyperspectral reflectance from the RaCA for mineral soil horizons (A- and B- horizons) from 2,673 locations within the conterminous United States (Fig. 1).

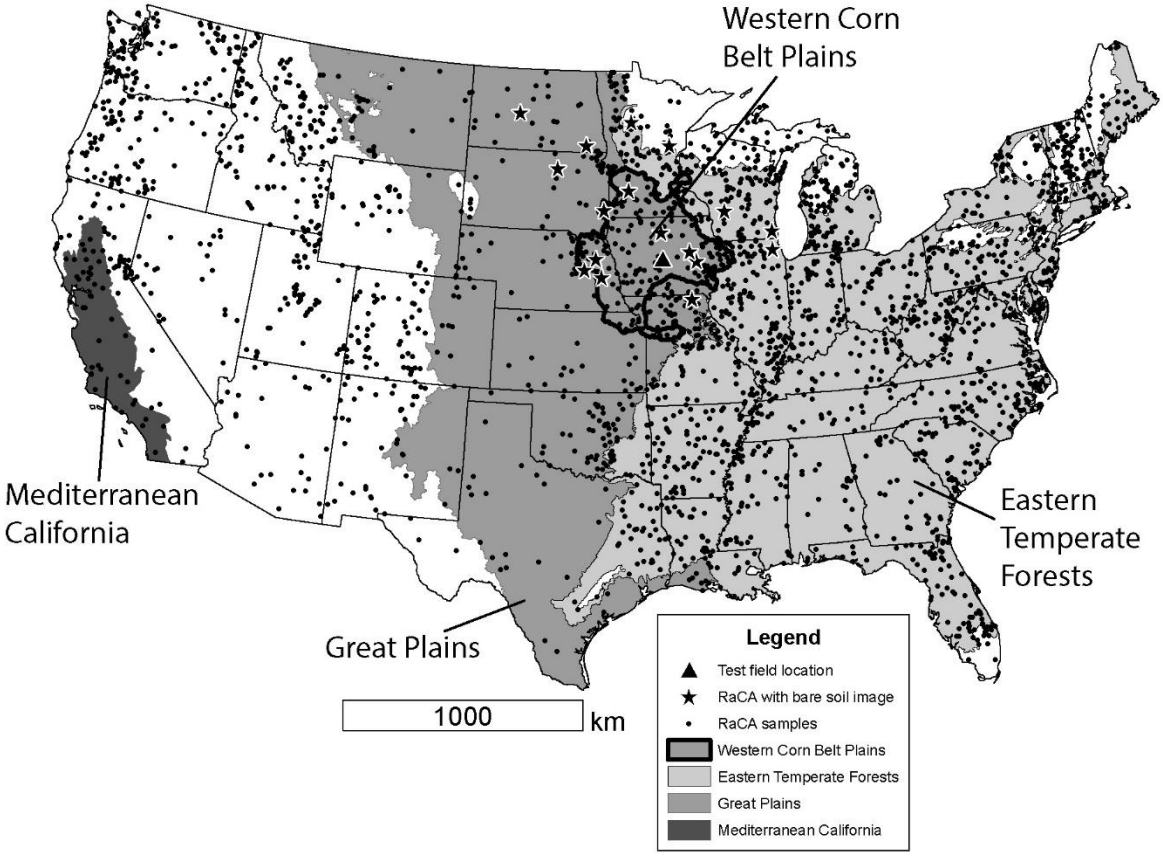

Fig. 2.1 Map of U.S. Department of Agriculture Rapid Carbon Assessment (RaCA) soil sample locations and U.S. Environmental Protection Agency ecoregions: The Great Plains, Mediterranean California, and Eastern Forests Level I ecoregions and the Level III Western Corn Belt Plains region. RaCA sample locations are shown as black circles. Black stars are locations of calibration sites where RaCA samples were collected and plowed, bare soil is exposed in a WorldView-2 (DigitalGlobe, Longmont, CO; https://www.digitalglobe.com) satellite image. The field where 228 soil samples were measured for SOC (Li et al., 2018) is marked as a black triangle.

Development of a new spectral index and comparison with existing indices

We developed a new soil organic carbon index (SOCI) by performing linear regression between combinations of visible bands and SOC using the national RaCA soil sample data and choosing a combination of bands that minimized the RMSE (Table S1). We term the band combination that yielded the minimum RMSE value the SOCI:

$$SOCI = \frac{Blue}{Red \cdot Green} \qquad (1).$$

We used reflectance at 478 nm, 546 nm, and 659 nm, for Blue, Green, and Red, respectively, which correspond to the center wavelengths of the WorldView-2 sensor.

Soil properties, such as SOC concentrations, exhibit high degrees of spatial correlation (Cambardella et al., 1994; Mishra et al., 2009), hence the strength of relationships between remote sensing indices and measured SOC values likely varies with spatial scale between and within regions due to differences in predominant soil forming factors. To assess the role of scale and regional variability we examined the coefficient of determination (R^2) and root mean squared error (RMSE) between measured SOC and the SOCI, the SWIR/NIR index, and the $SI_{1001\text{-}679\ nm}$ for RaCA soil sample datasets of varying spatial extent: the conterminous U.S., three large and predominantly agricultural U.S. Environmental Protection Agency Level I ecoregions (Great Plains, Eastern Temperate Forests, and Mediterranean California), and 54 Level III ecoregions nested within the larger Level I ecoregions (Omernik, 1987).

Application of the new index to SOC mapping using satellite imagery

We used a 1.9 m pixel resolution WorldView-2 satellite image of a 15 ha agricultural field in Iowa to assess the ability of the SOCI to predict spatial patterns in SOC. Within the field, previous workers collected 228 soil samples to a 30 cm depth (Li et al., 2018). The samples were sieved to < 2 mm, further ground to a powder, and the depth-averaged SOC concentrations for the 30 cm profile were measured (Li et al., 2018). The image was acquired on 4 May 2010, when the field was plowed and lacked both crop residue and crop cover. We used the SOCI to predict SOC within the field using two methods. First, we used a subset of the measurements from the field to locally calibrate a relationship between the SOCI and SOC and then used the local calibration to predict measured SOC values. Second, we developed a regional calibration between the SOCI and SOC using RaCA data from the Western Corn Belt Plains Level III ecoregion, where the agricultural field is located, and used the regional calibration to predict SOC.

Local calibration

To determine if radiometric correction of the image is necessary for the index to be applied, we calculated the SOCI from both the uncorrected, raw 11-bit digital number (DN) image and from reflectance data derived by radiometrically calibrating the image. The image was radiometrically corrected to derive reflectance using an empirical line calibration method (Smith and Milton, 1999). A deep, clear water pixel and an aluminum metal roof pixel were identified and calibrated against reflectance values for distilled water and aluminum metal roofing from the ASTER spectral library (Baldridge et al., 2009). The SOCI was then calculated from the reflectance data. For the DN image and the reflectance image, we extracted the SOCI from each pixel with a corresponding soil

sample. We predicted SOC for each sample location by developing a linear regression between SOC and the SOCI using a calibration dataset of 45 random samples (20%) of the measured SOC concentrations and SOCI values from both the DN and reflectance images. We then used the calibration to predict SOC for the remaining 183 pixels where samples were collected.

Regional calibration

The RaCA calibration data are based on laboratory spectral measurements, rather than satellite-based measurements, hence we first needed to account for offset between the satellite- and laboratory-derived indices, which arise due to different measurement conditions, such as sieving of laboratory samples and imperfect radiometric correction. We scaled the satellite-derived index to the laboratory-derived index by developing a linear regression relationship between satellite- and laboratory-derived SOCI using reflectance data from 16 locations where an RaCA sample was collected from a location with a WorldView-2 satellite image with bare soil at the sample site.

SOCI data derived from imagery predict SOC concentrations for the soil surface, but the measured SOC values are an average concentration for a depth interval extending from the soil surface to a depth of 30 cm (Li et al., 2018). To compare the SOC predictions from the satellite-derived SOCI values with the measured SOC values, we scaled the predicted SOC values to an average SOC concentration for the upper 30 cm of the soil profile by assuming an exponential depth-distribution of SOC (Mishra et al., 2009):

$$SOC = ae^{bz} \quad (2)$$

where *a* and *b* are fitted parameters describing the surface SOC concentration and the rate of decay, respectively, and *z* is depth within the profile. The depth at which the average SOC concentration occurs is described by 1/*b* (Lilliefors, 1969). The *a* and *b* parameters are not available for the field in Iowa, so we determined them by fitting equation (2) to 15 SOC-depth profiles with ≥ five SOC-depth measurements at RaCA sites in the Western Corn Belt Plains Level III ecoregion. We used the average of the *a* and *b* parameters from all profiles to calculate the average SOC for the upper 30 cm of the soil. The surface- and depth-averaged predictions were both compared against the depth-averaged measurements. All statistical analyses were performed using the NumPy (version 1.14.3) and SciPy (version 0.18.1) packages in Python 3.

Results

Index validation using laboratory spectral data

For the nationwide dataset of SOC measurements, the SOCI, SWIR/NIR, and $SI_{1001\text{-}679\ nm}$ indices are similarly correlated with SOC. The SOCI has a power-law relationship with SOC (Fig. 2a) and has an R^2 of 0.35 and RMSE of 1.5%. The SWIR/NIR index also has a power law relationship with SOC (Fig. 2b) where the R^2 is 0.17 and the RMSE is 1.2%. The $SI_{1001\text{-}679\ nm}$ is exponentially correlated with SOC (Fig. 2c) with R^2 and RMSE 0.21 and 2.8% respectively. (Table 1).

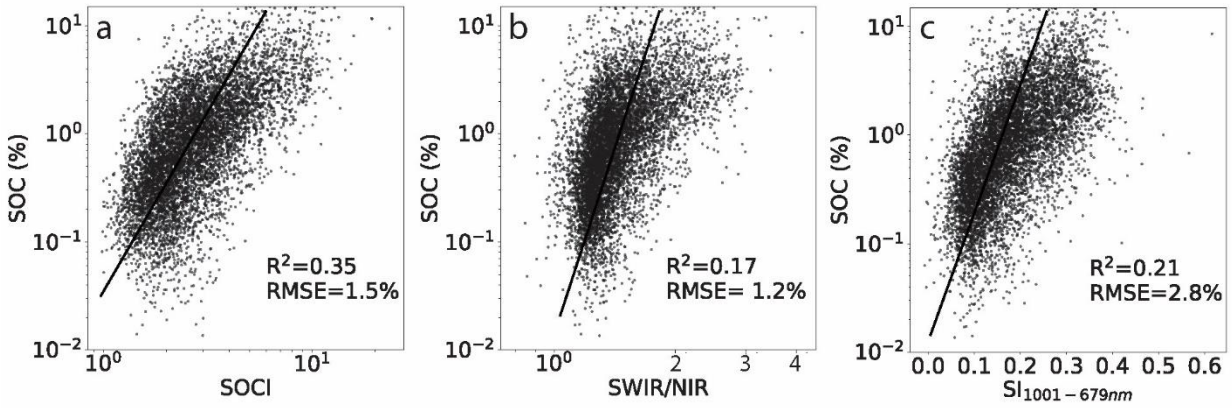

Fig. 2.2 Spectral indices versus soil organic carbon (SOC) for the nationwide dataset (*n*=7,916) for a) the SOCI developed in this study, b) the SWIR/NIR index, and c) the $SI_{1001\text{-}679\ nm}$. The black lines show the regression for each index.

Table 2.1 Equations, correlation coefficients, and RMSE values for SOC prediction using the three spectral indices for the national dataset, three major U.S. agricultural Level I ecoregions, and the Western Corn Belt Level III ecoregion.

Spectral Index	**Relationship with soil organic carbon (SOC) using national data**	**Nationwide n=7916**		**Level I ecoregions**						**Level III ecoregion†**	
				Great Plains n=1767		**Eastern Forests n=4243**		**Mediterranean California n=153**		**Western Corn Belt Plains n=595**	
		R^2	RMSE	R^2	RMSE	R^2	RMSE	R^2	RMSE	R^2	RMSE
SOCI	$SOC=0.3\cdot SOCI^{1.4}$	0.35	1.5%	0.43	1.4%	0.31	1.5%	0.36	1.8%	0.54	1.0%
SWIR/NIR	$SOC=0.7\cdot SWIR/NIR^{2.2}$	0.17	1.2%	0.36	0.98%	0.13	1.3%	0.26	1.3%	0.46	1.4%
$SI_{1001\text{-}679nm}$	$SOC=1.6\cdot e^{3.7\cdot SI1001\text{-}679nm}-1.7$	0.21	2.8%	0.29	3.3%	0.18	4.1%	0.31	2.9%	0.42	2.7%

†Data from all 54 Level III ecoregions are shown in Table A2

Results from the Level I ecoregions indicate there were higher correlation coefficients and lower errors for the Great Plains and Mediterranean ecoregions relative to the U.S.-wide data (Table 1). The respective Great Plains and Mediterranean California Level I ecoregion RMSE values for the SOCI were 1.4% and 1.8%, which were comparable to the SWIR/NIR index values of 0.98% and 1.3%, both which were lower than the $SI_{1001\text{-}679\ nm}$ values of 3.3% and 4.1%. Results from the Eastern Temperate Forests Level I ecoregion were comparable to values from the nation-wide analysis; RMSE values were similar for the SOCI (1.5%) and were slightly higher for the SWIR/NIR index (1.3%) and the value for the $SI_{1001\text{-}679\ nm}$ index was higher (4.1%). Generally, the results for the 54 Level III ecoregions had lower errors and higher correlations than the Level I ecoregions (Table S2). RMSE values for SOCI (0.42-2.6%) were comparable to the SWIR/NIR values (0.43-1.9%) and both were lower than those from the $SI_{1001\text{-}679\ nm}$ (0.60-9.1%) (Fig 3; Table S2).

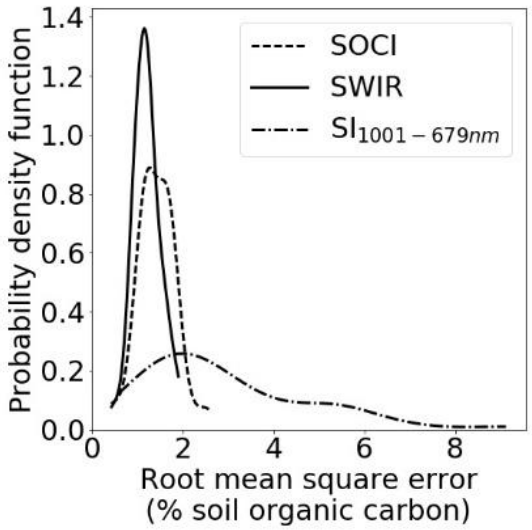

Fig. 2.3 Probability density function of RMSE values for the three indices calculated for each of the 54 Level III ecoregions.

Index validation using satellite image

Local calibration

The calibration dataset derived from the SOC measurements in the field (Fig. 4a) and the SOCI calculated from the DN image (Fig. 4b) predicted SOC with a RMSE of 0.53% (Fig. 4c). Similarly, when the SOCI was calculated from the reflectance image, the local calibration (Fig. 4d) predicted SOC with a RMSE of 0.54% (Fig. 4e).

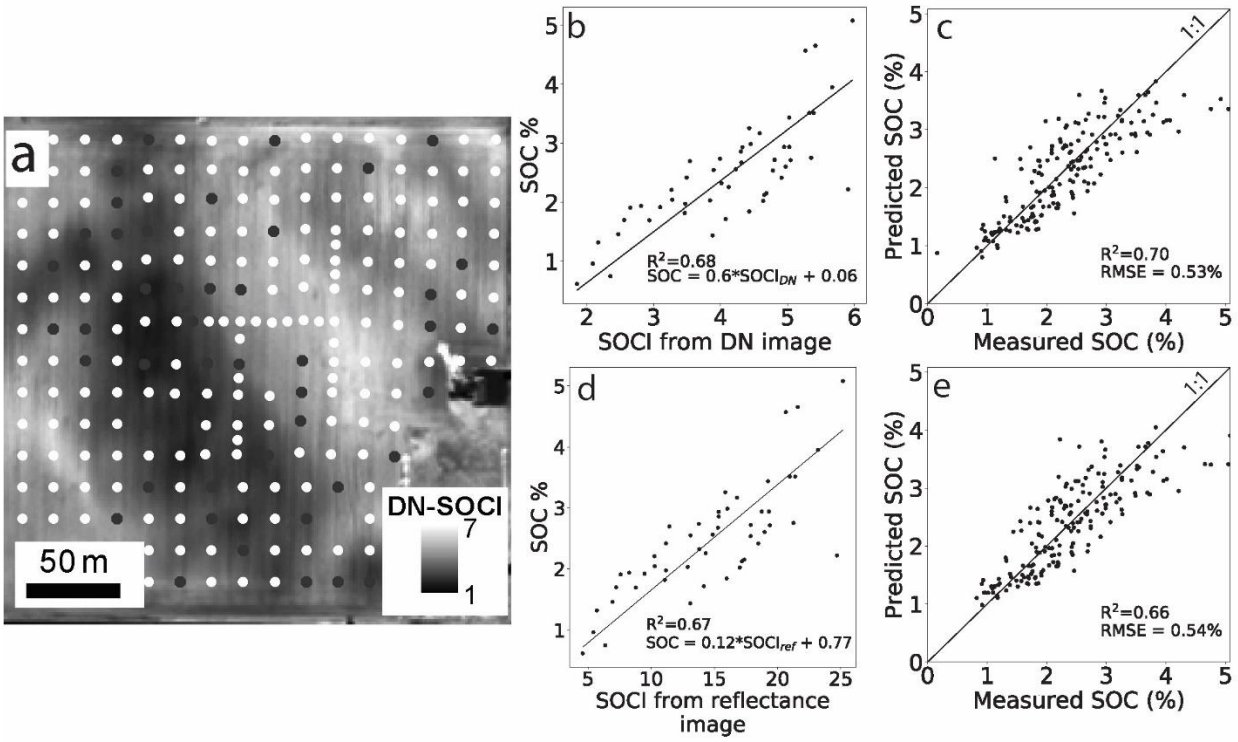

Fig. 2.4 a) Map of the SOCI calculated from a digital number (DN) image of a field in Iowa where SOC was measured in 228 soil samples (Li et al., 2018). Sample locations are shown as circles, those shown in black are the random 20% selection used in the calibration. b) Measured SOC versus SOCI values derived from the DN image (R^2 = 0.68). c) Predicted SOC versus measured SOC, where predictions are calculated from the relationship shown in b. The predicted SOC is correlated with measured SOC with

R^2=0.70 and RMSE=0.53%. d) Measured SOC versus SOCI values derived from the reflectance image for the calibration dataset (R^2 = 0.67). e) Predicted SOC vs measured SOC, where predictions are calculated from the relationship shown in d. The predicted SOC is correlated with measured SOC with R^2=0.66 and RMSE=0.54%.

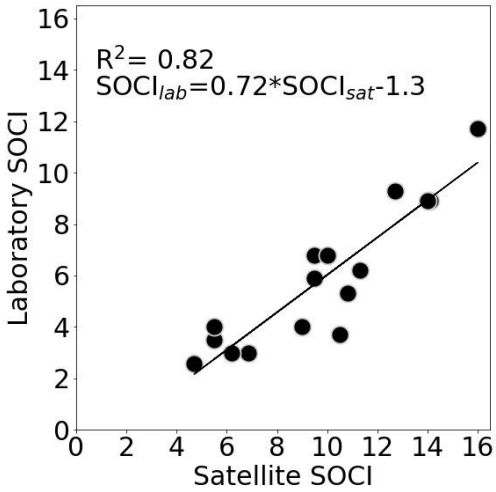

Fig. 2.5 The SOCI derived from RaCA laboratory spectral data versus SOCI derived from WorldView-2 satellite imagery spectral data (n=16).

Regional calibration

The comparison of SOCI values calculated from co-located RaCA soil samples and WorldView-2 imagery indicates the two indices are linearly correlated with an R^2 of 0.82 (Fig. 5). Because the SOCI values are well-correlated, the regression relationship was used to scale WorldView-2 satellite-derived SOCI values to the same range of SOCI values determined from the RaCA samples. The scaled, regionally-calibrated SOCI, based on the RaCA samples, generated SOC predictions that were comparable to the calibrations that were locally calibrated, but only after accounting for depth-averaged

SOC concentrations. We found that surface SOC concentrations predicted from the satellite image are correlated to the average SOC for the upper 30 cm of the soil profile with an R^2 of 0.66 and a RMSE of 4.8% SOC (Fig. 6a). However, after estimating the average SOC concentration within the upper 30 cm of the profile using an exponential decay function (Fig. 6b) the RMSE improved to 0.54% SOC (Fig. 6c).

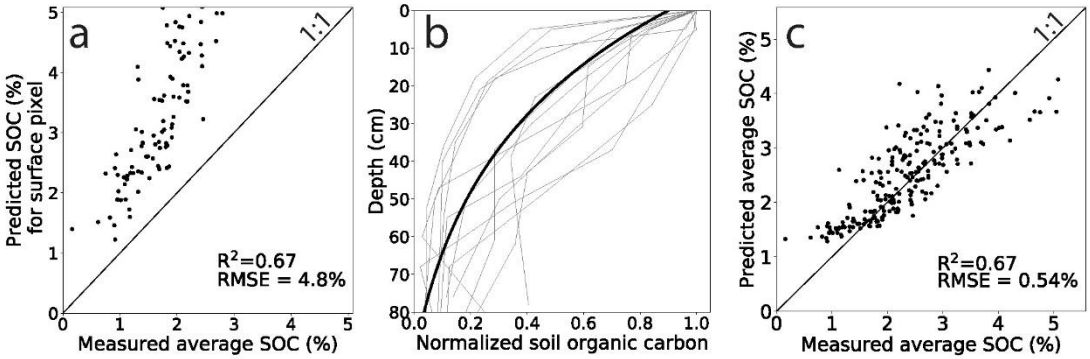

Fig. 2.6 a) SOC predicted for a surface pixel versus the measured average SOC for a 30 cm profile (R^2 = 0.67, RMSE = 4.8%), b) SOC-depth curves for 15 RaCA sites within the Western Corn Belt Plains ecoregion (gray lines) and the average exponential function (black line), where *a* is 3.5% SOC and *b* is -13.1. The SOC-depth profiles are normalized by the maximum SOC concentration for each profile. c) Same data as in a, except the predicted values have been scaled to the mean values for the upper 30 cm of the soil using the average exponential function in b. The predicted SOC is linearly correlated to the measured SOC with R^2=0.67 and a RMSE of 0.54% SOC.

Discussion

The SOCI is effective at estimating SOC because it tracks changes in the reflectance of the Red and Green wavelengths, which have been demonstrated to be

relevant for SOC estimations (Bartholomeus et al., 2008; Stevens et al., 2010). The slopes of reflectance curves in the visible wavelengths generally decline as a function of SOC, and the reflectance values for each of the visible wavelengths decreases with increasing SOC (Fig. 7). Concentrations of pedogenic iron-bearing minerals, which impart a red hue to soil, have been found to be inversely correlated to concentrations of SOC, such that soils with a red hue often have less organic matter and more iron oxide minerals than dark-colored SOC-rich soils (Frazier and Cheng, 1989; Palacios-Orueta and Ustin, 1998). Hence, soils enriched in pedogenic iron relative to SOC have increased reflectance in the Red and Green wavelengths relative to soils enriched in SOC (Huete and Escadafal, 1991; Palacios-Orueta and Ustin, 1998). The large increase in Red and Green reflectance in samples with low SOC, relative to darker samples with high SOC (Fig. 6), results in decreased SOCI values.

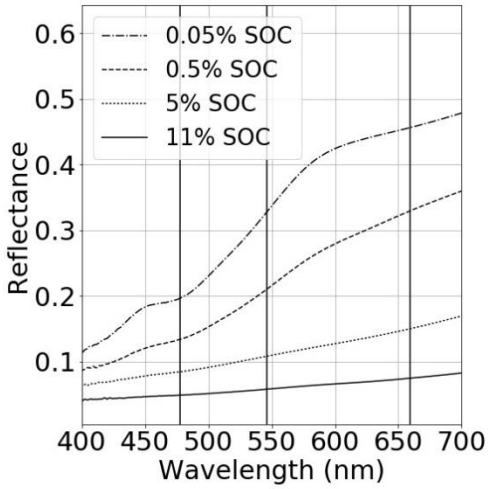

Fig 2.7. Influence of soil organic carbon (SOC) on spectral reflectance. Examples of spectral curves for samples within the RaCA database with SOC concentrations ranging

from 0.05% to 11%. Vertical bars show the reflectance values used in the calculation of the SOCI: 478 nm (Blue), 546 nm (Green), and 659 nm (Red).

For the national dataset, the three Level I ecoregions, and the 54 Level III ecoregions, the ability of the SOCI to predict SOC is comparable to the predictive power of the SWIR/NIR index and better than the $SI_{1001\text{-}679\ nm}$ index. An artificial neural network model, developed using ~20,000 samples from the RaCA database that incorporated textural as well as spectral information about the soil samples predicted SOC with RMSE values that ranged from 0.5-1.5% (Wijewardane et al., 2016). Likewise, using a dataset of ~8,600 samples from the RaCA, a random forest model, which also included horizon and texture information, was able to predict SOC with RMSE values ranging from 2.0 to 2.5% (Sequeira et al., 2014). The SOCI performance for the national and Level I ecoregion datasets (RMSE 1.5%-1.8%) is within the range of or slightly better than these multivariate techniques, which, along with its similar performance to the SWIR/NIR index, indicates the SOCI has potential for SOC prediction. Further, because the SOCI uses fewer wavelengths for predictions than multi-variate and machine learning methods it can be readily applied to multispectral imagery, as demonstrated by the calculation of the index from the WorldView-2 data (Figs. 5, 6).

The application of the SOCI to the WorldView-2 image of the field in Iowa, where soil properties are less variable than in the nationwide and ecoregion datasets, provides a test of its ability to predict SOC. There, SOCI is well-correlated with SOC with RMSE of ~0.5%, demonstrating that the index is a useful method for remotely measuring SOC. Because the SOCI relies only on the visible spectrum it has potential to

be more widely applied than the SWIR/NIR index, as SWIR and NIR wavelengths are often not available or are much costlier for very high-resolution satellite sensors (≤4m). For example, the SOC predictions for the field in Iowa would not be possible with the SWIR/NIR index, given the current resolution and library of SWIR imagery. Due to spatial variability in factors such as topography and erosion, SOC varies widely on small spatial scales; for example, within the 15 ha field in Iowa, SOC ranges from 0.2-5.0% (Li et al., 2018). Publicly-available platforms with global coverage of SWIR measurements (e.g. Landsat OLI, ASTER) often measure SWIR at 30 m spatial resolution (Roy et al., 2014). Such coarse resolution pixels are a mixture of soil properties (Adams et al., 1986), limiting the spatial scale at which SWIR-based indices can be used to predict SOC concentrations. Although there are satellite sensors that measure in the SWIR region at high spatial resolution, the library of images is not yet as spatially extensive as VIS data from other platforms.

Application of SOCI to imagery of plowed agricultural fields with exposed soil has potential to provide a rapid and robust qualitative assessment of the distribution of degraded soils from field to regional scales, as well as quantitative estimates of SOC. The SOCI can be applied to SOC prediction in at least two ways. For example, within the RaCA study region, the SOCI can be calculated from radiometrically-calibrated imagery and scaled to the RaCA-derived values (Fig. 4d). SOC can then be predicted using the regression relationships that are listed in Table S2 between SOC and SOCI for the ecoregion of interest. For areas where data like those in the RaCA database do not exist, regression relationships between SOC and the SOCI can be locally developed from laboratory and satellite spectral data and SOC measurements to predict SOC.

Alternatively, the strong correlation between SOC and the SOCI calculated from the DN image (Fig. 4c), as well as the similarity in the RMSE between the DN- and reflectance-derived SOCI values, suggests that raw imagery can be used to estimate the concentration of SOC without performing radiometric correction. Such a finding implies that any true-color image can be used to estimate SOC, including those collected from cameras on manned or unmanned aerial vehicles. The SOCI hence provides the ability to rapidly perform large scale, high resolution assessments of carbon stocks and identify SOC-poor soils within agricultural fields. Such information can guide agriculture land management decisions by allowing farmers to target SOC-depleted soils for remediation and precision nutrient application (McCarty and Reeves, 2006; Rossel et al., 2006).

Conclusions

We used 7,916 hyperspectral and SOC measurements from soil samples collected by the USDA Rapid Carbon Assessment from the conterminous U.S. to develop a new spectral index for predicting SOC concentrations that uses only the visible (Red, Green, and Blue) wavelengths. We find that our new index performs similarly to the SWIR/NIR index and better than the $SI_{1001\text{-}679\ nm}$ index, both of which rely on longer wavelengths than those in the visible spectrum. We calculated the new index on a high-resolution WorldView-2 image of a field in Iowa where SOC had previously been measured to test its ability to predict SOC concentrations. With local calibration data the new SOCI calculated from both a raw image and a radiometrically-corrected reflectance image predicts SOC concentrations with a RMSE of approximately 0.5%, indicating that with the use of local calibration data, radiometric correction of imagery is not necessary for

application of the index. We also showed that the SOCI can be used to predict SOC with a region-wide calibration by scaling the WorldView-2 satellite spectra to the same range as the Rapid Carbon Assessment laboratory spectra, where the index predicted measured SOC values with a RMSE of 0.54%. Because the new index relies only on the visible spectrum, it can be used to predict SOC using any true color image, which are captured by most satellite sensors and cameras, including those mounted on unmanned aerial vehicles, at increasingly high spatial resolution. Hence, the index has the potential to be widely applied to map SOC at the field to regional scale. Such maps have a wide range of potential applications for informing carbon budgets and guiding soil management.

Acknowledgments

The research was funded by NASA grant 80NSSCK0747 to Larsen. We thank Skye Wills and the USDA NRCS National Soil Survey Center for access to the laboratory data from the Rapid Carbon Assessment. We thank Elizabeth Hoy of NASA and Paul Morin of the Polar Geospatial Center for assistance accessing imagery - *Geospatial support for this work provided by the Polar Geospatial Center under NSF-OPP awards 1043681 and 1559691.* We are also grateful to Xia Li for sharing published soil organic carbon data and anonymous reviewer for helpful comments.

Appendix A includes a table of the combinations of visible band wavelengths used to develop the index and a table of equations, correlation coefficients, and root mean square error of each index for all 54 Level III ecoregions.

CHAPTER 3

SOIL MOISTURE EFFECTS ON NEAR SURFACE REFLECTANCE AND IMPLICATIONS FOR SOIL CARBON REMOTE SENSING

Abstract

Chemical and physical characteristics influence the spectral reflectance of soils. Among the most dominant factors influencing spectral reflectance are soil organic carbon and soil moisture, with increases in either factor resulting in decreasing spectral reflectance. Disentangling the effects of soil moisture on the spectral signature of soil organic carbon has hindered efforts to quantify soil organic carbon using airborne or satellite imagery of bare soil. Here, we perform a laboratory experiment and calculate the soil organic carbon index under a range of gravimetric soil moisture levels for soil samples with organic carbon concentrations ranging from 0.1-12%. We find that soil moisture has the largest effect on the spectral reflectance of soils with the highest organic carbon concentrations. For samples with the largest concentration of soil organic carbon (~12%), there is a factor of four increase in the soil organic carbon index, whereas the soil organic carbon index increases by a maximum factor of three for samples with < 1% soil organic carbon. Modeling studies have indicated that the soil moisture at the soil surface becomes decoupled from soil moisture at depth, resulting in relatively rapid drying of the soil surface. We test this modeling result by measuring the amount of time for soils packing in a column to return to dry soil organic carbon index values after being wetted. We used one soil collected from a hilltop and one sample collected from a hollow from an agricultural field in Iowa. The SOCI of the hilltop soil sample returned to the dry value after 25 hours, while the SOCI of the soil sample collected from the hollow

returned to the dry value after 27 hours. The results indicate that soil moisture does not affect the spectral signature of soil organic carbon of the surface soil after a day of dry conditions.

Introduction

Assessment of soil physical and chemical properties through near-infrared diffuse reflectance spectroscopy is a rapidly expanding field. Particular attention has been given to quantifying soil organic carbon (Viscarra Rossel et al., 2006; Gomez et al., 2008; Thaler et al., 2019) because of concerns of soil fertility degradation and the influence of soil carbon on the global carbon cycle. Efforts to map soil organic carbon at regional and field scale have led to the development of multiple remote sensing indices (Frazier and Cheng, 1989; Peón et al., 2017; Thaler et al., 2019). Soil moisture content can obscure the spectral signature of soil organic carbon, as an increase in either soil organic carbon or soil moisture results in a decrease in spectral reflectance in the optical wavelengths (Lobell and Asner, 2002; Minasny et al., 2011), but the effect of soil moisture on spectral indices for soil organic carbon has not been assessed. Here, we perform a laboratory experiment to quantify the effect of soil moisture on the soil organic carbon index (SOCI) (Thaler et al., 2019) values for soils with a range of organic carbon concentrations.

Methods have been developed to remove the effects of soil moisture on the full spectral profile of soils within the optical wavelengths, including calculating the first derivative of the reflectance spectra (Wu et al., 2009) and the more ubiquitous external parameter orthogonalization (EPO) (Roger et al., 2003; Wijewardane et al., 2016). EPO decomposes a given soil spectrum into two components: the component directly

influenced by the response variable (e.g., soil organic carbon) and an obscuring component which is imparted by an external parameter (e.g., soil moisture). The regions of the spectrum which are influenced by the external parameter are projected orthogonal to the influenced variations, which effectively removes the variability. In laboratory settings, EPO has been shown to largely remove the effect of soil moisture on soil spectral reflectance in laboratory experiments (Roger et al., 2003; Minasny et al., 2011; Wijewardane et al., 2016). Although successful at removing the effect of soil moisture in controlled laboratory environments, EPO does not improve the accuracy of prediction of soil organic carbon from airborne imagery (Guo et al., 2019) and hence cannot be used to correct laboratory-derived soil organic carbon indices.

Spectral indices for estimating soil organic carbon derived from laboratory analysis of dried soil samples can be applied to satellite or airborne imagery of bare soil only if the soil surface is also dry during the time of image acquisition (Thaler et al., 2021). Modeling of soil moisture concentration and vertical movement through a soil profile indicate that the moisture concentration of the soil surface layer quickly becomes decoupled from moisture at depth, leaving the soil surface dry three to four days after rainfall (Capehart and Carlson, 1997), but the time frame over which spectral properties of soils return to dry conditions has not been assessed. Here we perform a laboratory soil infiltration experiment, in which we measure the amount of time for the soil surface to dry in surface soils from hilltop and soils from a hollow collected within an agricultural field in Iowa.

Methods

To determine the influence of soil moisture on the SOCI and the potential impact on the differentiation of soil horizons from spectral data, we conducted a laboratory experiment to measure the spectral reflectance of 27 soil samples with a range of soil organic carbon concentrations; 26 samples were collected from the Midwestern U.S., and one sample was collected from a wetland in western Massachusetts to assess changes on a soil with a high organic carbon concentration. All soil samples were split, ground with a mortar and pestle, and sieved to 2 mm prior to measuring the spectral reflectance.

Of the Midwestern soil samples, 18 are from a ~5 cm diameter soil core collected to 105.3 cm depth from a native prairie in Iowa. The core was sampled in 2.1 cm increments from 0- 73.5 cm and then from 94.9 to 105.3 cm, to encompass the full range of soil organic carbon values. The other eight Midwestern soil samples were collected from 0-18 cm and from 90-108 cm depth. Soil organic carbon was measured for each sample using a Costech elemental analyzer (ECS 4010) following removal of inorganic carbon with 1 N HCl.

We assessed the effect of soil moisture on the SOCI for the soils by measuring soil spectral reflectance under dry and saturated moisture levels. The spectra used to calculate the SOCI values were measured using an ASD FieldSpec 4 with a Muglight attachment. The spectral reflectance was measured when the samples were dry and again when the samples were saturated with moisture. The reflectance for each moisture level was measured three times, and between measurements the spectroradiometer was recalibrated using a Spectralon white reference. The samples were oven-dried at 90º C for 30-minutes, after which both the gravimetric soil moisture content and the spectral reflectance were measured. For each sample, the maximum factor change in the SOCI

was calculated as the SOCI calculated for the greatest soil moisture content divided by the dry SOCI value.

Soil samples used for the infiltration experiment were collected from the surface layer of soil within a field in the Iowa using a 5 cm diameter, 1 cm thick ring. The soils were packed into a 2.5 cm clear plastic core tube. The length of the soil sample in the core tube was chosen to match the bulk density of the soil collected within the ring in the field, and a 1 cm gap was left at the top of the core to allow for water to be added to the sample. The core tube was attached to a laboratory stand, and placed on a balance, so that the mass of the soil sample, including the additional water, could be measured as the experiment progressed. The reflectance sensor was positioned 4 cm above the soil sample in the tube, so that the field of view encompasses the entire diameter of the sample. The soil was illuminated using a full spectrum light. Measurements of the spectral reflectance of the dry soil and the initial dry weight were collected, and then 1 cm of water was added to the sample. A picture of the experimental design is shown in Figure 3.1. The reflectance and weight were immediately measured once the water infiltrated through the soil surface and were measured every hour until the reflectance of the surface returned to the dry value.

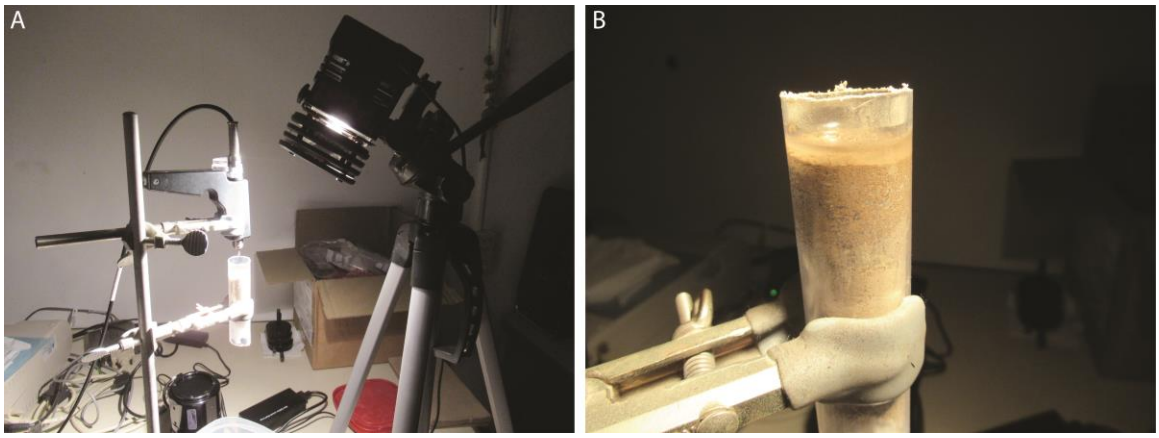

Figure 3.1 Infiltration experiment setup. A) Image showing the soil sample in the laboratory stand with the sensor held 4 cm above the soil surface and illuminated by the full spectrum light. B) Image showing soil core after addition of 1 cm of water.

Results

Effect of soil moisture on the soil organic carbon index

Measured soil organic carbon concentrations for the 27 samples range from 0% to 12%. Similarly, the dry SOCI values range from 2.5 to 7.5. For all soil samples analyzed in the muglight experiment, the SOCI increased for wet samples compared to dry samples. We found that the magnitude of the increase in the SOCI as a function of soil moisture is related to the SOC concentration of the sample (Fig. 3.2). For samples with concentration of SOC > 3%, there was a factor of four increase in the SOCI, whereas the SOCI increased by a maximum of a factor of three for samples with < 1% SOC (Fig. 3.3). The SOCI for the muglight samples did not return to the dry values until the gravimetric soil moisture content returned to 0%.

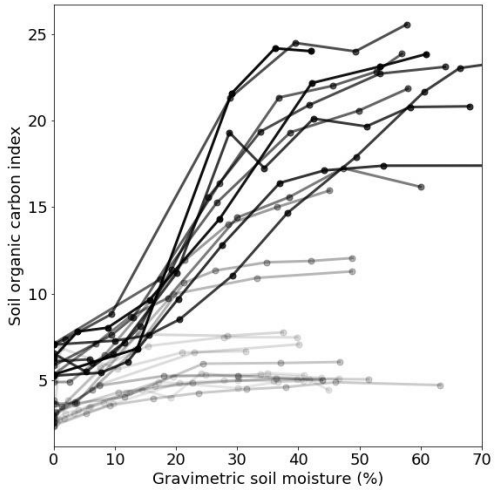

Figure 3.2 The soil organic carbon index as a function of the gravimetric soil content for each of the 27 samples. Lines and points with darker shading indicate samples with greater concentrations of soil organic carbon.

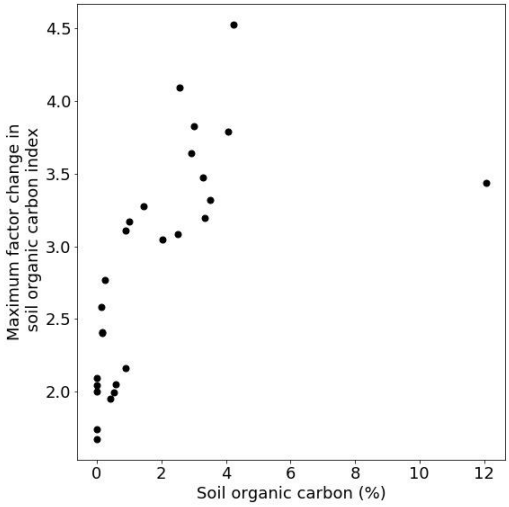

Figure 3.3 The factor change in the soil organic carbon index between the dry samples and samples saturated to their maximum gravimetric moisture level for 27 soil samples as a function of soil organic carbon content.

Infiltration experiment

After the addition of water to the soil column containing the hilltop soil, the SOCI increased from 2.5 to 4.2 in the first hour, and the gravimetric soil moisture content in the column was increased to the maximum value of 19%. The SOCI reached a peak value of 5.7 after 20 hours, and then decreased to 2.4 at hour 25 (Fig. 3.4A), but the final moisture content only decreased to 15%. The SOCI value of the soil sample from the hollow increased from 8.6 to 21.8 in the first hour, and the initial gravimetric soil moisture content after the addition of water was 19%. The SOCI reached a peak value of 22.3 at hour 10, and then decreased to 8.5 at hour 27, while the soil moisture content dropped to 17% (Fig. 3.4B).

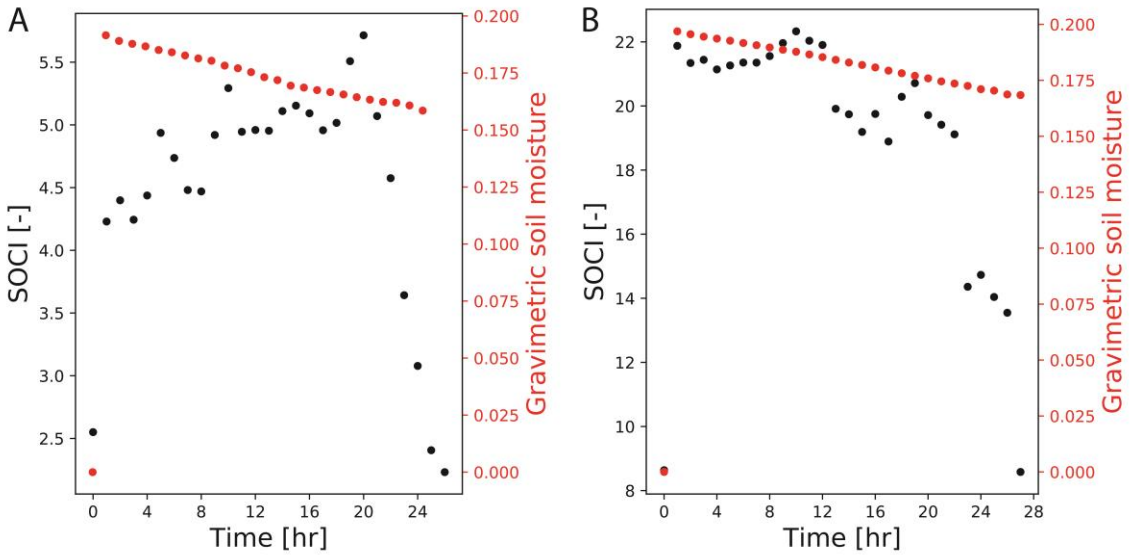

Figure 3.4 Evolution of soil organic carbon index values (SOCI) and soil moisture content during the infiltration experiment. A) Soil sample from a hilltop within an agricultural field from Iowa. B) Soil sample from a hollow within the same field as A. Black points represent the SOCI value, and red points indicate the gravimetric soil moisture content measured at each hour.

Discussion

Although the SOCI is effective at estimating organic carbon concentrations from dry soils (Thaler et al., 2019), it is influenced by soil moisture, where an increase in soil moisture content causes an increase in the SOCI and hence an increase in the predicted organic carbon concentration. The influence of soil moisture on the SOCI indicates that dry, bare soil imagery is required when transferring from laboratory to aerial- or satellite-based spectra. If the soils within acquired images are wet, then the SOCI values derived from the imagery will predict erroneously high organic carbon concentrations for the soils.

The results from our infiltration experiment indicate that the moisture content at the soil surface dries within ~ one day and becomes decoupled from the moisture content within the soil column. Even the soil surface of organic carbon-rich soils, which have higher water retention potential than organic carbon-poor soils found on hilltops, dry within 27 hours. These results align with more conservative modeling estimates, which indicate the soil surface becomes dry three to four days following precipitation (Capehart and Carlson, 1997). Although the addition of soil moisture impacts the SOCI value of a given soil, our analysis indicates that estimates of soil organic carbon, which will not be influenced by soil moisture, can be obtained using imagery that is acquired at a minimum of one day following a precipitation event.

CHAPTER 4

THE EXTENT OF SOIL LOSS ACROSS THE U.S. CORN BELT

Abstract: Soil erosion in agricultural landscapes reduces crop yields, leads to loss of ecosystem services, and influences the global carbon cycle. Despite decades of soil erosion research, the magnitude of historical soil loss remains poorly quantified across large agricultural regions because pre-agricultural soil data are rare, and it is challenging to extrapolate local-scale erosion observations across time and space. Here we focus on the Corn Belt of the Midwestern U.S. and use a novel remote sensing method to map areas in agricultural fields that have no remaining organic carbon-rich A-horizon. We use high-resolution satellite and LiDAR data to develop a relationship between A-horizon loss and topographic curvature, and then use topographic data to scale-up soil loss predictions across 3.9×10^5 km^2 of the Corn Belt. Our results indicate that 35±11% of the cultivated area has lost A-horizon soil, and that prior estimates of soil degradation from soil survey-based methods have significantly underestimated A-horizon soil loss. Soil

loss is most prevalent on convex slopes. Hilltops throughout the region are often completely denuded of A-horizon soil. The association between soil loss and convex topography indicates that tillage-induced erosion is an important driver of soil loss, yet tillage erosion is not simulated in models used to assess nationwide soil loss trends in the U.S. We estimate that A-horizon loss leads to a 6±2% decrease in crop yields, causing $2.8±$0.9 billion in annual economic losses. Regionally, we estimate 1.4±0.5 Pg of carbon have been removed from hillslopes by erosion of the A-horizon, much of which likely remains buried in depositional areas within the fields.

Main text

Productive agricultural soils are vital for producing food for a growing global population (Amundson et al., 2015; Montgomery, D. R., 2007; Tilman et al., 2002). However, degradation of soil quality by erosion reduces crop yields, which can result in food insecurity, conflict (Amundson et al., 2015), and the decline of civilizations (Montgomery, David R., 2012). Degradation of soils leads not only to economic losses for farmers, but also a loss in ecosystem services (Daily et al., 1997), which alters the ability of soils to regulate hydrologic and biogeochemical cycles. Widespread use of synthetic fertilizers to enhance the function of degraded soils increases food production costs (Pimentel et al., 1995) and impairs water resources (Schilling and Spooner, 2006), which negatively impacts human health (Weyer et al., 2001) and aquatic ecosystems (Turner and Rabalais, 1994).

Globally, the reservoir of carbon stored in soils is three times that in the atmosphere (Lal, Rattan, 2004), and given the extent of agricultural land use (Ramankutty and Foley, 1998), understanding soil carbon dynamics in agricultural systems is critical to understanding the carbon cycle (Guo and Gifford, 2002). Whether soil erosion constitutes a net carbon sink or source depends on both the depositional fate of the eroded carbon and the ability to replace carbon in degraded soils (Lal, Rattan, 2005a; Stallard, 1998; Van Oost, K. et al., 2007). If biological productivity replaces eroded carbon, and decomposition of carbon stored in sedimentary deposits is halted or slowed, then soil erosion is a net sink of atmospheric carbon (Berhe et al., 2007; Lal, 2005; Van Oost et al., 2007; Wang et al., 2017). However, if eroded carbon rapidly decomposes and is not replaced in eroded soil horizons, then soil erosion constitutes a carbon source. Restoring carbon to degraded soils therefore has potential to both re-establish soil function and sequester atmospheric CO_2 (10). However, quantifying the impacts of soil degradation on agricultural productivity and the carbon cycle first requires robust estimates of the magnitude of agriculturally-induced soil loss (14, 16).

Although thousands of soil erosion measurements have been made globally (García-Ruiz et al., 2015), the lack of a robust and scalable method for estimating the magnitude of erosion in agricultural landscapes remains a major gap in soil erosion research (Poesen, 2017). Large-scale assessments of soil erosion are often based on model predictions (Morgan et al., 1998; Nearing et al., 1989; Renard et al., 1997) or qualitative information from soil surveys regarding the degree of soil degradation (Jelinski and Yoo, 2016) In the U.S., for example, nation-wide soil loss trends (U.S. Department of Agriculture, 2018) are simulated using water and wind erosion models

that have been calibrated with erosion measurements made on small plots over a period of decades (Renard et al., 1997; Woodruff and Siddoway, 1965). It has been debated whether upscaling such predictions to regional or national scales results in an accurate assessment of the current magnitude of soil loss in the U.S. (Nearing et al., 2000; Trimble and Crosson, 2000). Whereas such models are useful for assessing relative rates of erosion for soil conservation planning, the soil loss predictions do not provide information regarding the cumulative soil loss that has occurred since the initiation of cultivation, and hence the overall magnitude of agricultural soil degradation.

To assess the degree of cumulative soil degradation, soil surveys conducted by the U.S. Department of Agriculture have assigned erosion classes to soils based on the percentage of the original A-horizon that has been eroded (Soil Science Division Staff, 2017). Because the A-horizon has the largest fraction of soil organic carbon within the soil profile, it is a key component of water and nutrient retention and soil productivity (Lal, Rattan, 2005b). Soils where 100% of the A-horizon thickness has been removed are designated as Class 4 eroded soils, and other classes represent lesser reductions in A horizon thickness (<25%, 25%-75%, >75%, for Class 1, 2, and 3, respectively). A major disadvantage of the use of erosion classes is that properly assigning classes based on the percentage of A-horizon loss requires accurate determination of the original A-horizon thickness on all topographic positions (Olson et al., 1994). Hence, although soil erosion classes indicate soil degradation is widespread (Jelinski and Yoo, 2016), we do not have a robust, quantitative understanding of how much soil has already been lost.

Here we present results from a new remote sensing method used to estimate the spatial extent of agriculturally-induced loss of A-horizon soil for a major global

agricultural region, the Corn Belt of the Midwestern U.S. Rather than simulate or measure short-term soil loss rates, we combine measurements of soil surface reflectance in the visible spectrum (soil color) with high resolution satellite imagery to directly measure the proportion of the agriculturally cultivated landscape that has completely lost its original A-horizon. Combining our spectral analysis with relationships between A-horizon soil loss and topography derived from high-resolution LiDAR topographic data allows us to predict A-horizon soil loss in areas where images are not available. We find that historical soil erosion has completely removed A-horizon soil from approximately one-third of the Corn Belt. The spatial patterns of soil loss suggest that key erosion mechanisms are not simulated in nationwide assessments of soil erosion trends in the U.S. and that soil survey data greatly underestimate the extent of A-horizon loss.

The Corn Belt region of the Midwestern U.S.

Our study focuses on the Midwestern U.S., on a ~390,000 km^2 region that encompasses much of the area colloquially known as the Corn Belt (Fig. 1). The region was glaciated repeatedly during the Pleistocene, with the exception of the Driftless area (Bettis III et al., 2003). The most recent ice sheet advance deposited glacial till in the northern part of the Corn Belt; whereas older glacial deposits to the south are mantled with loess (Bettis III et al., 2003). Prior to European settlement in the mid-late 19^{th} century, the vegetation was primarily tallgrass prairie with some savanna and woodlands (Sampson and Knopf, 1994), and mollisols are the dominant soil order in the region (Soil Survey Staff, 1999). The native prairie vegetation fostered the accumulation of thick A-horizon soils (*SI Appendix*, Fig. S1, Table S1). In the decades following European

settlement the prairie was plowed, and the landscape was rapidly and extensively converted to row-crop agriculture. For example, in Iowa, Indiana, and Illinois, less than 0.1% of the original tallgrass prairie remains (Sampson and Knopf, 1994). The fertile soils and temperate climate make the Corn Belt one of the world's most agriculturally productive regions. The U.S. is the world's largest producer of corn and soybeans (Food and Agriculture Organization of the United Nations, 2017), and 75% of the corn and 60% of the soybeans produced in the U.S. are grown in the Corn Belt (U.S. Department of Agriculture, 2017).

Despite the importance of the region's agricultural productivity, model predictions indicate the Corn Belt currently has the highest soil erosion rates in the U.S. (U.S. Department of Agriculture, 2018). The historical magnitude of A-horizon soil loss from the initiation of agriculture to the present is unknown, but prior work in Iowa and Minnesota noted that in some areas, the magnitude of soil erosion has been great enough to completely remove dark, carbon-rich A-horizon soil, exposing light-colored B-horizon soil that is poor in organic carbon (Fenton et al., 2005; Lindstrom et al., 1990).

A-horizon soil loss in individual fields

We combined high-resolution satellite imagery, a newly developed soil organic carbon index (Thaler et al., 2019), and soil spectral data from the U.S. Department of Agriculture's Rapid Carbon Assessment to develop a logistic regression to differentiate between A- and B-horizon soils exposed in plowed fields. The extent of historical soil loss was measured by the absence of the A-horizon, or inversely, by the presence of B-horizon soils, which underlie the A-horizon. An example field where we applied our

method is shown in Fig. 2, where pixels of A- and B-horizon soil are distinguished using the soil organic carbon index (Fig. 2a), and topographic curvature is calculated for each pixel in the field (Fig. 2b). Within the field, A-horizon soil has been completely removed from 34±7% (±1 S.D.) of the area (Fig. 2c). The fraction of pixels classified as B-horizon soil is highest on convex slopes, indicating topography exerts a strong influence on the spatial distribution of A-horizon loss within the field (Fig. 2d).

In 210 km^2 of agricultural fields across 28 locations, the soil organic carbon index values indicate the mean extent of the agricultural land area with complete A-horizon loss is 34±7% (Fig. 3a). These A-horizon soil loss values are minimum estimates because of the potential for soil moisture to cause misclassification of soil horizons (see *SI Appendix*). At all 28 sites, hillslope topography strongly controls the location of soil loss. B-horizon exposure occurs disproportionately on convex topography, which we quantitatively define as areas with topographic curvature values < 0 m^{-1}. Such areas make up only 50% of the area of the fields we analyzed but are the site of 68±9% of the exposed B-horizon soil. On hillslopes with the most convex topography (curvature < -0.02 m^{-1}), 74±8% of the land area has soil organic carbon index values indicative of exposed B-horizon soils. The proportion of the cultivated landscape with complete A-horizon loss decreases to 23±5% for straight slopes (curvature = 0), and 39±8% of the land area on concave topography (curvature > 0 m^{-1}) bears the spectral signature of B-horizon soils (Fig. 3b).

The most convex and concave portions of the cultivated landscape tend to have the greatest proportion of soil loss, due to an association of steeper slopes (3.5-4.1 degrees) with highly convex and concave topography (Fig. 3b). However, most of the

cumulative A-horizon loss occurs on more modestly sloping topography; 84±2% of the B-horizon exposure occurs in areas with curvature values between -0.02 m^{-1} and 0.02 m^{-1}, where the mean slope is 2.2 degrees. These results indicate hillslope summit and shoulder positions are prominent locations of soil loss. The implications of the topographic distribution of soil loss for inferring soil erosion mechanisms are discussed below.

The region-wide extent of A-horizon soil loss

Based on the proportion of B-horizon exposure for a given value of topographic curvature for the 210 km^2 of fields with available satellite imagery (Fig. 3b) and $3.9x10^5$ km^2 of topographic curvature data that span the region, we estimate that A-horizon soil has been completely removed from 35±11% or 132,738±46,849 km^2 of the Corn Belt (Fig. 3c). Within the Corn Belt, convex topography occupies roughly 70% of the cultivated landscape (~273,000 km^2), and 68% of the area predicted to no longer have A-horizon (~90,000 ±33,000 km^2) occurs on that convex topography, whereas the remaining 32% (~42,000 ±15,000 km^2) occurs on concave topography.

The proportion of the study area within each Corn Belt state predicted to have exposed B-horizon soil ranges from 30±10 to 41±13% (Fig. 4a), and county-level estimates range from 24±8 to 47±14% (Fig. 4b). Glacial history influences the extent of soil loss, with greater loss predicted for older, now loess-covered glaciated areas where drainage networks and associated ridge and valley systems are more developed. The extent of A-horizon loss is lower in areas that were covered with ice during the last glaciation because drainage networks are more poorly developed and ridge-valley systems are less established (Lai and Anders, 2018).

Our method predicts the land area with complete A-horizon loss, rather than soil erosion rates, so our results cannot be directly compared against regional soil erosion rates modeled using the Revised Universal Soil Loss Equation and the Wind Erosion Equation (U.S. Department of Agriculture, 2018). However, the Class 4 erosion class category from soil surveys (Soil Science Division Staff, 2017) is equivalent to the complete loss of A-horizon measured by our analysis. U.S. Department of Agriculture soil survey data indicate that none (0%) of our study area has soils with Class 4 erosion, or complete A-horizon loss (*SI Appendix* Fig. S2) (Soil Science Division Staff, 2017). However, we predict the A-horizon has been completely removed from 35±11 % of the cultivated area of the Corn Belt. Hence our results suggest that prior assessment of soil degradation based on erosion classes may have greatly underestimated the extent of A-horizon loss, and therefore the thickness or mass of soil that has been eroded from hillslopes in the Corn Belt.

Soil loss mechanisms

Our results indicate that A-horizon soil has been stripped from hilltops and hillslopes. Although our remote sensing method cannot detect soil deposition, prior work indicates that much of the eroded soil has accumulated in topographic concavities (Li, X. et al., 2018; Papiernik et al., 2009), though some is ultimately transported out of fields by water erosion (Li, H. et al., 2016). Hence topographic concavities tend to have thicker A-horizons, higher soil organic carbon concentrations, and higher crop yields than eroded hilltop summits and shoulder positions (Papiernik et al., 2009). Although water erosion contributes to soil loss throughout the cultivated landscape, our observation of

widespread loss of soil from low gradient, convex hilltops and deposition in topographic concavities at the base of hillslopes suggests tillage erosion is also an important driver of soil transport in the Corn Belt.

Tillage erosion is the net downslope movement of soil by repeated tillage operations, such as plowing (Govers et al., 1996). Soil transport by tillage causes diffusion-like evolution of topography, resulting in erosion of soil from topographic convexities and deposition in concavities (Li et al., 2018). The effect of tillage on soil transport can be described with a diffusion-like coefficient that integrates tillage direction, depth, and soil physical properties (Van Oost, Kristof et al., 2006), and measured diffusion coefficients for tillage range from 0.03 to 0.52 m^2 yr^{-1} (Van Oost et al., 2006). Although contour plowing is a common strategy to mitigate soil erosion by water, measured diffusion coefficients for contour plowing still range from 0.03 to 0.2 m^2 yr^{-1} (Van Oost et al., 2006). Such values are one to three orders of magnitude greater than diffusion coefficients measured in non-agricultural settings (Fernandes and Dietrich, 1997). Hence order-of-magnitude increases in topographic diffusion due to plow- and tillage-based agriculture provides a mechanistic explanation for the extensive loss of soil from hilltops, especially where the lack of upslope flow accumulation area limits the potential for water erosion by overland flow. The observation that the fraction of a landscape without A-horizon soil increases with increasing topographic convexity is also consistent with a diffusive, tillage erosion soil transport process.

Prior work has shown that whereas water and tillage both contribute to soil transport, erosion on upland convex hilltops is dominated by tillage, and erosion by water tends to be dominant in areas with steep, concave slopes (Schumacher et al., 2005). Our

finding that B-horizon exposure increases with slope for concave topography is consistent with previous work indicating that water erosion is dominant in such landscape positions. About 30% of the observed A-horizon loss has occurred on concave topography where water erosion is expected to dominate soil loss. The remaining ~70% of landscape with B-horizon exposure occurs on convex hilltops and slopes, where tillage is expected to be a more important mechanism of soil loss than erosion by water (Schumacher et al., 2005). Although it has been demonstrated that models that do not simulate tillage erosion underpredict the total magnitude of soil loss (Govers et al., 1996), tillage erosion is not incorporated into nationwide assessments of soil erosion in the U.S. (U.S. Department of Agriculture, 2018). Our analysis does not discount the need to quantify and model soil erosion by water, but highlights that tillage erosion is an important contributor to widespread removal of soil from hilltops in the Corn Belt that warrants greater recognition in soil erosion prediction and soil conservation efforts in the U.S.

Adoption of no-till agriculture greatly reduces soil erosion rates (Montgomery, 2007) and effectively eliminates tillage erosion. However, less than 15% of the acreage of the upper Mississippi River watershed, the heart of the Corn Belt, is farmed with no-till practices for at least three consecutive years (Horowitz et al., 2010). Similarly, nation-wide, only 21% of corn, soybean, cotton, and wheat fields are continuously farmed with no- or strip-till practices (U.S. Department of Agriculture,). Hence widespread adoption of no-till farming methods offers a strategy for preventing further soil loss.

Economic and soil organic carbon losses due to erosion of A-horizon soil

Using county-level harvest data for corn and soybeans, and crop yield reductions associated with severely eroded soils (Fenton et al., 2005), we estimate that loss of A-horizon soils decreases region-wide crop yields by 6±2%, leading to $2.8±$0.9 billion in annual losses across the Corn Belt. Mean annual crop yield decreases, relative to yields from undegraded soils, for each state in the region range from 3±1% to 8±3%, resulting in annual losses of $49 million±$16 million to $793 million±$262 million. The mean crop yield reductions for each county range from 2±1% to 9±3%, equating to annual economic losses of $0.1 million±0.04 million to $32 million±$11 million (Fig. 4c). The average county-level yield reductions per farm range from 2±1% to 9±3%, leading to losses of $300±$100 to $40,000±$14,000 (Fig. 4d), and varies as a function of regional differences in soil parent material, crop yields, and the average farm size per county, which ranges from 10 to 718 ha. Because our analysis only identifies areas where the A-horizon has been completely removed and not areas where the A-horizon has been thinned, which also reduces crop yields (Fenton et al., 2005), our estimates of economic losses are minimum values. Fertilizer is widely applied to degraded soils in the Corn Belt, though it does not restore crop yields to levels measured in non-eroded soils (Lal, 2005). Our analysis of economic losses does not account for the cost of fertilizer inputs required to raise crop yields in degraded soils, but others have indicated over-fertilization of low yielding areas in the Midwest alone costs nearly $0.5 billion a year (Basso et al., 2019).

Global-scale assessments of the influence of soil erosion on the carbon cycle are commonly based on modeled predictions of the extent of soil degradation, which have considerable uncertainty (Sanderman et al., 2017). Our remote sensing method provides a new means for quantifying the land area of degraded soil. Our method relies on the strong

color contrast between the A- and B-horizons of mollisols, but in principle can be applied to other agricultural regions with spectrally distinct soil horizons. In the Corn Belt, we estimate that the regional extent of A-horizon erosion has removed 1.4±0.5 Pg C (10±2 Gg C km^{-2}) from hilltops and hillslopes. Within fields (Li et al., 2018; Papiernik et al., 2009; Ritchie et al., 2007) and fluvial systems (Knox, 1977; Kumar et al., 2018) in the Corn Belt, there is evidence of widespread storage of the soils that have eroded since European settlement. Due to the greater land area, carbon preservation potential is higher in the hummocky topography of the recently glaciated portion of the Corn Belt, where we estimate erosion of A-horizon soils has removed 0.80±0.3 Pg C, whereas 0.6±0.2 Pg C is predicted to have been lost from the area glaciated earlier in the Pleistocene. Burial of these carbon-rich sediments can act as a carbon sink on timescales of decades to centuries (Stallard, 1998) and because the initiation of soil erosion in Midwestern U.S. was relatively recent, there is a high potential for the landscape to preserve carbon in young sedimentary deposits (Doetterl et al., 2016). Hence changes in land use (Hernández et al., 2013; Li, C. et al., 2017) or adoption of farming practices (Lal, R. et al., 2004; Montgomery, David R., 2017) that increase soil organic carbon concentrations in areas that have lost A-horizon soils may generate a net sink for atmospheric CO_2.

Acknowledgments:

We thank Elizabeth Hoy and Jaime Nickeson of NASA and Paul Morin of the Polar Geospatial Center for assistance accessing images. *Maxar data were provided by the Commercial Archive for NASA investigators under the National Geospatial-Intelligence Agency's NextView license agreement. The Polar Geospatial Center*

support was from NSF-OPP awards 1043681 and 1559691. We also thank Skye Wills of the USDA for assistance with access to the Rapid Carbon Assessment database and for sharing soil sample data, Wells Hively and Xia Li for sharing soil sample data, Rebecca McCulley and Jonathan Sanderman for sharing the native prairie soil carbon databases, Yong Tian for providing a spectroradiometer, Jeffrey Kwang, Brendan Quirk, and Caroline Lauth for assistance collecting field samples, Paul Willis and Todd and Jane Gruis for permission to collect soil samples, Oliver Korup for suggesting statistical approaches, David Montgomery for comments on a prior draft, and two reviewers for constructive feedback. The research was supported by NASA (80NSSC18K0747 P0004) and NSF (1653191) grants to Larsen.

Methods

Study area and topographic data

The availability of LiDAR-derived digital elevation models (DEMs) dictated the specific extent of the area of the glaciated, former tallgrass prairie region we analyzed. The LiDAR data were clipped to the Herbaceous Agricultural Vegetation layer from the U.S. Geological Survey Gap Analysis Program (Anonymous), so that the analysis excluded areas with non-agricultural land use. Topographic slope and curvature were calculated as the first and second derivatives of elevation, respectively using a 4 m resolution DEM (*SI Appendix*, Fig. S3). Details of the topographic analysis are described in the *SI Appendix*.

Differentiating between A- and B-horizon soils using satellite imagery

We used the National Geospatial-Intelligence Agency catalog (Neigh et al., 2013) to identify 28 GeoEye-1, Quickbird-2, WorldView-2, and WorldView-3 satellite images showing plowed fields with exposed bare soil (*SI Appendix,* Fig. S4). We analyzed 759 individual cropland fields with a total area of 210 km^2. An example of a study site, which are made up of multiple fields, is shown in *SI Appendix* Fig. S5. The spatial distribution of those fields within the study area was primarily dictated by the availability of imagery with plowed fields, as soil horizons could not be distinguished in fields with no-till or conservation tillage practices that left organic carbon-bearing crop residue exposed at the ground surface. Details of the image pre-processing are described in the *SI Appendix*. For each of the 28 images, we calculated the soil organic carbon index (SOCI = $\rho_{Blue}/(\rho_{Green} \cdot \rho_{Red})$), where ρ is spectral reflectance in the Blue, Green, and Red bands, respectively (Thaler et al., 2019). We demonstrated the validity of the SOCI by examining the relationship between the SOCI and measured soil organic carbon values at five sites (four within the study area), and the R^2 for the correlation ranges from 0.63 to 0.72 (*SI Appendix,* Fig. S6).

The Rapid Carbon Assessment (RaCA), undertaken by the Soil Science Division of the U.S. Department of Agriculture National Resource Conservation Service, collected soil samples at 6,148 sites in the conterminous United States (Wills et al., 2014). For each sample, the soil horizon was designated, and hyperspectral reflectance was measured. Using the laboratory hyperspectral reflectance measurements, we calculated the SOCI at 478 nm (Blue), 546 nm (Green), and 659 nm (Red) for each of the RaCA samples. The RaCA-derived SOCI values are offset from the satellite-derived SOCI values due to atmospheric effects and imperfect radiometric calibration. Hence, the RaCA SOCI values

were scaled to the same range as based on a regression relationship between the satellite-derived and laboratory-measured SOCI values (Thaler et al., 2019).

We evaluated the extent of A- and B-horizon exposure in each image by calculating the probability that a pixel has a SOCI signature of B-horizon soil. For each study site, we performed a bootstrapped logistic regression with 500 iterations using the *sci-kit-learn* module in *python 3.6* to determine the probability that a pixel from a satellite image with a given SOCI value has a B-horizon spectral signature. The soil horizon and SOCI data used in the site-specific logistic regressions were from samples in the RaCA database that were collected within a 50 km radius of individual study sites. We trained the logistic regression model using 20% of the SOCI values for the A- and B-horizon soils. We then tested the power of the logistic regression by using the derived probability function to predict the soil horizon for the remaining 80% of soil samples based on the SOCI value of a sample. To quantify the error in the predicted B-horizon exposure probability values, we generated a probability density function of B-horizon exposure using results from each of the 500 iterations of the logistic regression fit, each based on a different random selection of the 20% of the data used for training (*SI Appendix*, Fig. S7). We further assessed the validity of the logistic regression model by plotting the receiver operator characteristic curve and calculating the area under the curve (AUC) for each site. An AUC value of 0.5 indicates the logistic regression cannot distinguish between classes, and an AUC value of 1.0 indicates the regression perfectly distinguishes between classes. The AUC values for the classification performed in this study range from 0.52±0.15 to 0.96±0.04, and the mean true-positive classification of samples is 88±8%, indicating a high true-positive classification of soil horizon based on the SOCI values (*SI Appendix*,

Fig. S8). The probability functions derived from the bootstrapped logistic regressions were applied to the SOCI raster calculated for each image, and the mean percentage ± 1 S.D. of exposed B-horizon was calculated from the fraction of pixels with ≥ 50% probability of classification as B-horizon.

Effect of moisture on the SOCI and soil horizon classification

Soil moisture causes soils to appear darker and can obscure the spectral signature of soil organic carbon (Nocita et al., 2013). We performed two analyses to assess the potential impact of soil moisture on our estimation of A-horizon soil loss. We evaluated whether soil moisture influenced the spectral reflectance of soils in the images that we used; then we estimated the potential magnitude of a soil moisture impact on our analyses.

The soil surface, which is imaged by satellites, has been shown to become completely dry after three to four days after rainfall (Capehart and Carlson, 1997). To assess the surface soil moisture condition when the images we used were acquired, we analyzed precipitation data from NOAA weather stations nearest to each of our 28 sites. We found that the minimum time between image acquisition and prior rainfall was 20 hours, with a mean of 73 hours, and the mean magnitude of precipitation for all events was 10 mm (*SI Appendix*, Fig. 9). These results suggest that the soil surface would have been dry when the images were acquired. A more detailed description of the precipitation analysis is in the *SI Appendix*.

To determine the influence of soil moisture on the SOCI and the potential impact on the differentiation of soil horizons from spectral data, we conducted a laboratory experiment to measure the spectral reflectance of 26 soil samples with a range of soil organic carbon concentrations collected from the Corn Belt. The reflectance was measured when the samples were dry and again when the samples were saturated with moisture. When moisture is added to the soils, the largest increase in the SOCI occurs for samples with the greatest soil organic carbon concentration (*SI Appendix*, Fig. S10). We used the relationship between soil organic carbon and the maximum change in SOCI due to moisture-saturation to simulate the effect of soil moisture on the threshold distinguishing A- and B-horizon SOCI values. We scaled the RaCA SOCI values by the percent change in the SOCI due to moisture saturation. For each of the 28 sites, our analysis indicates that any addition of moisture to the RaCA samples increases the threshold SOCI value that distinguishes between A- and B-horizons (*SI Appendix*, Fig. S11). When the threshold that accounts for SOCI changes due to addition of soil moisture is applied to the image where the SOCI values have not been adjusted for moisture, a higher fraction of pixels are classified as B-horizon, relative to the threshold based on dry calibration samples (*SI Appendix*, Fig. S12). Because the simulated effect of soil moisture consistently results in an increase in the fraction the pixels predicted to have B-horizon soils, our estimate of A-horizon loss, which is based on dry calibration samples, is a minimum. A detailed description of the moisture experiment and sensitivity analysis is given in the *SI appendix*.

Upscaling soil loss estimates to the Corn Belt area using topographic curvature

Because high-resolution satellite imagery for plowed fields in the Midwest is limited by both spatial coverage and by seasonal crop, snow, and cloud cover, region-wide estimates of B-horizon exposure and A-horizon loss based solely on high-resolution satellite imagery is not possible. However, analysis at four sites throughout the Corn Belt (*SI Appendix,* Figs. S13, S14) indicates that satellite-derived SOCI is related to topographic curvature, where pixels with low SOCI values are observed on topographic convexities and high SOCI values are located in topographic concavities (*SI Appendix,* Fig. S14). Hence, we use the relationship between B-horizon exposure and topographic curvature from the 210 km^2 of analyzed fields to upscale our estimate of soil loss to the entire Corn Belt region. We extracted the SOCI and topographic curvature values from co-located pixels within each of the 28 study sites. Using data from all 210 km^2 of fields, we calculated the fraction of area with SOCI values diagnostic of exposed B-horizon soil. We treated each study site (each made up of 6-109 fields) as an individual measurement and calculated the mean and one standard deviation of B-horizon exposure as a function of curvature for the 28 sites. The relationship between soil loss and curvature (Fig. 3b), which includes uncertainty in B-horizon pixel classification from the bootstrapped logistic regression, was used to calculate the mean and standard deviation of the land area with curvature values indicative of B-horizon soil exposure. Pixels classified as B-horizon soil are disproportionately located where curvature values are < -0.02 m^{-1}. Compared to the analyzed fields, the full Corn Belt study area has a slightly larger fraction of curvature values between -0.02 m^{-1} and 0.02 m^{-1} (*SI Appendix,* Fig. S15), where most erosion is predicted to occur (Fig. 3a). Hence, the estimated percentage of the

Corn Belt with B-horizon exposure is slightly higher than the B-horizon exposure determined for the analyzed fields.

Calculation of economic losses

Our estimate of the magnitude of annual economic losses incurred from the loss of the A-horizon relies on the similarity between yield reductions reported for corn and soybeans in severely eroded soils (Langdale and Shrader, 1982). Corn yields were previously evaluated at 569 sites in 44 counties in Iowa on both glacial till and loess soil parent materials, where categorical measurements of soil erosion were also evaluated (Fenton et al., 2005). In severely eroded soils, where the A-horizon was completely removed, corn yields decreased by 137,300 kg km^{-2} in soils derived from glacial till, whereas yields decreased by 67,100 kg km^{-2} in loess-derived soils. We estimated the total area of loess-derived soils by assuming that all soils south of the last glacial maximum (LGM) ice limit are derived from loess, and the areas north of the LGM ice limit have soils formed from glacial till; soils in the Driftless Area were classified as loess-derived. We calculate that there are 235,632 km^2 and 154,775 km^2 of glacial till- and loess-derived soils in our study area, respectively. The area of till-derived soils that no longer has A-horizon is estimated to be 80,114±28,275 km^2 and the area of loess-derived soils with no A-horizon is estimated to be 52,623±18,573km^2. Based on the reductions in corn and soybean yields due to complete A-horizon loss for each parent material, predicted areas of A-horizon loss (mean loss ± 1 S.D.), hectares planted of corn and soybeans (*SI Appendix*, Fig. S16), and the average corn and soybean prices from 2012-2017, we estimate mean economic losses for each county. The uncertainties we report are based on

the 1 S.D. uncertainties in the percentage of A-horizon soil loss for each county. We estimate total loss with the glacial till-derived soils to be $1,683 million±$575 million and losses from loess-derived soils to be $762 million±$246 million. The mean per farm economic loss for glacial till-derived soils is $15,200±$5,200 and is $5,900±$1,900 for loess-derived soils.

Estimation of soil organic carbon erosion

To estimate the magnitude of soil organic carbon erosion, we multiplied the mean value of carbon stocks (10.5 billion g C km^{-2}) in the upper 30 cm of soil samples collected on native prairie hillslopes (Sanderman et al., 2017) from locations with convex topography (curvature values between -0.01^{-1} and $-0.09\ m^{-1}$) by the area of A-horizon loss. We also compiled published measurements of A-horizon thickness for native tallgrass prairies within our study area (*SI Appendix* Table S1). The mean A-horizon thickness was 37 cm, indicating a carbon stock value measured to 30 cm depth reasonably approximates the A-horizon carbon stock. The loss of 30 cm of soil is also consistent with our spectral measurements of soils on convex hilltops in a prairie and adjacent field in Iowa (*SI Appendix* Fig. S1).

Data Availability

Data are cataloged at the Oak Ridge National Laboratory Distributed Active Archive Center (https://doi.org/10.3334/ORNLDAAC/1774). The archive includes spatial raster data for topographic metrics (elevation, slope, curvature), soil organic carbon index values, and the probability of B-horizon soil. Spatial vector data and tabular data with county-, state-, and farm-level erosion and economic loss values are also archived. The

soil organic carbon index values, derived from the RaCA samples, and used to develop the logistic regression and receiver operator characteristic curve for each site (such as those shown in *SI Appendix* Fig. S8) are also archived.

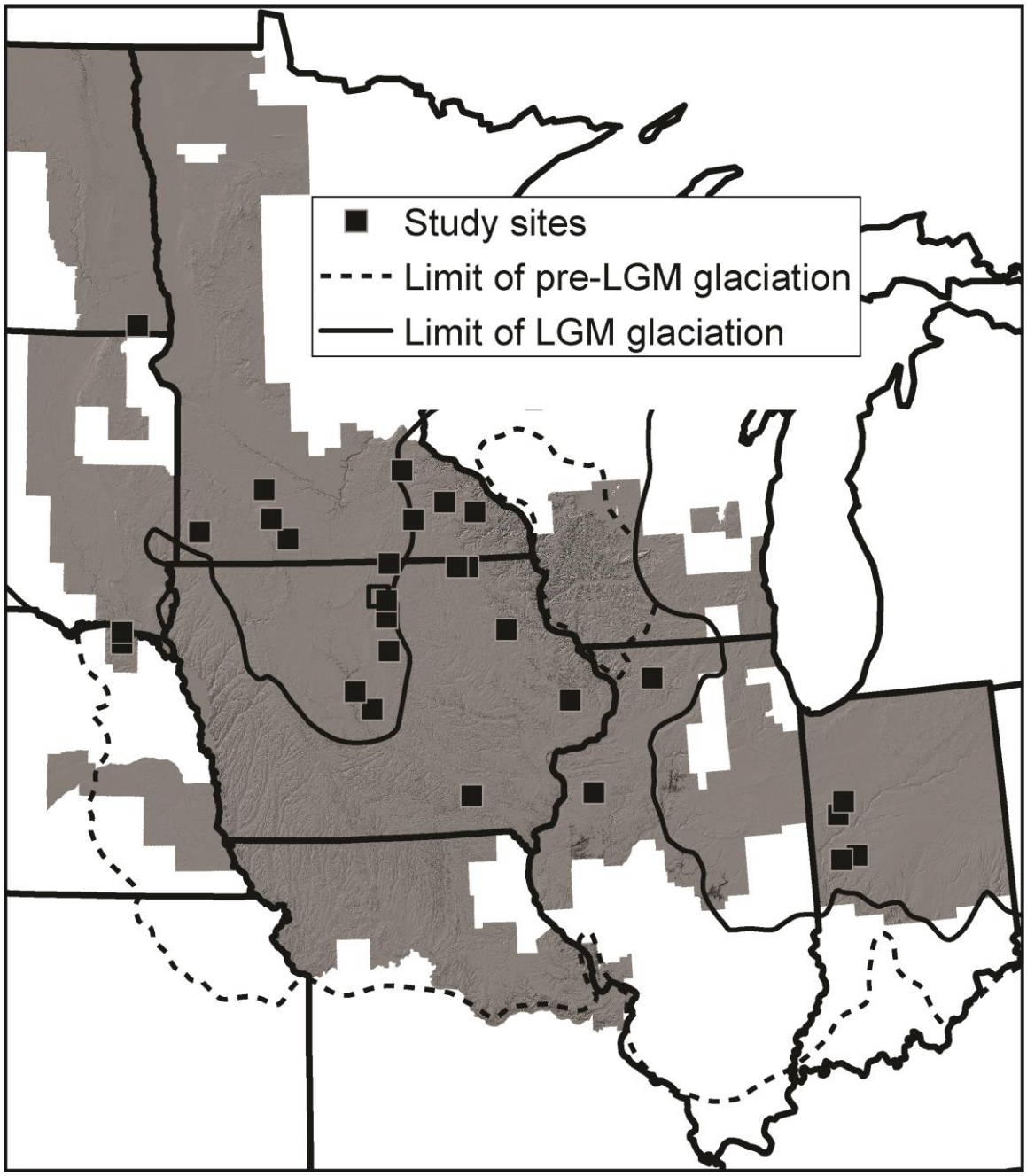

Fig. 4.1. Study area in the Midwestern U.S. The study area is defined by the spatial extent of LiDAR topographic data (gray hillshade). The squares show the locations of 28 sites where 210 km^2 of imagery from plowed agricultural fields with bare soil were analyzed. The open square indicates the location of the field shown in Fig. 2. The glacial extent prior to the Last Glacial Maximum (LGM) and the extent during the LGM are shown as dashed and solid lines, respectively.

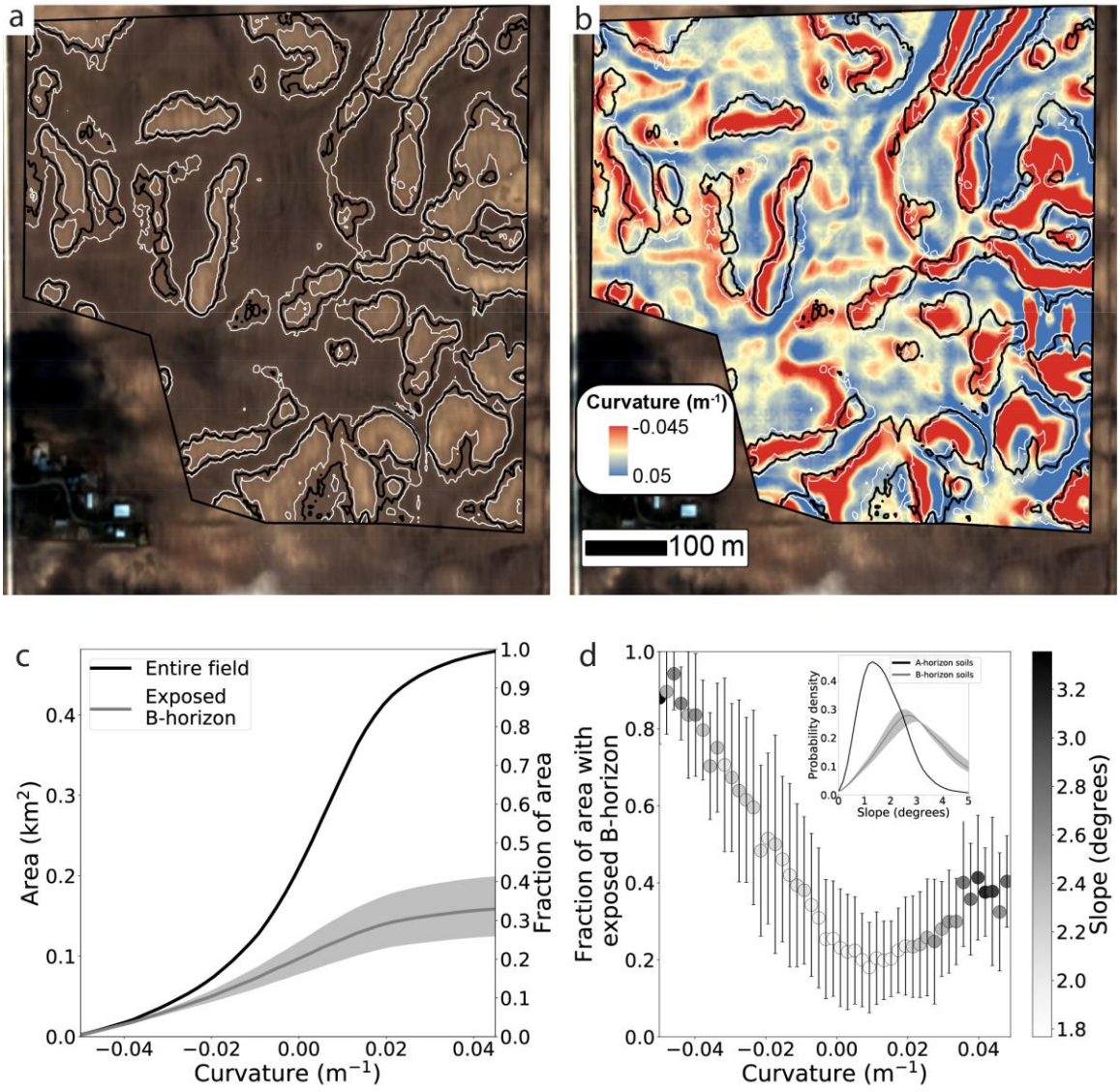

Fig. 4.2. Calculation of A-horizon loss and topographic curvature. a) True-color image of a field near Clear Lake, Iowa (open square in Fig. 1) (copyright 2013 Maxar, Inc.); Black polygons surround light-colored areas predicted to have exposed B-horizon soil. Gray polygons indicate ±1 standard deviation (S.D.) of the predicted area of B-horizon exposure. b) Topographic curvature map where red pixels denote negative curvature (convex hillslopes) and blue pixels denote positive curvature (concave hillslopes). c) Cumulative fraction of area with curvature values for the entire field (black line) and curvature values for the area with exposed B-horizon soil (gray line); 34±7% of the area is exposed B horizon soil. Gray shading shows the ±1 S.D. prediction of B-horizon exposure. d) Mean (±1 S.D.) of the fraction of pixels with a spectral signature of B-horizon soils versus topographic curvature, shaded by median topographic slope per curvature bin, which shows that exposure of B-horizon soil occurs predominantly on convex topography. Inset shows the probability density of topographic slope values for A-horizon pixels and for B-horizon pixels, and gray shading shows the ±1 S.D. prediction of B-horizon exposure.

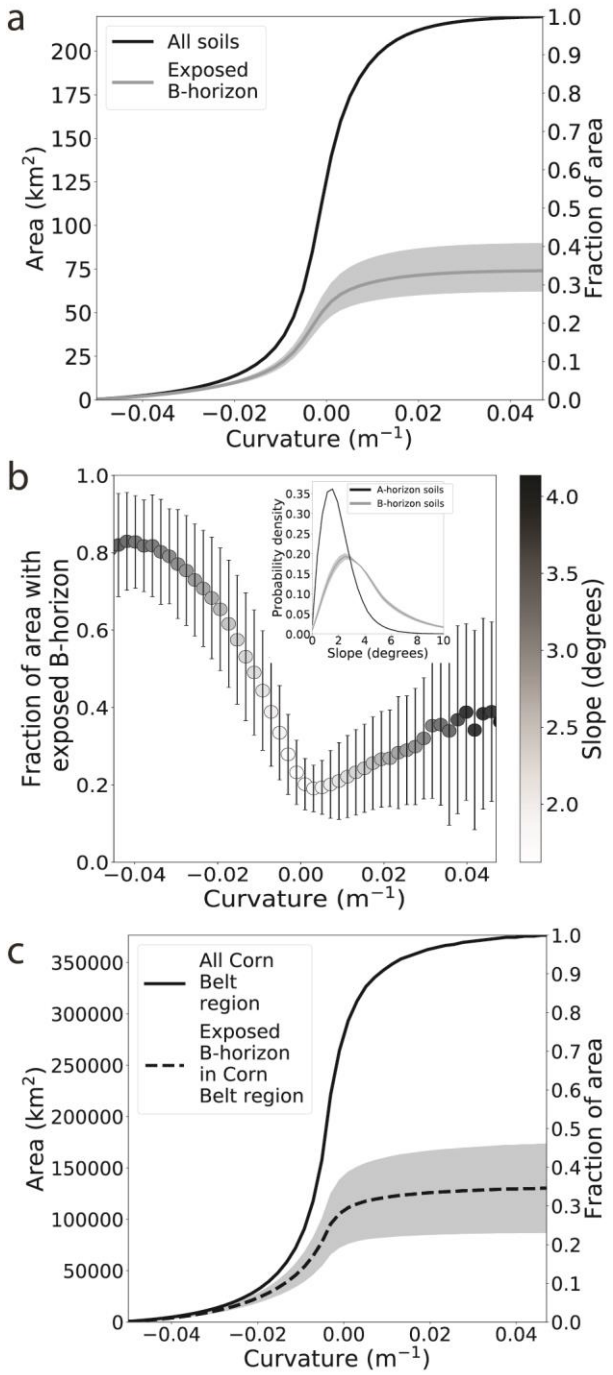

Fig. 4.3. Regional-scale A-horizon loss estimate for the Corn Belt. a) Cumulative distribution of topographic curvature for all (combined A- and B-horizon) soils (black line) and B-horizon soils (gray line) for the 210 km^2 of fields that were analyzed, which

indicate 34±7% of the soil exposed in fields is B-horizon; gray shading shows the ±1 S.D. prediction of B-horizon exposure. b) Mean (±1 standard deviation; S.D.) of the fraction of pixels with a spectral signature of B-horizon soils versus topographic curvature for the 210 km^2 of fields that were analyzed. Across all sites, convex topography (negative curvature) has experienced the highest proportion of B-horizon exposure and A-horizon loss. Symbol color denotes the median slope angle for each curvature value. Inset shows the probability density of topographic slope values for A-horizon pixels and for B-horizon pixels, and gray shading shows the ±1 S.D. prediction of B-horizon exposure. c) Cumulative distribution of area as a function of topographic curvature for the entire Corn Belt study area (solid line) and for B-horizon soils (dashed line); gray shading shows the ±1 S.D. prediction of B-horizon exposure. Our calculation indicates 35±11% of the landscape has completely lost A-horizon soil to erosion, exposing underlying B-horizon soil.

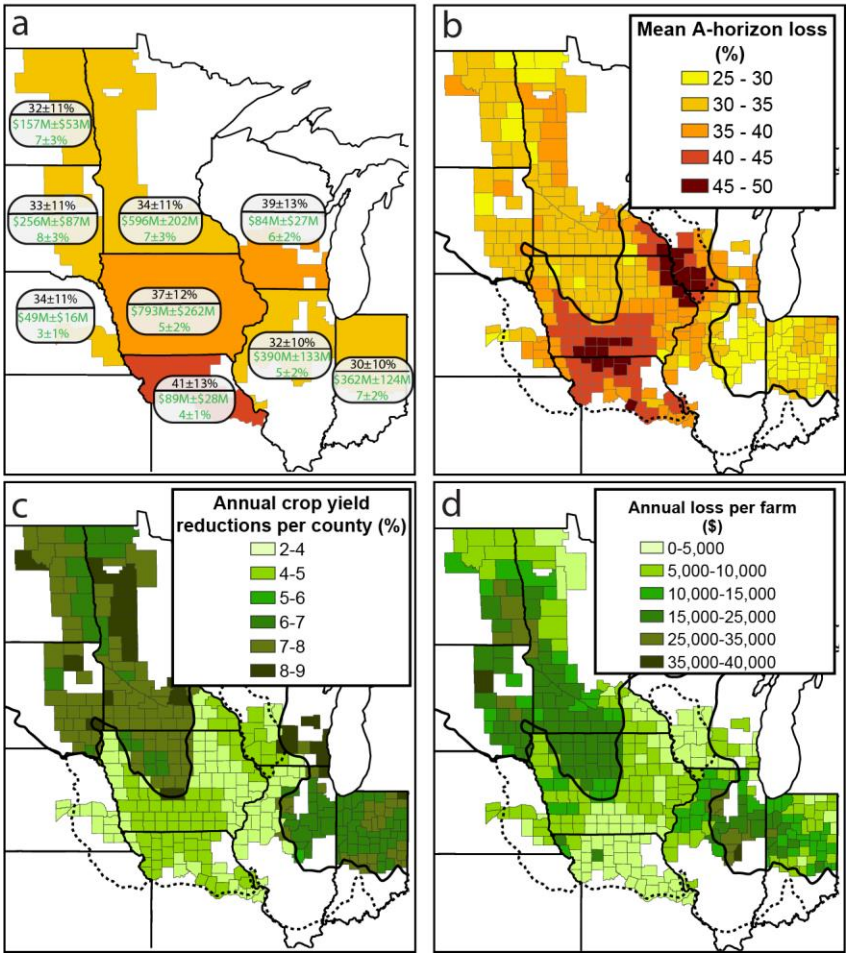

Fig. 4.4. A-horizon loss and associated economic losses within the Corn Belt. a) Aggregated percent A-horizon loss (black text) and annual economic losses expressed in millions of dollars (M) and as a percentage relative to un-eroded soils (green text) for each state within the region (color scale is the same as in b). b) Percentage of A-horizon loss for each county. c) Percent annual economic losses for each county relative to predictions for un-eroded soils. d) Predicted mean annual economic losses per farm in each county. The LGM and pre-LGM glacial extent, which define the distribution of glacial till- and loess-derived soils are shown as solid and dashed lines, respectively.

CHAPTER 5

RATES OF HISTORICAL ANTHROPOGENIC SOIL EROSION IN THE MIDWESTERN U.S.

ABSTRACT

Erosion degrades soils, reduces crop yields, and diminishes ecosystem services. The total thickness of soil that has been lost since the initiation of farming is unconstrained in most landscapes, hindering the assessment of soil loss trends. In the Midwestern U.S., erosion has caused native prairie remnants to become perched above surrounding farmland, providing an opportunity to measure historical soil loss. Here we use high-resolution topographic surveys conducted across erosional escarpments at the boundary between 20 prairies and adjacent fields and show the median depth of soil loss ranges from 0.04-0.69 m, corresponding to erosion rates of 0.2–4.3 mm yr^{-1}. We used an association between measured soil loss and topographic curvature to predict regional historical erosion rates, which are exceeded by U.S. Department of Agriculture estimates of current erosion rates for 60% of agricultural land, suggesting erosion rates have not declined from historical levels for the majority of cropland.

Introduction

Conventional agricultural practices have accelerated soil erosion rates, resulting in widespread soil degradation throughout the world's agricultural regions (Montgomery, D. R., 2007). Soil degradation diminishes soil fertility by removing organic matter and nutrients (Pimentel, 2006), which leads to reductions in crop yields (Lal, 2004), increased agricultural production costs (Pimentel et al., 1995), and negative off-site effects such as increased sedimentation and nutrient export to downstream waterbodies (Pimentel et al.,

1995). In the United States, recognition of the high costs of soil erosion in the early 20th century led to the development and implementation of soil conservation practices (Bennett, 1948), which had the goal of reducing rates of soil erosion to a level at which soil fertility can be maintained (Li et al., 2009; Skidmore, 1982). Field trials have demonstrated the efficacy of soil conservation efforts (Pimentel et al., 1976; Steiner, 1987), yet it is unclear whether the soil conservation movement has led to a reduction of region-wide soil erosion in the U.S. Although many studies have investigated erosion rates, such studies tend to integrate over short times scales of a few decades or less (García-Ruiz et al., 2015) (fig. S1). Remote sensing estimates indicate there has been widespread historical soil loss; roughly 30% of the cultivated area of Midwestern U.S. has completely lost A-horizon soil since the initiation of cultivation (Thaler et al., 2021). However, whereas remote sensing and other soil survey-based methods (Jelinski and Yoo, 2016) can provide information on the areal extent of degraded soil, such methods cannot quantify the total depth of soil loss since the initiation of farming or historical soil erosion rates. Hence in the Midwestern U.S., and other agricultural regions, historical erosion rates are poorly constrained, impeding determination of temporal trends in soil loss or the degree to which conservation efforts have reduced erosion rates below historical levels.

Rates of soil loss have been estimated from sediment yield studies, where a mass balance approach is applied by assuming that the volume of sediment delivery is proportional to eroded soil upstream (De Vente et al., 2007). Erosion of soil due to agriculture increases river sediment loads and sediment accumulation rates. For example, rapid expansion of agriculture across North America increased sedimentation rates 10-

fold compared to geologic rates (Kemp et al., 2020). In the Midwestern U.S., decreased sediment yields have been observed since soil conservation efforts began in the 1940s (Trimble, S. W., 1981). However, the ability to directly relate fluvial sediment yield to erosion rates at cultivated upland sites is obfuscated by internal basin dynamics, such as sediment storage in floodplains and internally drained basins, which are common in hummocky post-glacial landscapes (Lai and Anders, 2018). For example, sediment yields in Coon Creek, a long-term research site in Wisconsin, USA, remained stable from 1853-1993, while alluvial storage within the basin decreased during the same period, indicating that measurements of sediment yield do not capture upland erosional processes (Trimble, Stanley W., 1999). Similarly, in the Minnesota River watershed, fluvial sediment yields primarily reflect streambank and bluff erosion, and cannot be used to infer erosion rates on agricultural uplands (Gran et al., 2009). Furthermore, sediment yield studies do not provide information on the total magnitude of historical soil loss, and such studies often rely on model predictions to infer historical changes in upland erosion rates (Trimble, Stanley Wayne and Lund, 1982).

The U.S. Department of Agriculture National Resources Inventory (USDA NRI) (U.S. Department of Agriculture, 2018) provides a sub-decadal assessment of soil erosion rates at specific sites throughout the U.S. based on climate, soil property, and land use data. Site characteristics are used as parameters for the Revised Universal Soil Loss Equation (RUSLE) (Nearing, M. A. et al., 1989; Renard et al., 1997) and the Wind Erosion Equation (Woodruff and Siddoway, 1965), which provides estimates of sheetwash and rill and wind erosion, respectively. The USDA NRI five-year assessments of soil erosion suggest that erosion rates have been decreasing (U.S. Department of

Agriculture, 2018); however, these assessments of erosion do not incorporate models for tillage or gully erosion, which can be primary drivers of soil transport (Nearing, Mark A. et al., 2017; Thaler et al., 2021). The NRI estimates of soil loss trends have occurred every 5 years from 1982 to 2017, (U.S. Department of Agriculture, 2018) but these assessments do not determine whether present-day erosion rates have declined relative to independently estimated historical erosion rates. Historical and modern soil erosion rates in the U.S. are poorly constrained (Trimble, S. W. and Crosson, 2000); hence, whereas the NRI assessments suggest soil loss has declined over the last several decades, it is unclear whether erosion rates have declined relative to historical levels. Here, we relate field measurements of the depth of soil loss to topographic curvature and generate the first regional estimates of soil erosion rates in the Midwestern U.S. that span from the initiation of agricultural cultivation in the mid-1800s to the present-day. We then compare our historical erosion rates against USDA NRI values for each county in the Midwest to assess whether erosion rates have declined from historical levels.

Study Area

The Midwest is an important agricultural region that produces most of the corn and soybeans in the U.S. (U.S. Department of Agriculture, 2017). Prior to agricultural development in the mid-late 1800s, the ecosystem of the Midwestern U.S. was dominated by tallgrass prairie (Sampson and Knopf, 1994); however, within decades of the initiation of cultivation, the prairies were converted to agricultural fields, and today less than 0.1% of the prairie remains (Sampson and Knopf, 1994). Although most of the land in the

Midwestern U.S. has been converted to agricultural fields, native prairie remnants, which were spared from cultivation, are preserved throughout the landscape (Fig. 1).

When the prairie remnants are located up-gradient of adjacent agricultural fields, an escarpment is commonly present at the boundary between prairies and fields because agriculturally-accelerated erosion within the fields outpaces natural erosion in the prairies (Fig. 2). Because the native prairies have not been anthropogenically altered, they preserve the pre-settlement topography; natural erosion rates in the prairies occurs at such low rates (0.047 mm yr^{-1}) (Jelinski et al., 2019) that the topography can be considered static over post-settlement timescales. Hence, we measured the height of the erosional escarpment to quantify the magnitude of soil loss that has occurred since cultivation began between approximately 1850 and 1900 C.E. We use the measurements to estimate the historically-averaged erosion rate and combine the soil loss data with high-resolution topographic data (see Materials and Methods) to extrapolate predictions of historical erosion rates for agricultural fields in the Midwest.

Results

The median thickness of soil that has been eroded from the 20 fields ranges from 0.037 m to 0.69 m, indicating median time-integrated erosion rates ranging from 0.002 mm yr^{-1} to 4.3 mm yr^{-1} (Fig. 3). The greatest magnitudes of soil loss, and hence the largest integrated erosion rates, were measured in areas with the most convex topography ($\nabla^2 z < 0$). At eight transects in areas within topographic concavities, the elevation of the field is higher than the elevation of the prairie due to soil deposition, and these transects are indicated by negative soil loss and erosion rate values (Fig. 4a,b). Historical soil loss

is linearly correlated with topographic curvature and data from all transects at the 20 field sites, with a coefficient of determination (R^2) of 0.3 and mean ± 1 standard deviation (S.D.) slope and intercept values of -28.9±3.1 m^2 and 0.24±0.01 m, respectively.

Binning the soil loss measurements by evenly spaced curvature bins and assessing the error in the regression parameters using the Monte Carlo simulations (Fig. 4c) (see Materials and Methods) resulted in a coefficient of determination (R^2=0.8), while producing similar mean slope (-30.1±13 m^2) and intercept values (0.23±0.09 m). Similarly, there is a linear relationship between erosion rate and topographic curvature (Fig. 4b), where the slope of the regression relationship defines a coefficient (D) that describes the efficacy of diffusion-like topographic evolution caused by soil erosion. Our analysis indicates the value of D is 0.19±0.02 m^2 yr^{-1} when each transect is considered a separate measurement and 0.18±0.08 m^2 yr^{-1} when the data are binned by curvature and the error in the slope is estimated using the Monte Carlo simulations (Fig. 4d).

The regionally estimated total mass of soil eroded since cultivation began in the 16,503,300 ha of convex topography that we analyzed is $55.7 \times 10^9 \pm 20.7 \times 10^9$ metric tons, equating to a historically averaged erosion rate of 21.7±8.1 t ha^{-1} yr^{-1} (1.8±0.7 mm yr^{-1}). An example field where we calculate soil loss is shown in Figure 5. Averaging the soil loss over the entire area of farmland (both convex and concave topography, 62,063,244 ha) yields an average historical erosion rate of 5.8±2.1 t ha^{-1} yr^{-1} (0.48±0.2 mm yr^{-1}). County-level soil loss estimated using the relationship between soil loss and topography for 408 counties in our study area range from 0.19±0.08 (0.02±0.1 mm yr^{-1}) to 12.7±5.7 t ha^{-1} yr^{-1} (1.1±0.48 mm yr^{-1}), whereas county-level fluxes estimated from the NRI assessment range from 0.91 to 23.2 t ha^{-1} yr^{-1} (Fig. 6 and fig. S2). NRI-based soil erosion

rates from the last five years exceed the historically-averaged values for 68% of counties and 60% of total cropland in the Midwest. Of the 130 counties where the historical erosion rate is greater than the NRI rate, 115 counties are north of the last glacial maximum (LGM) extent. The mean historical erosion rate for counties north of the LGM extent is 5.6±1.9 t ha^{-1} yr^{-1} (0.47±0.16 mm yr^{-1}), and the mean historical erosion rate for counties south of the LGM extent is 5.4±2.1 t ha^{-1} yr^{-1} (0.45±0.18 mm yr^{-1}). The mean NRI-based erosion estimates north and south of the LGM extent are 4.0 t ha^{-1} yr^{-1} (0.3 mm yr^{-1}) and 11.1 t ha^{-1} yr^{-1} (0.93 mm yr^{-1}), respectively.

Discussion

Conversion of land from native tallgrass prairie to cultivation-based agriculture has resulted in decimeters of soil loss in the Midwestern U.S. The historical erosion rates documented by our surveys average over timescales of ~100 to ~170 years, depending on the site. The rates we measure are consistent with previously documented soil erosion rates measured in the Midwest, which range from 0.14 to 7.7 mm yr^{-1} (Fig. 3c). However, the previously documented erosion rates typically are based on only a few decades of measurement (fig. S1) during the mid-20th century. The similarity in the historically-averaged and previously documented 20th century, decadal-averaged erosion rates suggests the Midwestern landscape eroded at high rates in the century and a half since the initiation of farming.

To set a goal for reduction of soil degradation, the USDA has assigned a soil loss tolerance (T) value for a given soil, which is defined as the “maximum rate of annual soil

loss that will permit crop productivity to be sustained economically and indefinitely" (U.S. Department of Agriculture, 2018). T values are based on multiple characteristics including soil physical properties, and assumptions regarding soil formation rates (Skidmore, 1982). In the U.S., T values range from 2.2-11.2 t ha^{-1} a^{-1}, which is equivalent to 0.4-1 mm yr^{-1}, assuming a soil bulk density of 1,200 kg m^{-3} (U.S. Department of Agriculture, 2018). The T value for the soils at all of our sites is equivalent to 1 mm yr^{-1} (Fig. 3), and it has been argued that such values are too high to adequately reduce soil loss to a sustainable level by balancing soil loss and formation (Johnson, 1987; Li et al., 2009). The median historical erosion rate exceeds the T value at 15 of our 20 field sites, indicating that soil loss at these sites has outpaced even the most erosion-permissive soil conservation target set by the USDA for more than a century. The topography of the 20 field sites is relatively flat, with slope angles measured at 3 arc-second (~90 m) pixel scale values from 0.3 to 7.6 degrees. The Kalsow site has the flattest topography, with a mean topographic slope of 0.21 degrees, which might explain the low erosion rates at the site. However, the other four sites with erosion rates lower than the T value, Loda, Dinesen, Harker, and Sheppard, have mean topographic slopes of 0.63, 2.5, 0.95, and 1.1 degrees, respectively, which are greater slopes than sites where erosion rates outpace the T value, indicating that topography alone does not explain the relatively low erosion rates at the sites. Nor does soil parent material explain the low erosion rates, as soils at these five sites are formed from both loess and glacial till, the two dominant soil parent materials in the Midwest. Hence, it is likely that differences in agricultural practices may contribute to differences in historical erosion rates across the sites, although data on the history of farming practices are not available to test that hypothesis.

The mean 3 arc-second slope value of 1.7 degrees for all sites is equivalent to the 47th percentile of slope values measured globally (Larsen et al., 2014). However, the anthropogenic erosion rates in the agricultural fields exceed the 99th percentile of long-term, pre-agricultural erosion rates inferred globally from *in situ*-produced cosmogenic ^{10}Be and slope data (Larsen et al., 2014). Globally, only the steepest topography (slopes > 28 degrees) has natural, background erosion rates equivalent to those we measured in the Midwest (Larsen et al., 2014). Hence due to agricultural practices, the relatively gentle topography of the Midwest is eroding at rates comparable to Earth's major mountain belts, such as the Himalaya.

The soil erosion we measure at each site is the sum of soil loss caused by all erosion processes, including rainsplash, overland flow, wind, and tillage. However, the correspondence between topographic curvature and our measured erosion rates indicates that tillage erosion is a primary driver of erosion, particularly since convex ridgetop sites that we surveyed have little upslope accumulation area to generate overland flow but have lost decimeters of soil. At the 20 paired prairie-field sites, we find the greatest depth of historical soil loss and the highest time-averaged erosion rates occur on the most convex hilltops (Fig 4a,b). The large soil loss we measure on convex topography is consistent with the widespread erosion of A-horizon soil observed on convex hilltops (Thaler et al., 2021), which provides further evidence that tillage erosion *(12)* is a primary driver of soil degradation in the Midwest. The D value calibrated from our measurements of erosion rate and topographic curvature (0.19±0.02 m^2 yr^{-1}) (Fig. 4b) is comparable to previously measured diffusion coefficients for tillage erosion, which range from 0.03 to 0.52 m^2 yr^{-1} (Van Oost et al., 2006). Hillslopes affected by tillage become

less convex through time and since our estimate of D relies on the linear relationship between erosion rate and the modern topographic curvature, our estimate of D is a slight overestimation. However, the D values we estimate are one to three orders of magnitude greater than values measured in non-agricultural settings (Fernandes and Dietrich, 1997), which indicate agriculture has increased erosion rates in the Midwest by orders of magnitude.

Within the Midwestern U.S., sub-decadal scale estimates of soil erosion from the USDA NRI assessment indicate that soil erosion rates decreased by 34% from 1982 to 2015 (U.S. Department of Agriculture, 2018). However, the NRI estimates of erosion are higher than the historically averaged erosion rates we predict for 60% of the cropland within our study area. Of the 130 counties where the historical erosion rates are higher than NRI-predicted rates, 115 are in the recently glaciated upper Midwest (fig. S3). Soil characteristics in the Midwest vary as a function of glacial history; soils within recently glaciated terrain are derived from glacial till, whereas soils are derived from fine-grained loess deposits outside of the limits of the LGM ice margin. The RUSLE-based NRI soil loss predictions incorporate a soil erodibility factor that is based on soil texture and organic matter content, both which are influenced by the glacial history, resulting in lower erodibility factors north of the LGM ice limit (fig. S4) (Soil Survey Staff, 2019), where soils tend to be coarser-grained and have higher organic carbon content. The NRI hence predicts soil loss rates are higher by at least a factor of 4 to the south versus north of the LGM ice limit (fig. S2b). However, our measurements indicate soil loss rates are not significantly different to the north and south of the LGM ice extent. We attribute the similarity in our measured values of soil loss rates north and south of the LGM ice limit

to tillage erosion. Tillage erosion, which is not included in RUSLE-derived erosion estimates used by the NRI, is predominately influenced by topography and farming practices rather than by soil properties (Van Oost et al., 2006). Hence, at least with respect to convex topography, spatial patterns in erosion rates attributable to parent materials may be much smaller than predicted by the NRI.

More broadly, although our method and the NRI use different assumptions to predict region-wide soil loss rates, our findings suggest that NRI-based estimates of recent erosion rates exceed historical agricultural erosion rates on 60% of the cropland in the Midwestern U.S, even without inclusion of estimates of tillage erosion, which is dominant within the landscape (Thaler et al., 2021). Although the NRI methodology has been debated (Trimble and Crosson, 2000), the NRI surveys indicate that cropland soil erosion rates have decreased in recent decades (U.S. Department of Agriculture, 2018). The trend of decreasing erosion rates is primarily because the NRI began incorporating the effects of conservation agricultural practices, which were not included prior to 1997 (U.S. Department of Agriculture, 2018). However, whereas adoption of soil conserving practices is a step in the right direction, the NRI predicts that soil loss rates in the Midwest are the highest of any region of the U.S. (U.S. Department of Agriculture, 2018), and our analysis suggests progress has not been great enough to reduce erosion rates below historical levels, which are markedly higher than T value targets, for the majority of cropland in the Midwest. Although political and social barriers remain (Amundson, Ronald and Biardeau, 2018; Schlesinger and Amundson, 2019), incentives that lead to widespread adoption of conservation methods that are effective at reducing soil loss, such as no-till (Montgomery, 2007) and soil regenerative farming

(Montgomery, David R., 2017) will be required to reduce erosion rates in the Midwest to levels that can sustain soil productivity and ensure long-term prosperity (Amundson, R. et al., 2015).

Materials and methods

We used a real-time kinematic GPS to conduct cm-scale accuracy topographic surveys across the prairie-field boundary at 20 sites throughout the Midwest (Fig. 1a). A minimum of ten transects were surveyed at each site, and transect locations were selected to span the range of topographic curvature at each site. At each transect, the height of the erosional escarpment was determined by using linear regression to extrapolate the elevation of the prairie surface across the erosional escarpment (Fig. 2). The elevation at the base of the escarpment was determined by fitting a linear regression to survey points in the field. The thickness of eroded soil was calculated as the difference between the two regression lines at the base of the erosional escarpment between the prairie and the field. Use of the regression relationships accounts for the slope of the ground surface, resulting in more accurate determination of the thickness of soil loss relative to simply comparing the elevation at the edge of the prairie versus the edge of the field, which would over-estimate soil loss. Examples of escarpments, transects, and soil loss estimations are shown in Fig. 2. In a small number of cases, we measured deposition along the prairie-field boundary.

We estimated a soil erosion rate (Fig. 3) by dividing the thickness of eroded soil by the time since the initiation of cultivation. Several of the prairies are the site of pioneer cemeteries, and at these sites, the date of the earliest gravestone was assumed to coincide

with the initiation of cultivation. For the non-cemetery sites, we assumed that cultivation began when the ownership of the land parcel was transferred from U.S. government to private individuals, based on records from the U.S. General Land Office Records (Bureau of Land Management,). Dates of land transfer and hence initiation of cultivation range from 1846 to 1902. 16 of the 20 agricultural fields where we measured soil loss are still cultivated for row crop agriculture. The fields at Loda, Judson, and Steinauer have been removed from row crop production within the last decade, but the exact year is unknown for each site. Therefore, we assumed that cultivated ceased in 2019 when we surveyed the fields, which leads to a conservative estimate of the erosion rate at each site because the integrated time is longer. However, the end of cultivation at the McKnight field is better constrained to the late 1960s, leading to an integrated erosion period of ~100 years.

To contextualize our estimates of soil erosion, we compiled estimates of previously published soil erosion rates calculated in croplands within the Midwestern U.S. (Fig. 3, Data repository). We further contextualize the erosion rates at each of the sites within a global perspective by comparing the topographic slope and erosion rates for each field site against a global dataset of slope and *in situ*-produced ^{10}Be denudation rates (Larsen et al., 2014), which reflect long-term, pre-agriculture erosion rates (Vanacker et al., 2007). For each agricultural field that we surveyed, we calculated topographic slope using 3 arc-second spatial resolution digital elevation models (DEM) derived from the Shuttle Radar Topography Mission (Farr et al., 2007) global dataset. Then, we determined the global percentile within which the median erosion rate and mean local topographic slope for each site lies using results from ref. (Larsen et al., 2014).

LiDAR point cloud data were used to generate DEMs for each site, ranging from 0.15 to 0.5 m spatial resolution. We used a high pass gaussian filter, with a window size of 4 m, on the DEMs to remove small-scale surface roughness caused by tilling, while retaining the larger-scale landform topography. Because the gaussian filter samples from a spatial averaging window, the filter has the potential to greatly change the elevation values near the boundary between the prairie and the field. To avoid this, we masked out the boundary before applying the filter. We then calculated topographic curvature for each filtered DEM and extracted the curvature values for each transect location.

We fit a linear regression between the thickness of eroded soil and topographic curvature (Fig. 4a) data from all sites to derive a relationship that we used to scale-up estimates of the thickness of soil loss throughout cultivated lands in the Midwestern U.S. At many of the field sites, there is little variation in topographic curvature, and soil loss, along the escarpment, resulting in a dense clustering of measurements between curvature values of -0.01 m^{-1} and 0 m^{-1} (Fig. 4a,b). To account for the density of points, we binned the curvature values into ten evenly spaced bins, and for bins with >four soil loss measurements, we calculated the mean and standard deviation (S.D.) soil loss thickness (Fig. 4c). We assessed the uncertainty in the slope and intercept of the regression line through the binned data using a Monte Carlo simulation. For each bin, we assumed a normal distribution of 500 erosion rate measurements with a mean and S.D. equal to the mean and standard deviation of the binned data. For 10,000 iterations of the Monte Carlo simulation, we calculated the slope and intercept of a regression line fit through randomly selected values from each bin and calculated the mean and S.D. of the simulated regression slopes.

We calculated topographic curvature from LiDAR-derived topographic data at 4 m pixel resolution throughout the Midwestern U.S (Fig. 1), as 4 m is the optimal spatial resolution to calculate curvature for fields in this region (Thaler et al., 2021). The topographic dataset was clipped to include only agricultural croplands using the Herbaceous Agriculture raster from the USGS Gap Analysis dataset (Anonymous). Waterways were removed from the DEM using the National Hydrography Dataset (Geological Survey, (U. S.), 2004), transit lines (roads, railways, etc.) were removed using the National Transportation Dataset (U.S. Geological Survey, 2014), and property boundaries, which contain fences, were removed using the Agricultural Conservation Planning Framework dataset (Tomer et al., 2017).

Because our surveys indicate soil loss primarily occurred on convex hillslopes, we only predicted soil loss on convex topography (topographic curvature <0), resulting in an area of 16,503,300 ha (165,033 km^2). For each curvature pixel, we predicted the total soil loss since cultivation and the uncertainty. Within each county in the study area, we estimated the thickness of eroded soil, which we converted to a mass of soil loss using an assumed uniform soil bulk density of 1,200 kg m^{-3}, and the total mass of soil eroded from convex areas within cultivated lands was summed for each county. The total mass of soil loss was converted to an erosion rate by diving by the period of erosion (155 years), which is the mean period of erosion for all our field locations. An example of the soil depth loss rasters with roads, waterways, and field boundaries removed and the calculation of mass loss is shown in Fig. 5.

For each county within the study area, we also calculated the total yearly soil flux (t ha yr^{-1}) estimated by the 2015 USDA NRI soil erosion assessment, which are annual

estimates of erosion from 2000 to 2015 (U.S. Department of Agriculture, 2018). The NRI erosion estimates are derived by calculating the RUSLE (Renard et al., 1997) at target cells, which contain a surveyed field site. The soil flux estimates are then interpolated to 2.5 km^2 spatial resolution using all target cells within 80 km of interpolated cells. We compared our estimates of the annual county-level soil flux derived from our soil loss estimates to the NRI county-level estimates by dividing our county-level estimates by the total NRI area within each county. To assess the influence of soil parent material on our estimated erosion rates and the NRI erosion rates, we divided the study area into counties with till-derived soils and counties with loess-derived soils, which we assume to correspond to areas north and south of the last glacial maximum (LGM), respectively (fig. S2, S3).

Preferential erosion of hilltops within the fields adjacent to the native prairies indicates that tillage erosion is the dominant driver of soil transport in the region (Thaler et al., 2021). Tillage erosion is the movement of soil by repeated tillage operations (Van Oost et al., 2006), in which soil is preferentially removed from topographic convexities and deposited in topographic concavities. We used our estimates of the time-integrated soil erosion rate and measurements of topographic curvature to estimate the diffusion coefficient for tillage erosion in the region. Tillage erosion can be modeled as a diffusion-like erosion process,

$$dz/dt = D\nabla^2 z \qquad (1)$$

where dz/dt is erosion rate averaged since cultivation began [$L\ T^{-1}$], D is a diffusion coefficient [$L^2\ T^{-1}$] that integrates tillage direction, depth, and soil physical characteristics, and $\nabla^2 z$ is the Laplacian operator of z, or topographic curvature [L^{-1}], a

measure of landscape convexity. By rearranging eq. 1, D can be estimated by calculating the slope of the regression line fit to the erosion rate calculated from the GPS surveys (dz/dt) and topographic curvature ($\nabla^2 z$) data (Fig. 4b). D and its ±1 standard error (S.E.) uncertainty were calculated from the slope of the regression line through the erosion rate and curvature data from all sites (Fig. 4b). We also performed the same Monte Carlo analysis for regression line fit between the erosion rate and topographic curvature at the field sites (Fig. 4d). We then assessed the uncertainty in our estimates of D using the ±1 S.D. of the slope parameter derived from the Monte Carlo simulation.

ACKNOWLDEGEMENTS

We thank Joe McGovern, Ryan Schmidt, and Erin Van Waus of the Iowa Natural Heritage Foundation, John Pearson, Jon Judson, Lynn Sheppard, Paul Willis, Cyril and Darlene Thilges, Gerry Steinauer, David and Ruth Fritchner, the Cowling Arboretum at Carleton College, Jennifer Delisle, Melody Kroll, Rachel Simpson, Kristen Veum, John Peters, the Buena Vista County Conservation Board, the Kossuth County Conservation Board, Todd and Jane Gruis, James Ellis, Jeffrey Walk, Stephen Chaplin, and Alisha Paplow for assistance locating and accessing native prairie remnants. The research was funded by a Geological Society of America Graduate Research grant to E.A.T and NSF grant 1653191 to I.J.L.

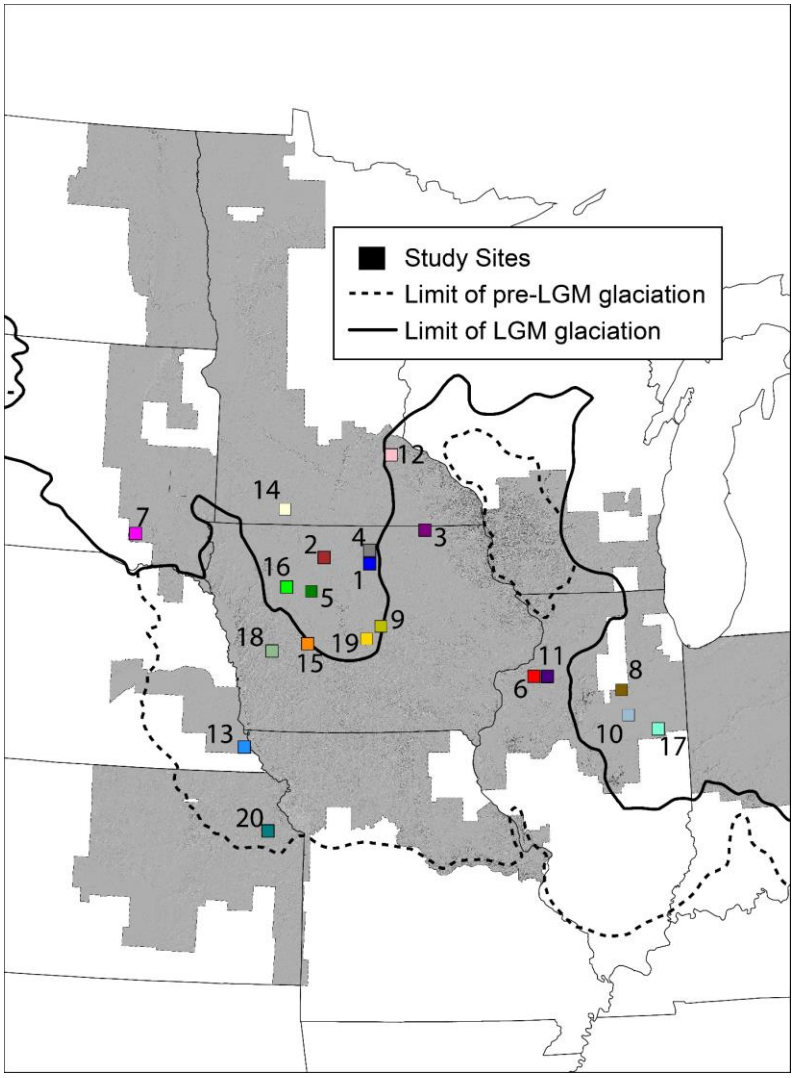

Fig. 5.1. Location of the individual study sites (squares) within the Midwestern U.S. Region-wide soil loss was predicted for areas with LiDAR topographic data, defined by the extent of the gray hillshade map. The dashed and solid lines indicate the extent of the glacial extent prior to the last glacial maximum (LGM) and the extent during the LGM, respectively. The numbers correspond to each field site: 1. Willis, 2. Stinson, 3. Hayden, 4. Hoffman, 5. Kalsow, 6. Munson, 7. Steinauer, 8. Voight Pauper, 9. Kurtz, 10. Weston, 11. Greenlee, 12. McKnight, 13. Fricke, 14. Blue Gentian, 15. Judson, 16. Newell, 17. Loda, 18. Dinesen, 19. Harker, 20. Sheppard.

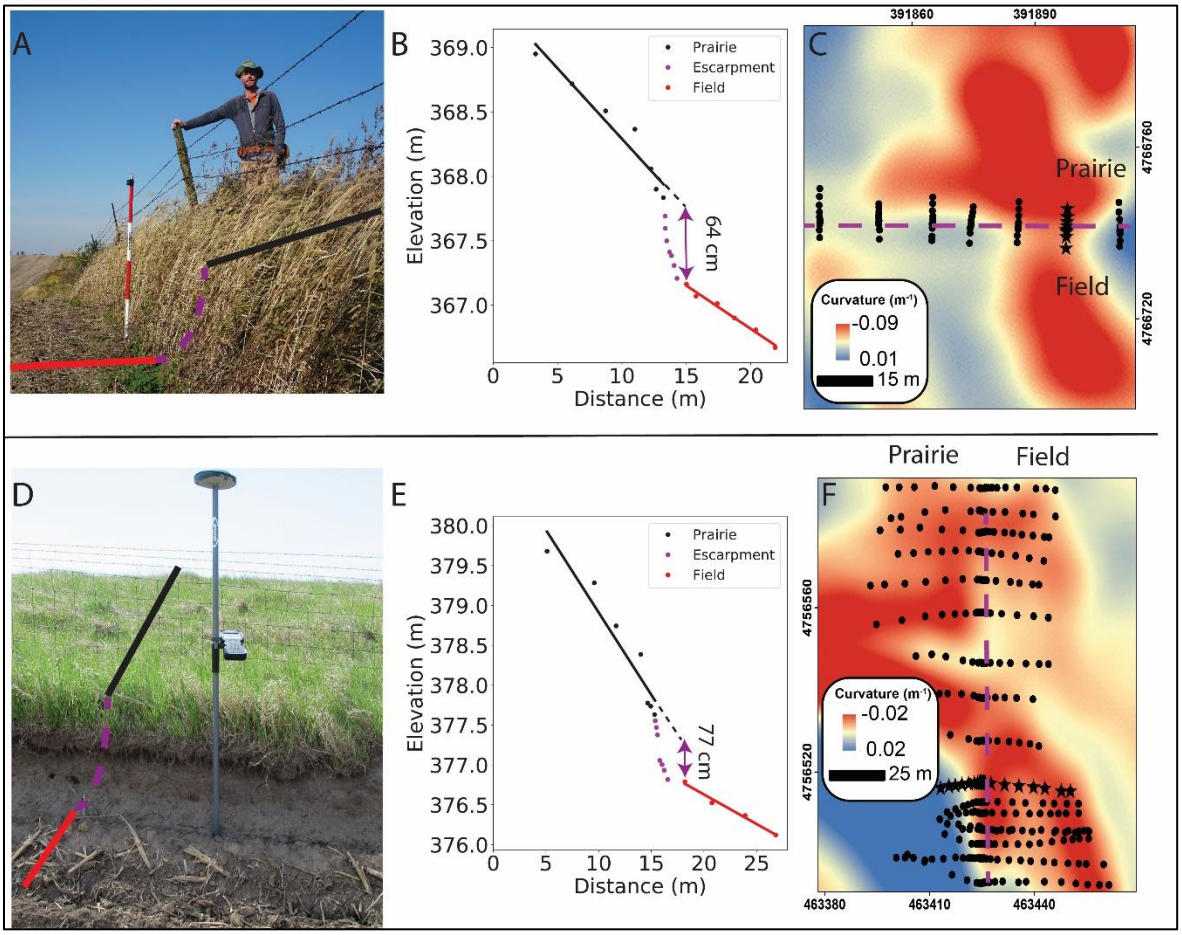

Fig. 5.2. Examples of erosional escarpments and GPS transect analysis. A) Photograph of an escarpment between the native prairie (right) and the adjacent agricultural field (left) at Stinson Prairie. B) An example survey transect and calculated elevation offset. In this example, the offset is 64 cm. C) Map of topographic curvature, where red pixels indicate convex topography, and blue values indicate concave topography. GPS transect lines are shown as black dots, and the black stars indicate the transect shown in A and B. The boundary between the prairie and field is shown as a magenta dashed line. D) Photograph of an escarpment between the native prairie (top) and the adjacent agricultural field (bottom) at Willis Prairie. E) An example profile of a surveyed transect and estimated

elevation offset. In this example, the offset is 77 cm. F) Same as D, but for the Willis site. In B and E the prairie survey points and estimated topographic gradient are shown as the black points and line, respectively; the escarpment is shown as magenta points, and the field points and estimated topographic gradient are shown in red.

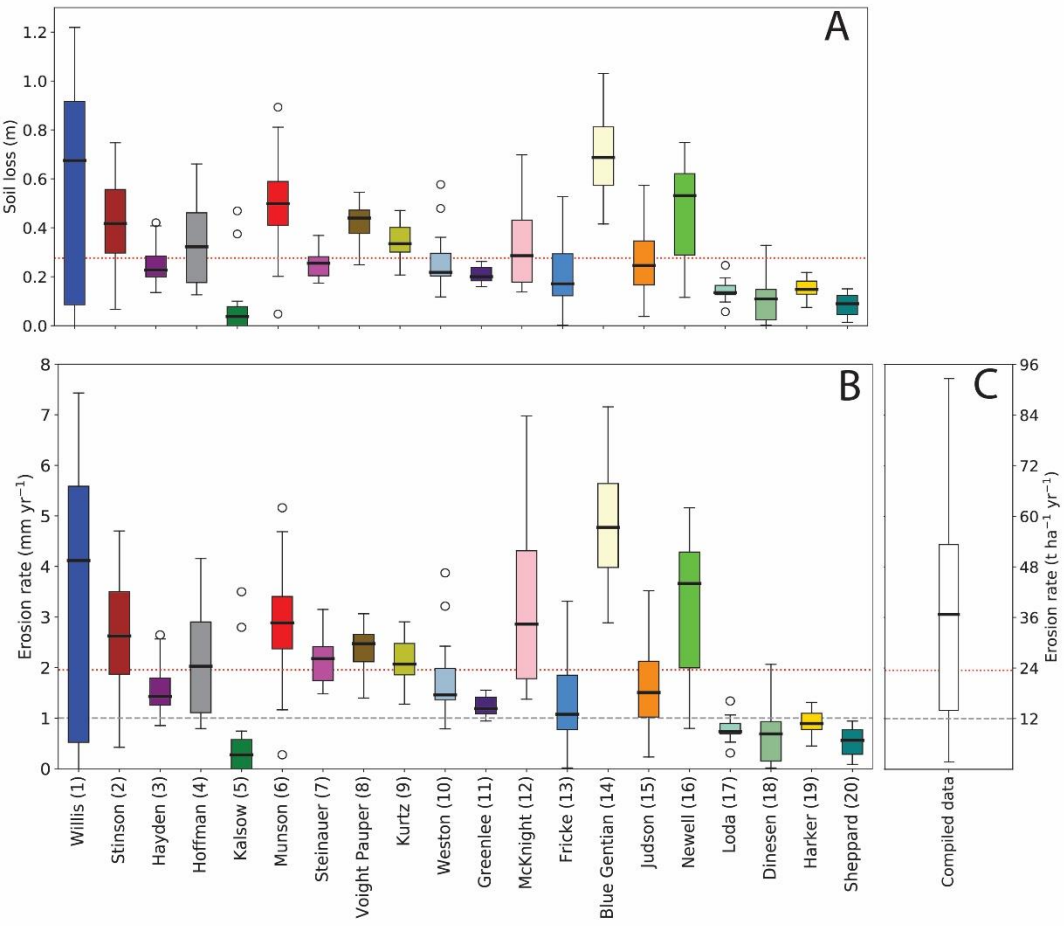

Fig. 5.3. Boxplots of soil loss and erosion rates at each study site. A) Boxplot of soil loss (m) measured for each of transect at each of the 20 sites. The median soil loss for all sites (0.3 m) is shown as the red dotted line. B) Boxplot of erosion rates measured for each site. The USDA soil loss tolerance (T) value is the same for all sites (1 mm yr^{-1}) and is shown as the gray dashed horizontal line. The red dotted line indicates the median value from all sites (1.9 mm yr^{-1}). 15 of the 20 sites have median erosion rates greater than the

T value. Erosion rates were converted to a mass flux (t ha^{-1} yr^{-1}) by assuming a uniform bulk density of 1,200 kg m^{-3}. The numbers for each site correspond to the numbers in Fig. 1. C) Boxplot with compilation of previously published soil erosion rates within the study region. The red dotted line indicates the median value from all the prairie sites. The box spans the interquartile range; the black line is the median, and the bottom and top whiskers represent 5th and 95th percentiles, respectively. Outliers are shown as open circles. Colors of the boxes match those in Figs. 1, 4.

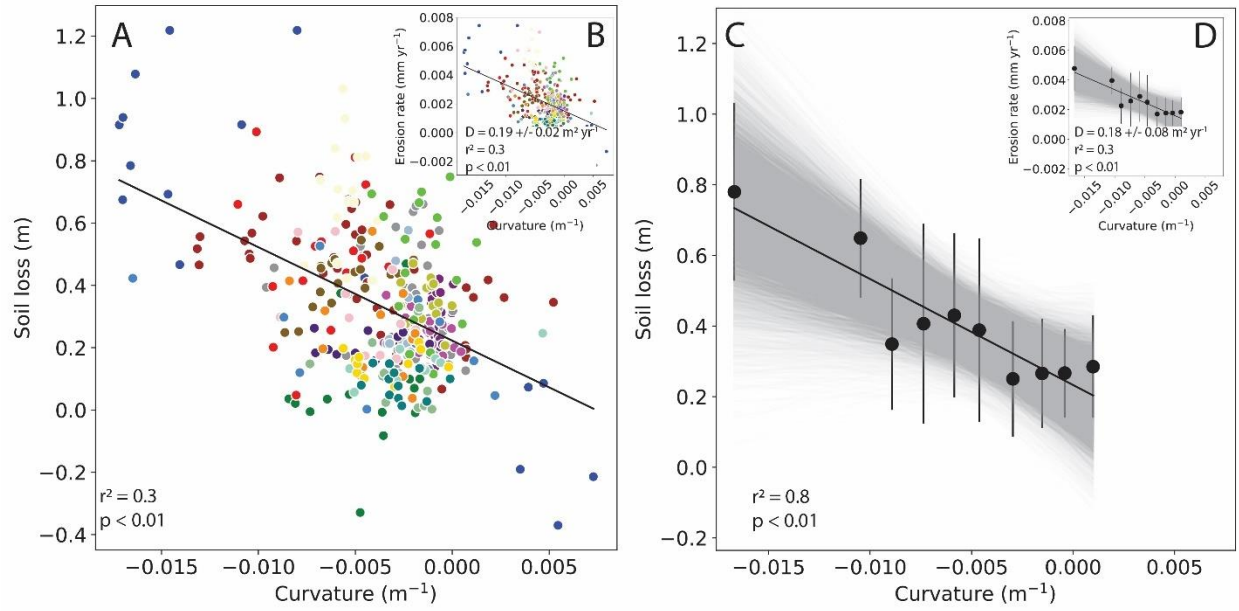

Fig. 5.4. A) Measurements of eroded soil thickness versus topographic curvature for each of the 464 transects at the 20 sites. The points are colored by site location, which matches colors in Figs. 1 and 3. The equation of the regression line for the full dataset is y = (-28.9±3.1)·x+(0.24±0.01). B) Erosion rate versus topographic curvature for each of the transects. The diffusion coefficient (D) calculated from the full dataset is 0.19 ± 0.02 m^2/yr. C) The median ± 1S.D. of the soil thickness values for evenly spaced curvature bins with > four measurements. The gray lines indicate the regression line from each of

10,000 Monte Carlo simulations. The equation of the mean and ± 1S.D. regression line is y = (-30.1±13)·x+(0.23±0.09). D) Points and error bars indicate the median ± 1S.D of the erosion rates for evenly spaced curvature bins with > four measurements. The gray lines indicate the regression line from each of 10,000 Monte Carlo simulations. The mean ± 1S.D D value calculated from the slope of the iterated regressions is 0.18±0.08 m^2 yr^{-1}.

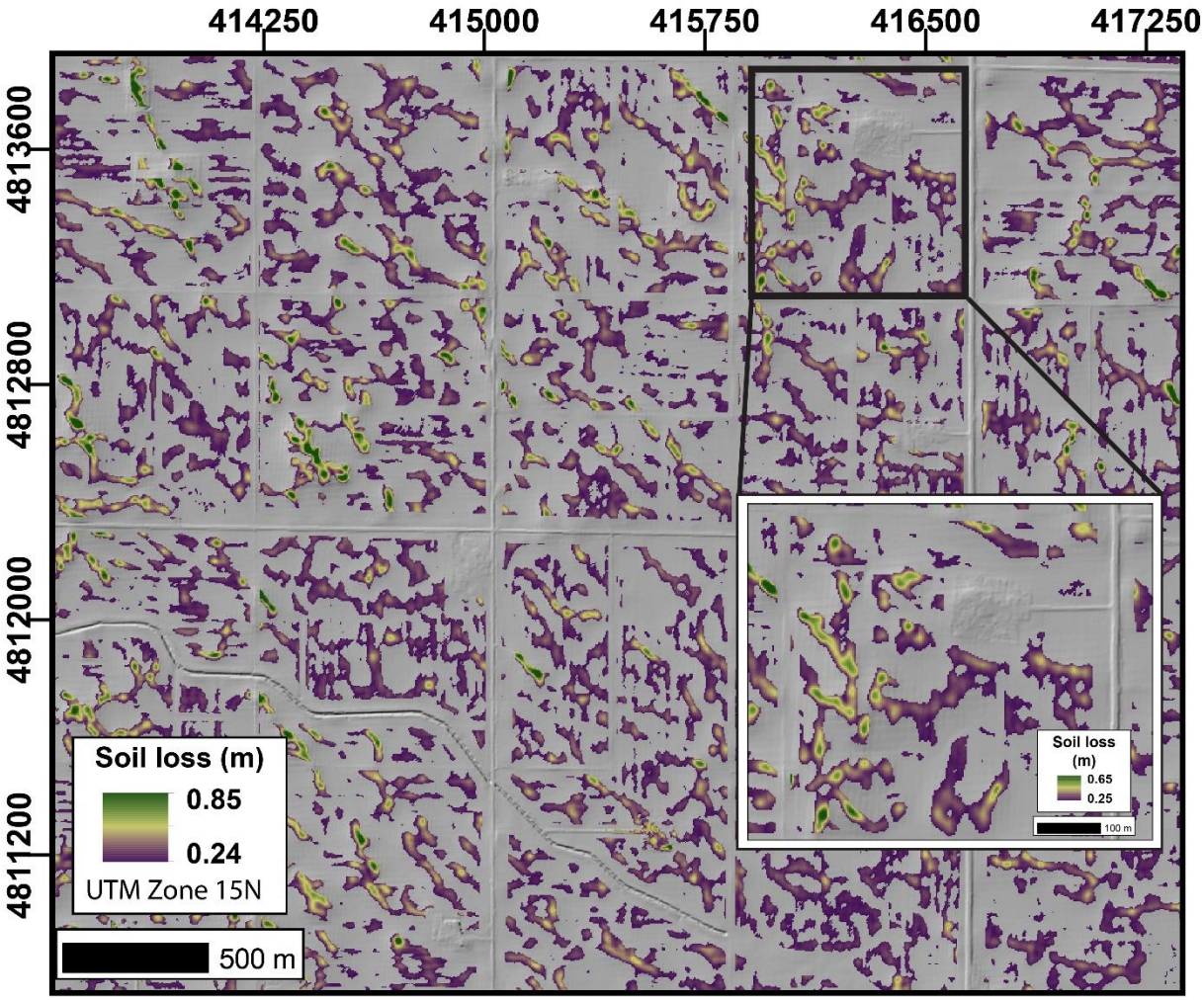

Fig. 5.5. Example of soil loss estimates from 16 km^2 of convex hilltops near Lakota, Iowa. Purple pixels indicate areas with lower soil loss estimates, while areas with higher

soil loss estimates are shown green pixels. The total estimated mass of eroded soil in the full example extent is 99,183 t. The inset demonstrates the removal of buildings, roads, and fence lines from the soil loss raster. Within the inset, we estimate 3,738 t of eroded soil on 0.63 km^2 of convex topography.

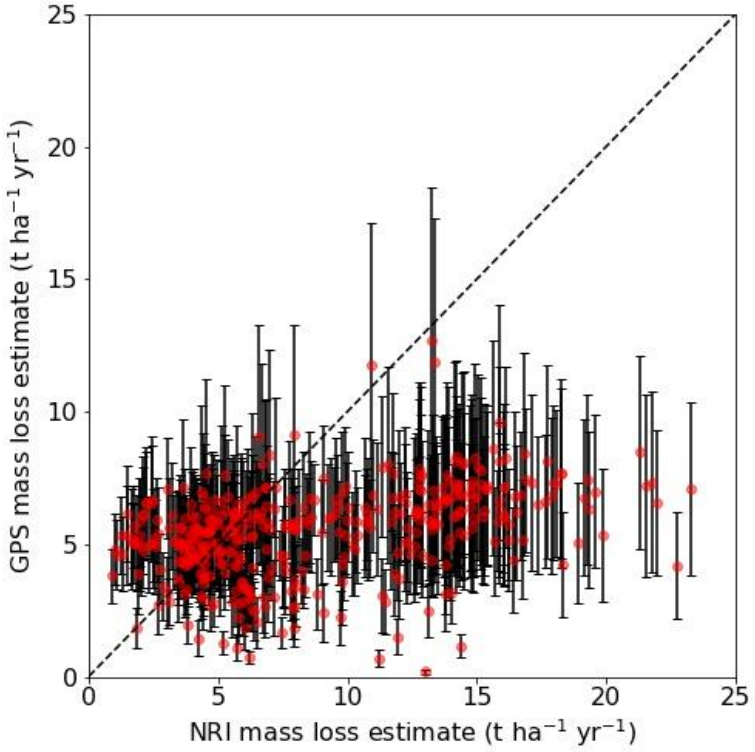

Fig. 5.6. County-level estimates of annual soil flux (t ha^{-1} yr^{-1}) from the USDA National Resources Inventory (NRI) and estimates derived from the relationship between measured soil loss and topographic curvature (Fig. 4). Red circles indicate the mean for each county and the error bars represent the ±1 S.D. uncertainty based on the Monte Carlo simulations.

CHAPTER 6

CONCLUSIONS

Maintaining fertile agricultural soils is essential for producing food for a growing global population. Soil erosion reduces agricultural productivity by degrading soil quality and can lead to negative offsite effects such as impairment of water quality and increased sedimentation within reservoirs. Yet, despite the negative impacts of soil erosion on societal and environmental systems, robust and scalable methods to quantify the magnitude of soil loss at various have not yet been developed. In this dissertation, we fill that research gap by developing a remote sensing method for estimating the magnitude of historical soil loss and a field-based method for quantifying the rates of historical soil loss.

Soil organic carbon is one of the major chemical characteristics that distinguishes A- and B-horizon soils. The differences in soil organic carbon between the horizons leads to visible differences in soil color, especially in mollisols. Hence differences in the concentrations of soil organic carbon, derived from aerial or satellite imagery, can be used to differentiate which soil horizon is exposed at the surface. In Chapter 2, we develop a remote-sensing index using a nationwide dataset of soil organic carbon and hyperspectral measurements, the soil organic carbon index (SOCI), to quantify soil organic carbon concentrations from images of bare soil. The SOCI relies only on the

visible wavelengths, which are frequently measured at high-spatial resolution by aerial- and satellite-based platforms. Results from a test field in Iowa indicate that the SOCI can predict organic carbon with a RMSE of 0.54%.

In Chapter 4, we calculate the SOCI from high-resolution satellite imagery for 210 km^2 of bare soil fields in the midwestern U.S. For each field, we determined the probability of a given SOCI value of a bare soil pixel indicating exposed B-horizon soil. We then related the probability of B-horizon exposure to topography and found that hilltops are often completely denuded of A-horizon soil, a finding which indicates that tillage erosion, which is ignored in U.S. soil erosion assessments, is the primary driver of erosion in the region. Using the relationship between topography and B-horizon exposure, we scaled the estimates of A-horizon soil loss to 3.9 $x10^5$ km^2 of cultivated land across the Midwestern U.S. The results from Chapter 4 provide the first estimates of historical A-horizon loss across the region and indicate that roughly one-third of the region has completely lost A-horizon. A-horizon loss results in decreased crop yields, and our analysis suggests that soil erosion in the region results in a ~6% decrease in yields, causing nearly $3 billion in annual economic losses. Further, we quantify the mass of soil organic carbon lost as A-horizon soil was eroded. We estimate that 1.4±0.5 Pg of carbon has been removed from hillslopes in the region, an amount equivalent to one year of U.S. carbon emissions. The eroded soil carbon is likely deposited in topographic lows within the fields, and restoration of organic carbon on the hillslopes could generate a sink of atmospheric carbon.

Although the remote-sensing methods presented in Chapter 4 provide an estimate of the areal extent of complete A-horizon soil loss, they do not provide information about

the depth of eroded soil or the historical erosion rate. However, in Chapter 5, we use high-resolution topographic surveys conducted across the boundary between 20 perched native prairie remnants and adjacent agricultural fields to quantify the total depth of soil loss since the beginning of agricultural cultivation in the region. Results from the topographic surveys indicate that median soil loss ranges from 0.04–0.69 m, corresponding to erosion rates of 0.2–4.3 mm yr^{-1}. The analysis in this chapter provides the first quantification of regional erosion rates that integrate over the time since cultivation of the region began in the mid-1800's.

Implementation of soil conservation efforts within the midwestern U.S., have been thought to decrease erosion rates over the past several decades. We compare our estimates of the historically averaged erosion rates to the 2017 soil erosion estimates provided by the USDA, which do not include tillage erosion, and find that modern erosion rates outpace historical erosion rates on 60% of agricultural land in the region, indicating that soil conservation efforts have not led to reductions in soil erosion rates throughout the region.

Soil erosion in agricultural landscapes is an underappreciated problem, yet fertile, undegraded soils are key to producing enough food for the growing global population. In this dissertation, we have provided analysis which highlights the enormity of the soil erosion problem within the most agricultural productive region in the U.S. There is urgent need for widespread adoption of soil conservation efforts, including continuous no-till, winter cover crops, crop rotation, and manure addition. If implemented on a regional scale, these conservation farming practices have the potential to rebuild eroded

organic-carbon rich soil, reverse economic losses caused by poor crop productivity, and sequester atmospheric carbon and thereby mitigating climate change.

APPENDIX A

Supplemental material for "A New Index for Remote Sensing of Soil Organic Carbon Based Solely on Visible Wavelengths"

Authors: Evan Thaler[1*], Isaac Larsen[1], Qian Yu[1]

6 pages
2 Tables

Table A1 Combinations of blue (B; 478 nm), green (G; 546 nm), and red (R; 659) reflectance and the associated RMSE values (% SOC) and coefficient of determination values (R^2) from SOC prediction.

Band combination	RMSE	R^2
B	2.81	-0.32
G	2.8	-0.4
R	2.78	-0.46
B/G	2.53	0.36
G/B	2.49	-0.34
B/R	2.6	-0.34
R/B	2.6	0.29
R/G	2.46	-0.25
G/R	2.46	-0.14
(B·G)/R	2.83	0.14
R/(B·G)	10.4	-0.26
(B·R)/G	2.8	0.35
G/(B·R)	3.23	-0.4
(R·G)/B	2.76	0.59
B/(R·G)	1.5	0.35

Table A2 Equations, coefficient of determination (R^2), and RMSE values (% SOC) for SOC prediction using the three spectral indices for the 54 Level III ecoregions.

Ecoregion	n	Median SOC	NDVI			SWIR			SOCI		
			R^2	RMSE	Equation	R^2	RMSE	Equation	R^2	RMSE	Equation
Acadian Plains	19	2.09	0.65	5.43	$1.20e^{(-7*NDVI)}$	0.41	1.30	$0.96*SWIR/NIR^{4.6}$	0.4	1.17	$0.90*SOCI^{1.32}$
Arkansas Valley	81	0.74	0.21	2.47	$0.06e^{(-1*NDVI)}$	0.49	1.08	$0.07*SWIR/NIR^{6.8}$	0.49	1.26	$0.03*SOCI^{3.69}$
Atlantic Coastal Pine	9	0.48	0.32	3.16	$0.83e^{(-5*NDVI)}$	0.38	1.41	$0.46*SWIR/NIR^{5.0}$	0.82	1.68	$0.00*SOCI^{6.13}$
Blue Mountains	5	4.02	0.87	5.17	$0.17e^{(-1*NDVI)}$	0.98	1.01	$0.13*SWIR/NIR^{5.7}$	0.93	1.07	$0.19*SOCI^{1.72}$
Blue Ridge	23	2.42	0.44	6.15	$1.13e^{(-7*NDVI)}$	0.34	1.27	$0.75*SWIR/NIR^{4.0}$	0.62	1.09	$0.95*SOCI^{1.21}$
Boston Mountains	34	1.07	0.34	1.83	$0.58e^{(-5*NDVI)}$	0.34	0.85	$0.79*SWIR/NIR^{1.7}$	0.56	0.99	$0.63*SOCI^{1.07}$
Cascades	6	0.92	0.75	3.37	$0.01e^{(-1*NDVI)}$	0.95	0.89	$1.99*SWIR/NIR^{20.}$	0.88	1.36	$0.01*SOCI^{3.82}$
Central Appalachians	28	1.36	0.42	3.57	$0.24e^{(-1*NDVI)}$	0.4	1.09	$0.15*SWIR/NIR^{7.5}$	0.62	0.99	$0.53*SOCI^{1.74}$
Central California Foothills	61	0.61	0.12	1.24	$0.35e^{(-4*NDVI)}$	0.07	1.38	$0.49*SWIR/NIR^{1.4}$	0.12	1.82	$0.37*SOCI^{0.86}$

Central California Valley	65	0.64	0.4	1.10	$0.02e^{(-1*NDVI)}$	0.21	1.26	$0.22*SWIR/NIR^{3.5}$	0.36	1.77	$0.05*SOCI^{2.53}$
Central Corn Belt Plains	231	0.89	0.25	1.89	$0.37e^{(-5*NDVI)}$	0.51	1.12	$0.35*SWIR/NIR^{2.6}$	0.53	1.52	$0.20*SOCI^{1.40}$
Central Great Plains	158	0.91	0.18	1.51	$0.30e^{(-5*NDVI)}$	0.39	1.18	$0.50*SWIR/NIR^{1.7}$	0.45	1.72	$0.32*SOCI^{0.97}$
Central Irregular Plains	296	1.04	0.27	1.95	$0.08e^{(-1*NDVI)}$	0.5	0.91	$0.50*SWIR/NIR^{2.3}$	0.63	1.27	$0.12*SOCI^{1.99}$
Coast Range	14	2.54	0.48	5.70	$0.72e^{(-9*NDVI)}$	0.61	1.14	$0.20*SWIR/NIR^{8.1}$	0.84	0.84	$0.22*SOCI^{2.68}$
Cross Timbers	49	0.57	0.43	1.30	$0.04e^{(-1*NDVI)}$	0.51	1.24	$0.24*SWIR/NIR^{2.9}$	0.67	1.63	$0.09*SOCI^{2.08}$
Driftless Area	148	1.16	0.27	2.15	$0.38e^{(-6*NDVI)}$	0.52	1.10	$0.42*SWIR/NIR^{2.9}$	0.61	1.37	$0.26*SOCI^{1.47}$
East Central Texas Plains	46	0.34	0.35	0.93	$0.08e^{(-1*NDVI)}$	0.3	1.56	$0.23*SWIR/NIR^{3.1}$	0.46	1.86	$0.11*SOCI^{2.14}$
Eastern Corn Belt Plains	262	0.82	0.24	2.40	$0.26e^{(-1*NDVI)}$	0.13	0.99	$0.44*SWIR/NIR^{3.8}$	0.41	1.18	$0.18*SOCI^{2.23}$
Eastern Great Lakes Lowlands	37	0.81	0.42	9.12	$0.14e^{(-1*NDVI)}$	0.39	1.74	$0.21*SWIR/NIR^{8.2}$	0.62	1.83	$0.25*SOCI^{1.87}$
Edwards Plateau	10	3.14	0.33	2.97	$0.80e^{(-5*NDVI)}$	0.14	0.63	$2.03*SWIR/NIR^{0.7}$	0.63	0.43	$0.74*SOCI^{1}$
Eerie Drift Plain	44	0.32	0.55	5.67	$0.49e^{(-8*NDVI)}$	0.2	1.58	$0.30*SWIR/NIR^{5.3}$	0.68	1.62	$0.22*SOCI^{2.25}$

High Plains	103	0.73	0.03	1.10	$0.58e^{(-2*NDVI)}$	0.09	1.12	$0.46*SWIR/NIR^{1.7}$	0.09	1.72	$0.33*SOCI^{0.88}$
Interior Plateau	143	0.88	0.36	1.69	$0.43e^{(-7*NDVI)}$	0.31	1.12	$0.59*SWIR/NIR^{2.8}$	0.55	1.22	$0.46*SOCI^{1.59}$
Interior River Valleys and Hills	549	0.63	0.26	1.43	$0.23e^{(-7*NDVI)}$	0.31	1.27	$0.47*SWIR/NIR^{2.1}$	0.44	1.56	$0.33*SOCI^{1.25}$
Lake Agassiz Plain	56	0.61	0.32	2.61	$0.34e^{(-6*NDVI)}$	0.52	1.22	$0.46*SWIR/NIR^{2.2}$	0.59	1.66	$0.23*SOCI^{1.31}$
Midatlantic Coastal Plain	76	0.75	0.21	4.88	$0.82e^{(-5*NDVI)}$	0.51	1.72	$0.55*SWIR/NIR^{3.4}$	0.65	1.97	$0.15*SOCI^{2.08}$
Mississippi Alluvial Plain	330	0.68	0.26	2.41	$0.07e^{(-1*NDVI)}$	0.42	1.19	$0.26*SWIR/NIR^{4.7}$	0.46	1.52	$0.13*SOCI^{2.22}$
Mississippi Valley Loess	154	0.39	0.29	1.30	$0.01e^{(-2*NDVI)}$	0.37	1.41	$0.10*SWIR/NIR^{7.8}$	0.51	1.58	$0.12*SOCI^{3.09}$
Nebraska Sand Hills	14	0.28	0.24	0.60	$0.01e^{(-2*NDVI)}$	0.43	1.90	$0.09*SWIR/NIR^{3.5}$	0.61	2.61	$0.00*SOCI^{3.21}$
North Central Hardwood	383	0.74	0.18	3.17	$0.50e^{(-6*NDVI)}$	0.31	1.51	$0.67*SWIR/NIR^{2.1}$	0.44	1.89	$0.33*SOCI^{1.26}$
Northeast Coastal Zone	31	0.78	0.34	1.94	$0.63e^{(-5*NDVI)}$	0.52	1.30	$0.76*SWIR/NIR^{2.6}$	0.26	1.69	$0.37*SOCI^{1.46}$
Northeastern Highlands	56	1.72	0.29	3.26	$1.10e^{(-6*NDVI)}$	0.06	1.18	$1.10*SWIR/NIR^{3.8}$	0.33	1.24	$0.60*SOCI^{1.22}$
Northern Allegheny Plateau	37	0.67	0.34	2.44	$0.32e^{(-1*NDVI)}$	0.07	1.29	$0.08*SWIR/NIR^{12.}$	0.56	1.39	$0.36*SOCI^{1.95}$

Northern Glaciated Plains	205	1.54	0.12	5.02	$0.51e^{(-6*NDVI)}$	0.56	0.88	$0.55*SWIR/NIR^{2.5}$	0.66	1.23	$0.02*SOCI^{2.45}$
Northern Piedmont	21	0.74	0.5	1.60	$0.17e^{(-1*NDVI)}$	0.02	1.54	1.14*SWIR/NIR	0.2	1.71	$0.08*SOCI^{3.55}$
Northern Rockies	140	1.53	0.32	3.25	$0.61e^{(-6*NDVI)}$	0.48	1.02	$0.84*SWIR/NIR^{2.2}$	0.44	1.24	$0.60*SOCI^{1.13}$
Northwestern Glaciated Plains	84	0.93	0.18	1.76	$0.46e^{(-4*NDVI)}$	0.18	0.92	$0.56*SWIR/NIR^{1.8}$	0.19	1.55	$0.37*SOCI^{0.95}$
Northwestern Great Plains	114	1.30	0.46	2.44	$0.22e^{(-1*NDVI)}$	0.38	0.80	$0.22*SWIR/NIR^{5.0}$	0.43	1.11	$0.18*SOCI^{1.89}$
Ouachita Mountains	46	0.65	0.6	1.91	$0.31e^{(-1*NDVI)}$	0.52	1.23	$0.28*SWIR/NIR^{5.7}$	0.81	1.19	$0.30*SOCI^{2.33}$
Ozarks Highlands	146	1.06	0.31	2.26	$0.67e^{(-5*NDVI)}$	0.44	0.93	$0.45*SWIR/NIR^{4.0}$	0.6	0.98	$0.57*SOCI^{1.26}$
Piedmont	98	0.68	0.21	2.46	$0.36e^{(-1*NDVI)}$	0.12	1.40	$0.29*SWIR/NIR^{5.5}$	0.52	1.42	$0.31*SOCI^{2.15}$
Ridge and Valley	88	1.58	0.36	5.51	$0.77e^{(-9*NDVI)}$	0.34	1.24	$0.87*SWIR/NIR^{4.9}$	0.54	1.16	$0.30*SOCI^{2.24}$
Sierra Nevada	18	1.69	0.56	4.24	$0.39e^{(-8*NDVI)}$	0.46	0.86	$1.30*SWIR/NIR^{2.2}$	0.6	0.85	$0.16*SOCI^{2.12}$
Sonoran Basin and Range	31	0.41	0.58	0.70	$0.07e^{(-1*NDVI)}$	0.17	1.90	$0.23*SWIR/NIR^{3.0}$	0.12	2.42	$0.03*SOCI^{2.86}$
South Central Plains	368	0.46	0.43	1.21	$0.13e^{(-1*NDVI)}$	0.22	1.42	$0.40*SWIR/NIR^{2.6}$	0.52	1.62	$0.23*SOCI^{1.79}$

Southeastern Plains	176	0.42	0.13	4.20	$0.04e^{(-1*NDVI)}$	0.42	1.65	$0.25*SWIR/NIR^{4.9}$	0.55	1.81	$0.31*SOCI^{1.85}$
Southeastern Wisconsin Till Plains	71	1.49	0.15	3.67	$1.05e^{(-4*NDVI)}$	0.42	1.02	$0.84*SWIR/NIR^{2.4}$	0.58	1.18	$0.21*SOCI^{1.76}$
Southern Coastal Plains	116	0.61	0.06	6.99	$0.54e^{(-5*NDVI)}$	0.3	1.62	$0.37*SWIR/NIR^{3.1}$	0.54	2.10	$0.09*SOCI^{1.94}$
Southwest Tablelands	46	0.73	0.22	1.88	$0.30e^{(-5*NDVI)}$	0.28	0.98	$0.42*SWIR/NIR^{2.0}$	0.26	1.01	$0.30*SOCI^{0.98}$
Southwestern Appalachians	32	1.01	0.42	0.89	$0.18e^{(-1*NDVI)}$	0.42	1.14	$0.15*SWIR/NIR^{8.7}$	0.63	1.67	$0.32*SOCI^{2.18}$
Texas Blackland Prairies	10	1.60	0.45	1.95	$0.44e^{(-7*NDVI)}$	0.45	0.43	$0.65*SWIR/NIR^{2.9}$	0.44	0.46	$0.88*SOCI^{0.87}$
Western Allegheny Plateau	78	1.17	0.4	2.23	$0.41e^{(-1*NDVI)}$	0.17	1.21	$0.56*SWIR/NIR^{4.7}$	0.68	1.18	$0.39*SOCI^{2.14}$
Western Corn Belt Plains	595	1.49	0.15	2.70	$0.60e^{(-4*NDVI)}$	0.46	0.97	$0.67*SWIR/NIR^{1.7}$	0.54	1.41	$0.21*SOCI^{1.38}$

APPENDIX B

Supplementary Information for

The extent of soil loss across the U.S. Corn Belt

Authors: Evan A. Thaler, Isaac J. Larsen, Qian Yu

Correspondence to: ethaler@geo.umass.edu

This PDF file includes:

Materials and Methods

Initial condition of the soil organic carbon index

Our interpretation that the exposure of soils with low soil organic carbon (SOC) concentrations on convex hilltops indicates a SOC-rich A-horizon was eroded relies on the assumption that hilltops in the Corn Belt maintained a layer of SOC-rich soil prior to cultivation. Native prairie remnants record the pre-disturbance soil catena (Manies et al., 2001), but the permanent vegetation cover in the prairie precludes application of the satellite-derived soil organic carbon index (SOCI) (Thaler, Evan A. et al., 2019) to assess the distribution of SOCI throughout the prairies. Hence, we collected soil cores from hilltops in a native prairie in Iowa to directly measure the SOCI for the prairie soils and then compared the SOCI values to soil samples collected from the surface of hilltops in an adjacent agricultural field (Fig. S1). Each soil sample was dried, sieved to < 2 mm, and the spectral reflectance was measured using an ASD FieldSpec 4 with a Muglight attachment. SOCI for the samples was calculated from the spectral reflectance data following (Thaler et al., 2019).

The three cores collected on convex topography (Fig. S1a-b) in the prairie display high SOCI values at the surface that decline with depth (Fig. S1c-e), consistent with previous measurements of SOC-depth profiles (Mishra et al., 2009). The mean SOCI value for the uppermost 1 cm in the prairie samples is 6.5, and the high SOCI values in near-surface soils is consistent with our assumption that hilltops in native prairies had SOC-rich A-horizon soils prior to cultivation. On the three sampled hilltops in the adjacent agricultural field (Fig. S1f), the mean SOCI value of the ten surface samples is 2.4, which corresponds to SOCI values for the 30-40 cm depth interval of the prairie soils, suggesting an equivalent thickness of soil has been lost from the hilltops.

Topographic analysis

LiDAR topographic data were downloaded from the USGS (Dollison, 2010) and from individual state data repositories. To determine the appropriate resolution for measuring topographic curvature (∇^2), we calculated curvature from test digital elevation models (DEM) with resolutions that varied from 2 to 15 m in 1 m increments. For each grid size, curvature values were extracted from a polygon containing a hilltop, hillslope, and hollow, and the interquartile range (IQR) (25^{th} to 75^{th} percentiles) was calculated (Fig. S3). We find that the IQR of curvature decreases with increasing grid size, indicating greater terrain roughness at lower grid sizes. At the 4 m grid size, there is a break in the scaling, such that the IQR of curvature shows relatively little variation with increasing grid size. Following prior work (Roering et al., 2010), we interpret the scaling break to differentiate between landscape-scale hilltop-hollow topography and smaller-scale topographic roughness generated, by, for example, plowing. Hence we resampled the LiDAR-derived DEMs to a 4 m spatial resolution to capture the landscape-scale hilltop and hollow topography in our analyses. Slope and topographic curvature values were calculated as the first and second derivative of elevation, respectively.

Cumulative distributions of topographic curvature were extracted from all of the analyzed fields within each of the 28 individual study sites (Fig. S15) and for the region-wide dataset by first binning the curvature data into 50 bins of uniform width. The median slope values shown in Fig. 3 were calculated for all the pixels located within each curvature bin.

Image processing

High-resolution satellite images (WorldView-2, WoldView-3, Quickbird-2, and GeoEye-1) provided by the Commercial Archive Data for NASA Investigators (Neigh et al., 2013) or the Polar Geospatial Center were orthorectified using the rational polynomial coefficient orthorectification workflow in ENVI 5.4. The images were radiometrically corrected using an empirical line correction method (Smith and Milton, 1999). A clear water pixel and an aluminum metal roof pixel were identified and calibrated against the known reflectance of distilled water and aluminum metal roofing using data from the ASTER spectral library (Baldridge et al., 2009). The SOCI was calculated for each image and the resulting rasters were resampled to a spatial resolution of 4 m to match the resolution of the curvature grids.

Relating laboratory- and satellite-derived SOCI

The Rapid Carbon Assessment (RaCA), undertaken by the Soil Science Division of the USDA National Resource Conservation Service, collected 144,833 soil samples to 1 m depth at 6,148 sites in the conterminous United States (Wills, Skye et al., 2014). The soil horizon each sample was collected from was determined in the field, and the samples were air-dried and hyperspectral reflectance was measured from 350-2500 nm using a laboratory spectroradiometer and SOC was measured on the dry samples (Sequeira et al., 2014; Wijewardane et al., 2016). We scaled the RaCA-derived SOCI values to the same range as the satellite-derived SOCI values, which are offset from one another due to different measurement conditions, such as atmospheric effects. The re-scaling used the relationship in Figure 5 of Thaler et al. (Thaler et al., 2019), and the methods described therein.

Antecedent precipitation and surface soil moisture

Previous work has demonstrated that the soil surface dries rapidly following precipitation and becomes decoupled from soil moisture at depth (Capehart and Carlson, 1997). Hence we evaluated the timing and magnitude of precipitation prior to image acquisition for each of the 28 sites to qualitatively assess whether the soil surface, which is imaged by the satellites, was likely to have been dry at the time of image acquisition. For each site, precipitation data were downloaded from the nearest weather station that is part of the Hourly Precipitation Dataset, archived at the National Climatic Data Center. At the 28 sites, the minimum time between image acquisition and previous rainfall was 20 hours, with a mean of 73 hours, and the mean amount of precipitation was 10 mm (Fig. S9). Previous observations have indicated that the soil surface becomes completely dry after three to four days (Capehart and Carlson, 1997), and our own observations throughout the study area suggest a faster drying rate, as even following nightly rainfall, the soil surface is typically dry after a full day of summer sunlight. These results suggest the soil surface would have been dry when the cloud-free images were acquired. The predicted B-horizon exposure at sites where rainfall occurred < 72 hours and >72 hours before image acquisition are 31±7% and 30±7%, respectively. Hence the predicted B-horizon exposure is indistinguishable for sites with different rainfall timing which is consistent with a lack of a soil moisture influence on our results.

Effect of moisture on the SOCI

Increases in SOC and soil moisture result in decreased reflectance in the visible spectrum and cause soils to appear darker (Nocita et al., 2013). We assessed the effect of

soil moisture on the SOCI for soils with a range of SOC by measuring soil spectral reflectance under dry and saturated moisture levels. The spectra used to calculate the soil organic carbon index values were measured using an ASD FieldSpec 4 with a Muglight attachment. Soil organic carbon was measured using a Costech elemental analyzer (ECS 4010) following removal of inorganic carbon with 1 N HCl. We found that the magnitude of the increase in the SOCI as a function of soil moisture is related to the SOC concentration of the sample. For samples with the largest concentration of SOC (~4%), there is a factor of four increase in the SOCI, whereas the SOCI increases by a maximum of a factor of three for samples with < 1% SOC (Fig. S10).

The spectral measurements of RaCA soil samples used to develop the logistic regression analysis that informed our classification of A- and B-horizon soils in the satellite images were made on dried soils. We assessed the impact of soil moisture on the classification of soil horizons by adjusting the SOCI values for the RaCA samples according to our experimental results. For A-horizon samples, which have a range of SOC from ~1.0% to 9.0%, the SOCI values were conservatively increased by a minimum factor of three and a maximum factor of four. Similarly, B-horizon samples, which have a range of SOC from ~0.5% to 2.5%, the SOCI values were increased by a minimum factor of two and a maximum factor of three. In our framework, samples with SOCI values less than the value represented by the 50% probability threshold are classified as B-horizon. For each set of RaCA calibration samples for the 28 study sites, we recalculated the classification threshold for five soil moisture cases: 1) the minimum effect of soil moisture on the A-horizon SOCI values and dry B-horizon values, 2) the minimum effect of soil moisture on both the A- and B-horizon SOCI values, 3) the maximum effect of

soil moisture on the A-horizon and dry B-horizon SOCI values, 4) the maximum effect of soil moisture on the A-horizon and the minimum effect on the B-horizon SOCI values, and 5) the maximum effect of soil moisture on both the A- and B-horizon SOCI values. We simulated a variety of scenarios because topographic influences on soil moisture may result in different moisture levels throughout a landscape. The thresholds were applied to images for each to the 28 study sites and the fraction of the land area with exposed B-horizon soil was calculated (Fig. S12). Increasing soil moisture increases the A- and B-horizon SOCI values and hence increases the threshold SOCI value, such that samples classified as A-horizon when dry are classified as B-horizon when wet (Fig. S11). When the moisture-adjusted thresholds are applied to the images, the fraction of pixels classified as B-horizon increases relative to the threshold developed using the SOCI values from dried soil samples. Because the SOCI values in the image are lower than the predicted values for moisture-adjusted sample values, the thresholds calculated using samples adjusted for soil moisture reclassify A-horizon pixels as B-horizon. Hence, our estimate of topsoil loss based on the threshold developed using the dry RaCA samples is a minimum if any moisture is present in the analyzed fields.

Relationship between SOC and the SOCI

The relationship between SOC and the satellite-derived SOCI was validated at five agricultural fields across the U.S. (Fig. S13). Two of the sites are in areas with till-derived soils (Fig S14a, d), and the two other sites are in areas with loess-derived soils (Fig.14b, c) within the Corn Belt region (Li et al., 2018; Wills, Skye A. et al., 2007; Wilson et al., 2018). At the four sites, the coefficient of determination (R^2) ranges from

0.63 to 0.68. The relationship was also validated at a fifth site ($R^2 = 0.72$), located in Maryland (Fig. S14e) (Hively et al., 2011), which demonstrates the validity of the index beyond the Corn Belt region. Additionally, the correlation between the SOCI and the SOC was assessed for each set of RaCA soil samples within a 50 km buffer of each of the 28 field sites. The mean R^2 value of the correlations is 0.8 (Fig. S6), indicating that the SOCI predicts SOC very well within the study area.

Relationship between SOCI and topography

The relationship between SOC, SOCI, and topographic curvature was examined at the four SOCI validation sites in the Corn Belt (Fig. S14). Consistent with observations and interpretations at the 28 sites (Fig. 3), low SOC and SOCI values are observed on the most convex topography (negative curvature), and the SOC and SOCI values increase as curvature increases. At the two sites in the till-derived soils (Fig. S14b, c), where the sampling point density is higher than the other two sites, the full range of values is observed at the transition from concave to convex topography, an observation consistent with both B-horizon exposure via water erosion and deposition of A-horizon from tillage translocation at those locations (Li et al., 2018) .

Determination of soil parent material

To determine the spatial distribution of till-and loess-derived soils, we used the United States Geological Survey map of surficial deposits and the inferred ice limit of the last glacial maximum (LGM) compiled from 31 individual quadrangles mapped at a

1:1,000,000 scale (Fullerton et al., 2004). We presume that areas north of the LGM are composed of soils derived from glacial till surficial deposits, whereas soils south of the LGM are developed primarily from loess. Loess deposits have been mapped in the Driftless Area, a region that was not glaciated during the LGM (Leigh and Knox, 1994). Hence, we classify soil in the Driftless Area as loess-derived.

Calculation of economic losses

We calculated economic losses based on data for corn and soybean production, as, on average, these two crops make up 95% (United States Department of Agriculture, National Agricultural Statistics Service, 2017) of the area planted in each county within the study area. We used results from a comprehensive study of the influence of erosion on corn yields in Iowa to assess declines in productivity. Prior work has shown that in mollisols, complete topsoil loss produces similar decreases in crop yields for corn and soybeans (Fullerton et al., 2004), hence we assume the fractional yield losses for soybeans are the same as for corn. We calculate economic losses based on our estimates of the area with exposed B-horizon soil, and the mean corn and soybean prices, hectares planted, and yields (Fig. S16) from 2012-2018 using data from the U.S Department of Agriculture National Agricultural Statistics Service. Corn yields were previously evaluated at 569 sites in 44 counties in Iowa, where categorical measurements of soil erosion were also evaluated (Fenton, 2012). The sites include areas where soil parent materials are glacial till and loess. The erosional severity of soils was classified by the amount of A-horizon remaining, as no erosion to slight severity (>18 cm remaining), moderate severity (8-18 cm remaining), and severe (< 8 cm remaining). In soils

developed from glacial till, corn yields decreased 55,800 kg km^{-2} as soils became moderately eroded and further decreased 81,500 kg km^{-2} when soils became severely eroded. Similarly, corn yields in loess-derived soils decreased by 36,400 kg km^{-2} for moderately eroded soils and further decreased by 30,700 kg km^{-2} when soils were severely eroded (Fenton, 2012). Because topsoil has been completely eroded at the sites for which we calculate economic losses, and thus would be classified as severely eroded, we sum the decreased corn yields from slight to severe, giving estimated reduction of 137,300 kg km^{-2} for soils formed from glacial till and 67,100 kg km^{-2} for loess-derived soils.

Based on the hectares planted of corn (Fig. S16a) and soybeans (Fig. S16d), predicted areas of topsoil loss (mean loss ± 1 S.D.), reductions in corn (Fig. S16b) and soybean (Fig. S16e) yields due to complete topsoil loss, and the average corn and soybean prices from 2012-2018 (US$0.15 kg^{-1} and $0.37 kg^{-1}, respectively) (USDA Economic Research Service, 2017), we estimate the mean annual economic losses per county for decreased corn (Fig. S16c) and soybeans (Fig. S16f). Annual economic losses were calculated as: Annual losses per county [USD $county^{-1}$] = Exposed B-horizon area [ha $county^{-1}$] * mean yield [kg ha^{-1}] * fraction decrease due to A-horizon erosion * crop price [USD kg^{-1}], where USD is U.S. dollars. We further estimated economic losses at the farm-level (Fig. 4d) by dividing the county-level losses by the number of farms in each county (Fig. S16g) (U.S. Department of Agriculture, 2018).

Data availability

Data are cataloged at the Oak Ridge National Laboratory Distributed Active Archive Center (https://doi.org/10.3334/ORNLDAAC/1774) (Thaler, EA., IJ. Larsen, Q. Yu., 2020). The archive includes spatial raster data for topographic metrics (elevation, slope, curvature), soil organic carbon index values, and the probability of B-horizon soil. Spatial vector data and tabular data with county-, state-, and farm-level erosion and economic loss values are also archived. The soil organic carbon index values, derived from the RaCA samples, and used to develop the logistic regression and receiver operator characteristic curve for each site (such as those shown in Fig. S8) are also archived.

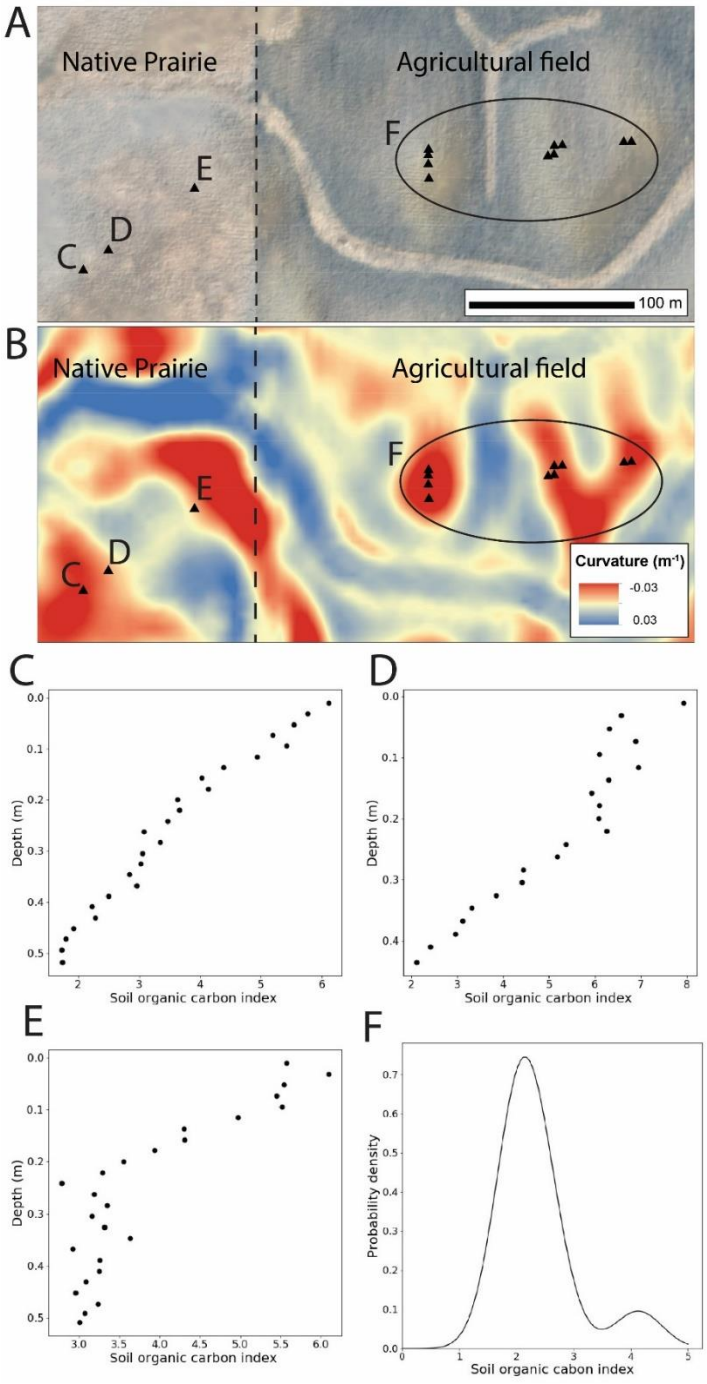

Fig. S1. The Soil Organic Carbon Index (SOCI) values measured for three soil cores from a native prairie in Iowa and surface soil samples from an adjacent agricultural field. A) True-color WorldView-2 image showing location of prairie cores (C, D, E) and surface samples from the field (F) B). Map of topographic curvature where red pixels denote negative curvature (convex topography) and blue pixels denote positive curvature (concave topography). The SOCI-depth profiles from the prairie cores are shown in panels C-E. F) The distribution of SOCI values for surface soil samples collected in the

adjacent agricultural field. Locations of the samples are shown in panels A and B. Image credit: ©2015 DigitalGlobe, Inc., a Maxar company, NextView License.

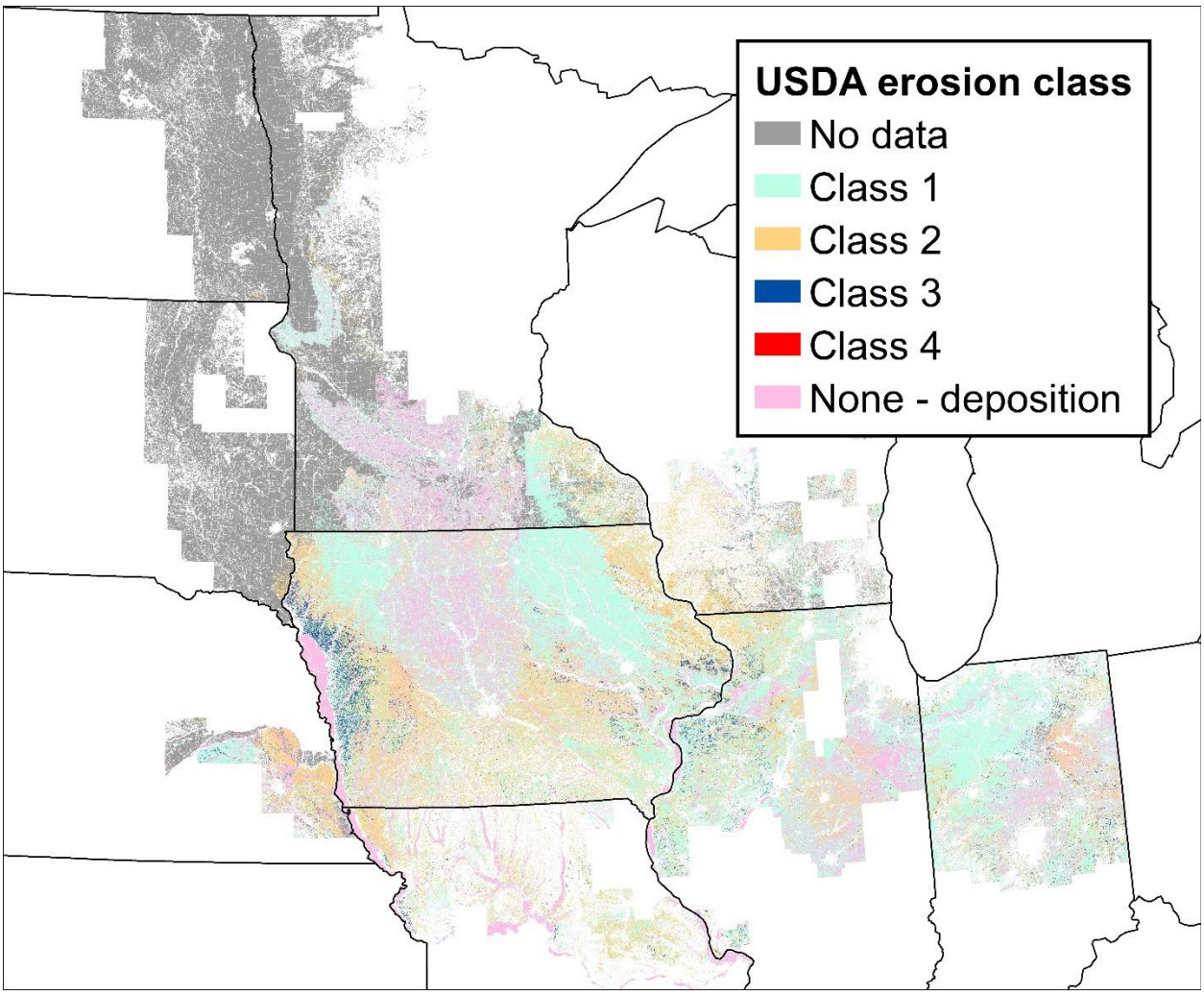

Fig. S2. Map of erosion classes assigned by the U.S. Department of Agriculture (25). 31% of the soils in the area have soils with Class 1 erosion, 16% have Class 2 erosion, 3 % have Class 3 erosion, 0% have Class 4 erosion, 15% of soils are classified as having no erosion or as depositional sites, and classification data are not available for 35% of soils. Class 4 is equivalent to the complete loss of A-horizon measured by our analysis.

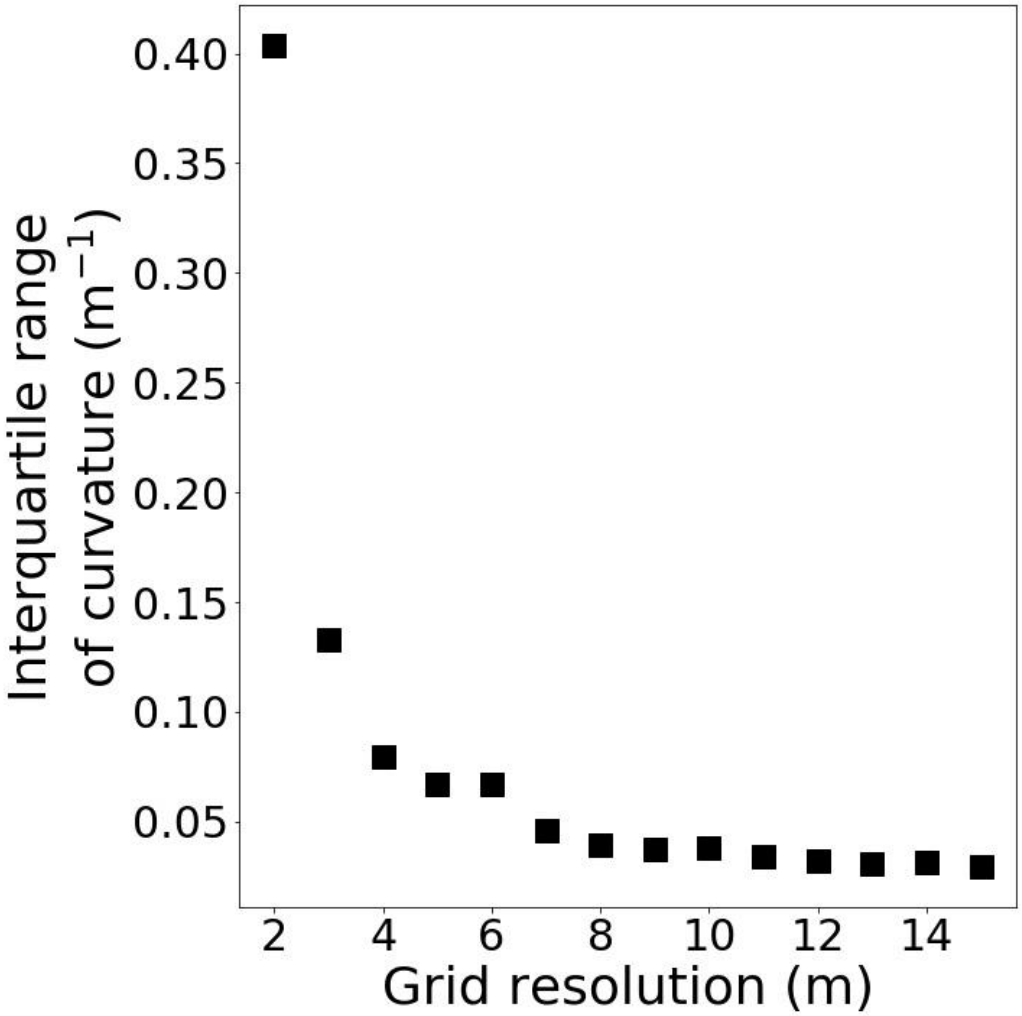

Fig. S3. The interquartile range of curvature values calculated using grid resolutions ranging from 2 m to 15 m.

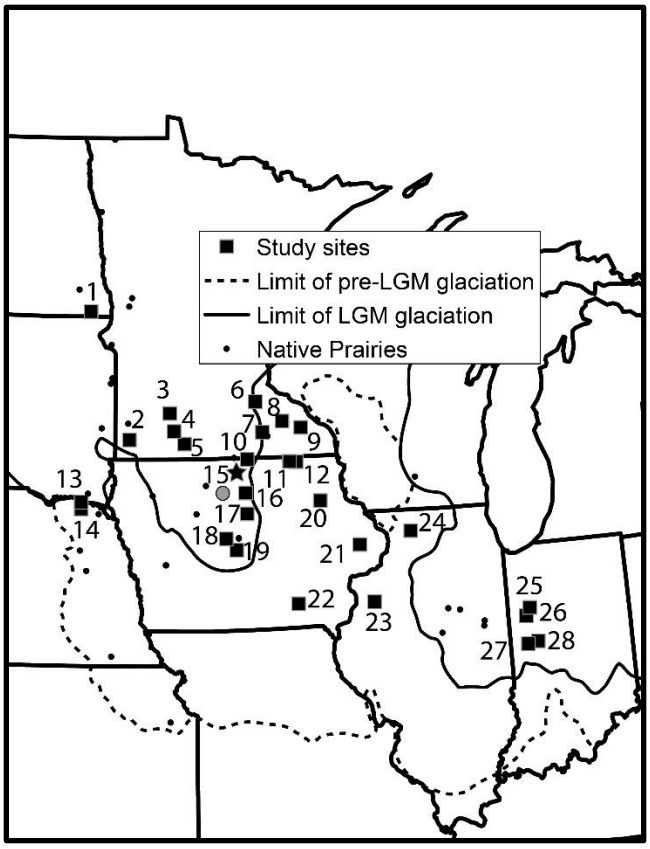

Fig. S4 Location of study sites with numbers corresponding to study sites in Fig. S17 and in the ORNL DAAC data repository. The gray circle shows the location of the native prairie and adjacent agricultural field shown in Fig. S1, and the star indicates the location of the example field shown in Fig. 2. The dots indicate the location of soil samples collected on convex topography in native prairies (26) that were used to estimate the organic carbon stock to 30 cm-depth.

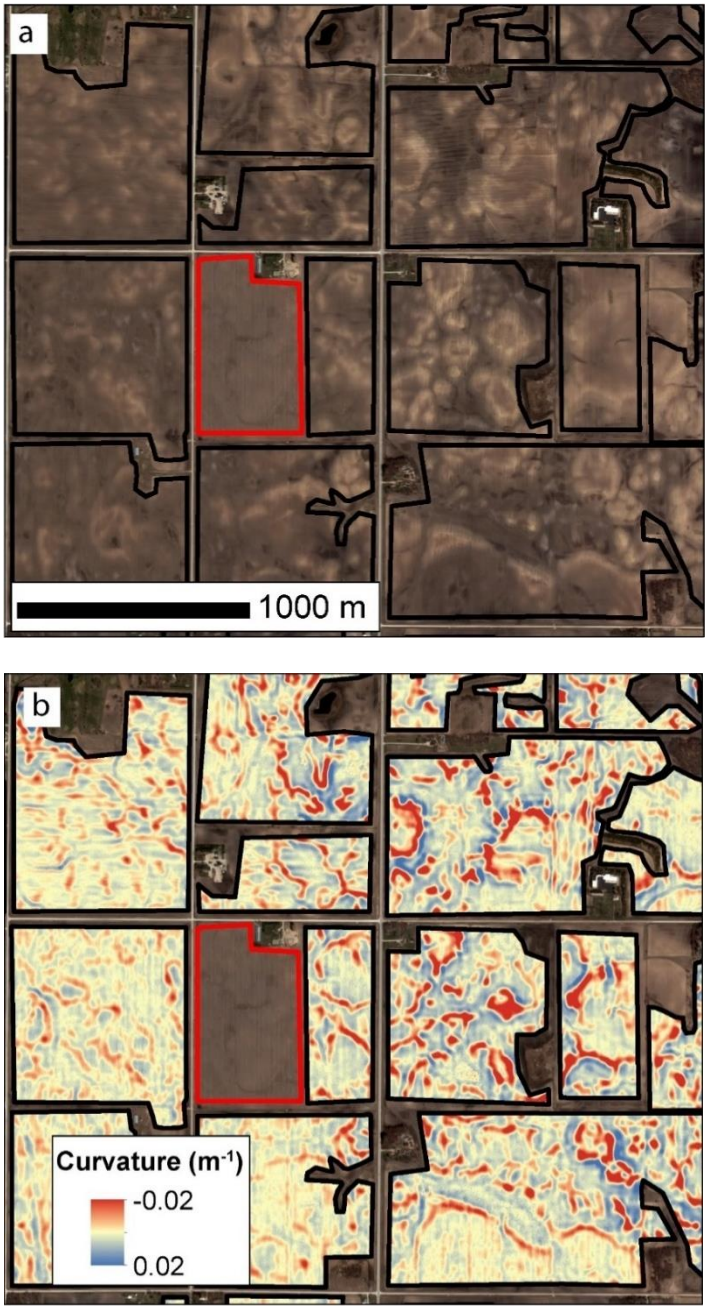

Fig. S5. An example study site comprised of multiple fields shown in (a) true color and (b) topographic curvature The black polygons surround plowed fields with bare soil. The field within the red polygon contains crop residue and such fields are excluded from the analysis, as are areas such as fence lines and grass waterways where bare soil is not exposed. Image credit: ©2015 DigitalGlobe, Inc., a Maxar company, NextView License.

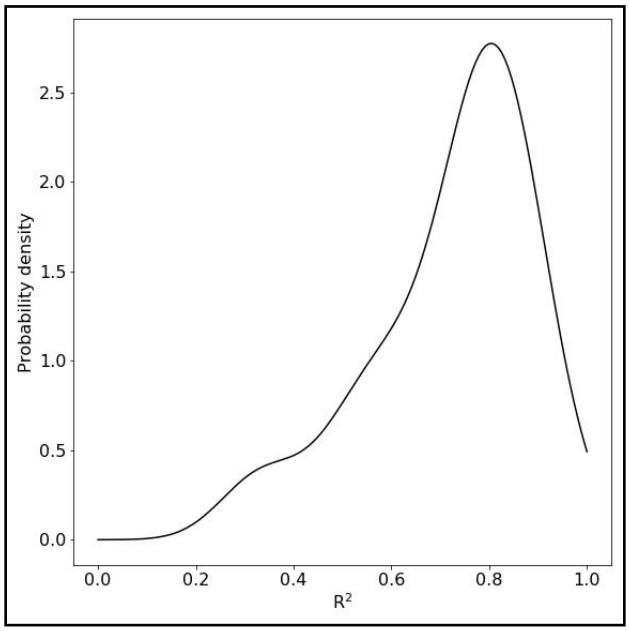

Fig. S6. Probability density of R^2 values for the relationship between the soil organic carbon index (SOCI) and soil organic carbon (SOC) for the data used to develop the logistic regression models at each of the 28 study sites.

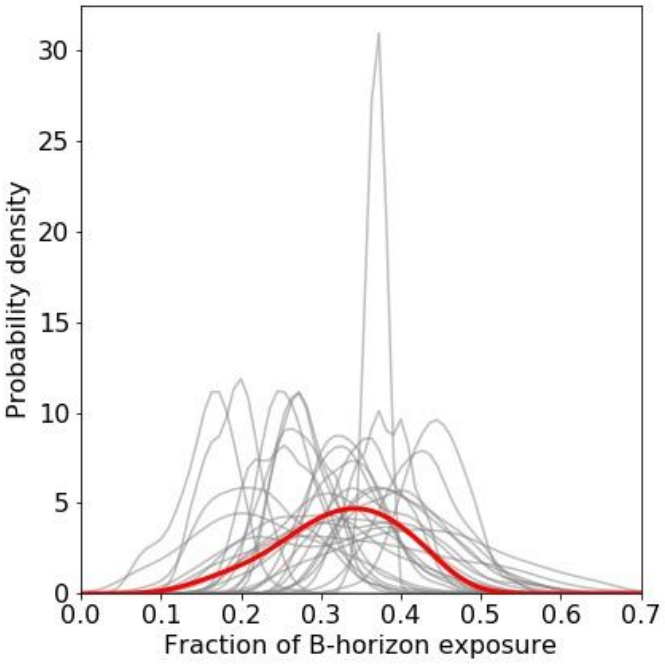

Fig. S7. Probability density of B-horizon exposure for each of the 28-sites (gray lines) generated from 500 iterations of a bootstrapped logistic regression. The red line shows the mean probability density of B-horizon exposure for all sites.

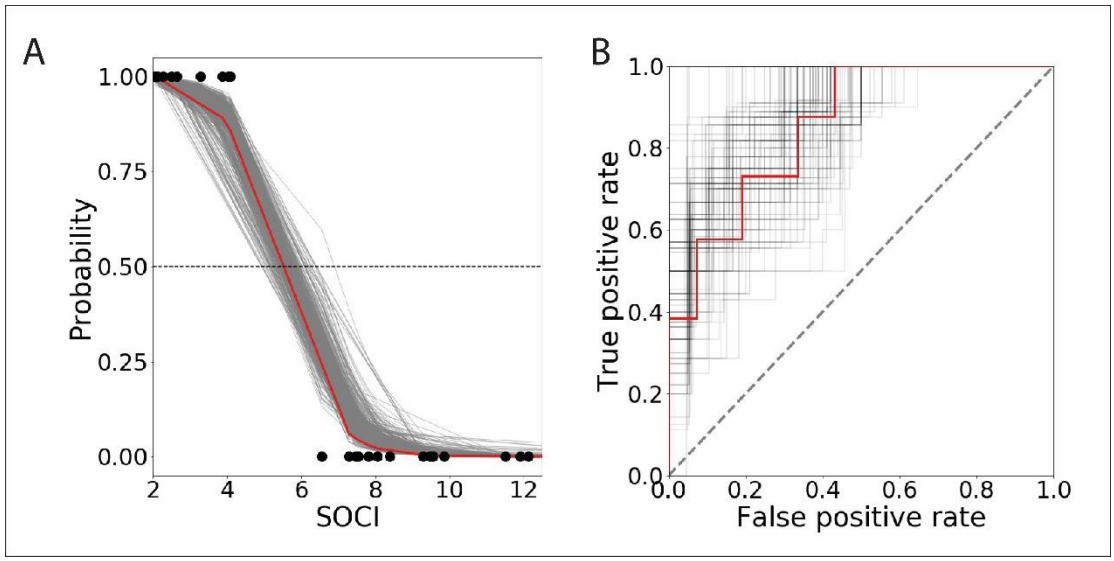

Fig. S8. Example of the logistic regression employed to classify soil horizons for the example field in Fig. 2. a) Logistic regression used for classification of A- and B-horizon soil organic carbon index (SOCI) values. The SOCI values for the A-horizon samples are shown at zero on the y-axis and B-horizon values are shown at 1.0. The solid red line describes the mean probability of an SOCI value belonging to the B-horizon class, and the results from each of the 500 bootstrapped iterations of the logistic regression are shown in gray. The threshold SOCI we use to differentiate A- and B-horizon soils is the 50% probability of an SOCI value representing a B-horizon pixel. In this example, the threshold SOCI is 8.0±1.2. b) The receiver operator characteristic curve for each iteration (gray lines) and the mean of all iterations (red line), which demonstrates the true- versus false positive classification rate. The mean area under the curve (AUC), which quantifies the rate of true classification, is 0.75 ±0.06.

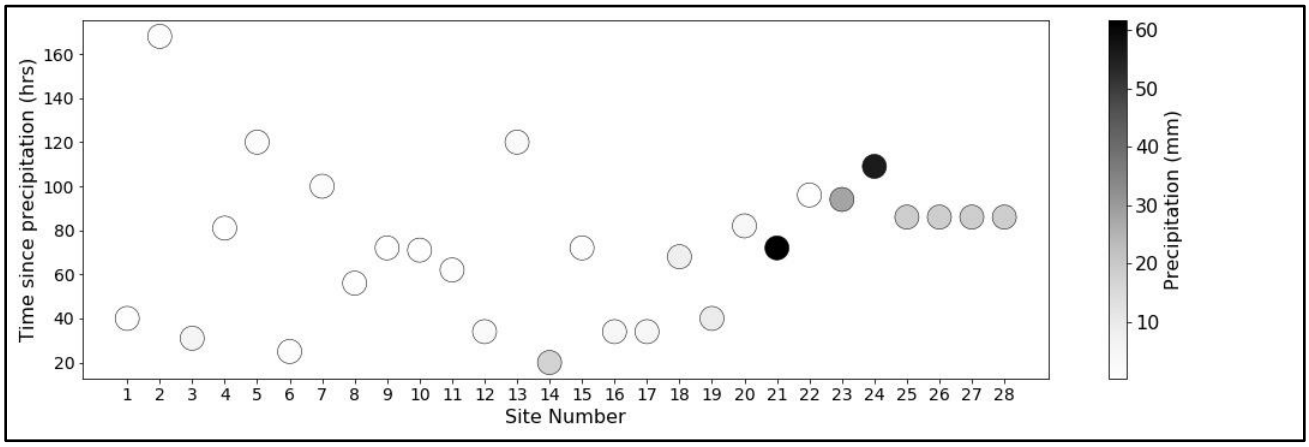

Fig. S9. Elapsed time between image acquisition and measurable precipitation and the precipitation amount for each of the 28 study sites.

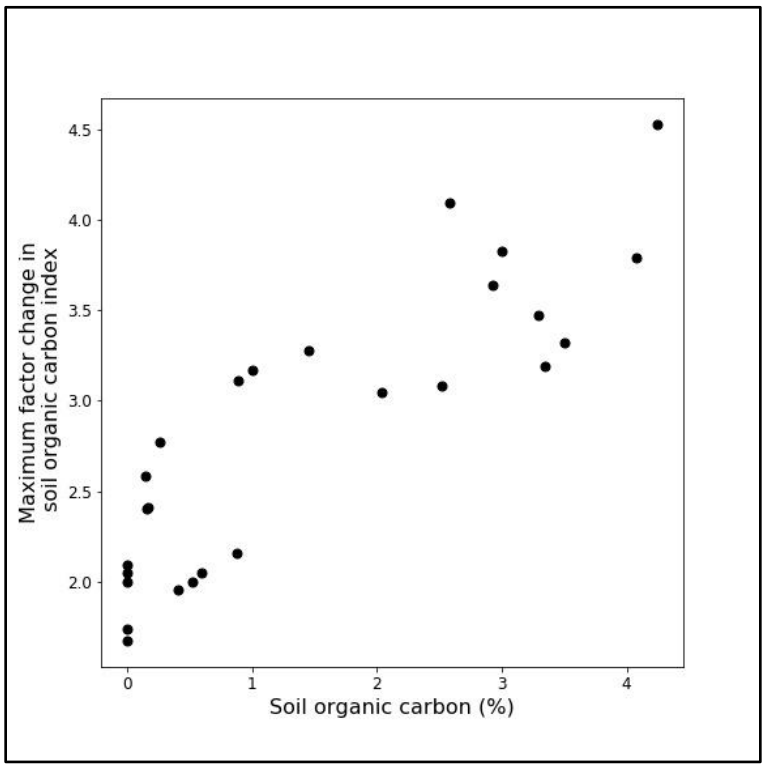

Fig. S10. The factor change in the soil organic carbon index between the dry samples and samples saturated to their maximum gravimetric moisture level for 26 soil samples as a function of soil organic carbon content.

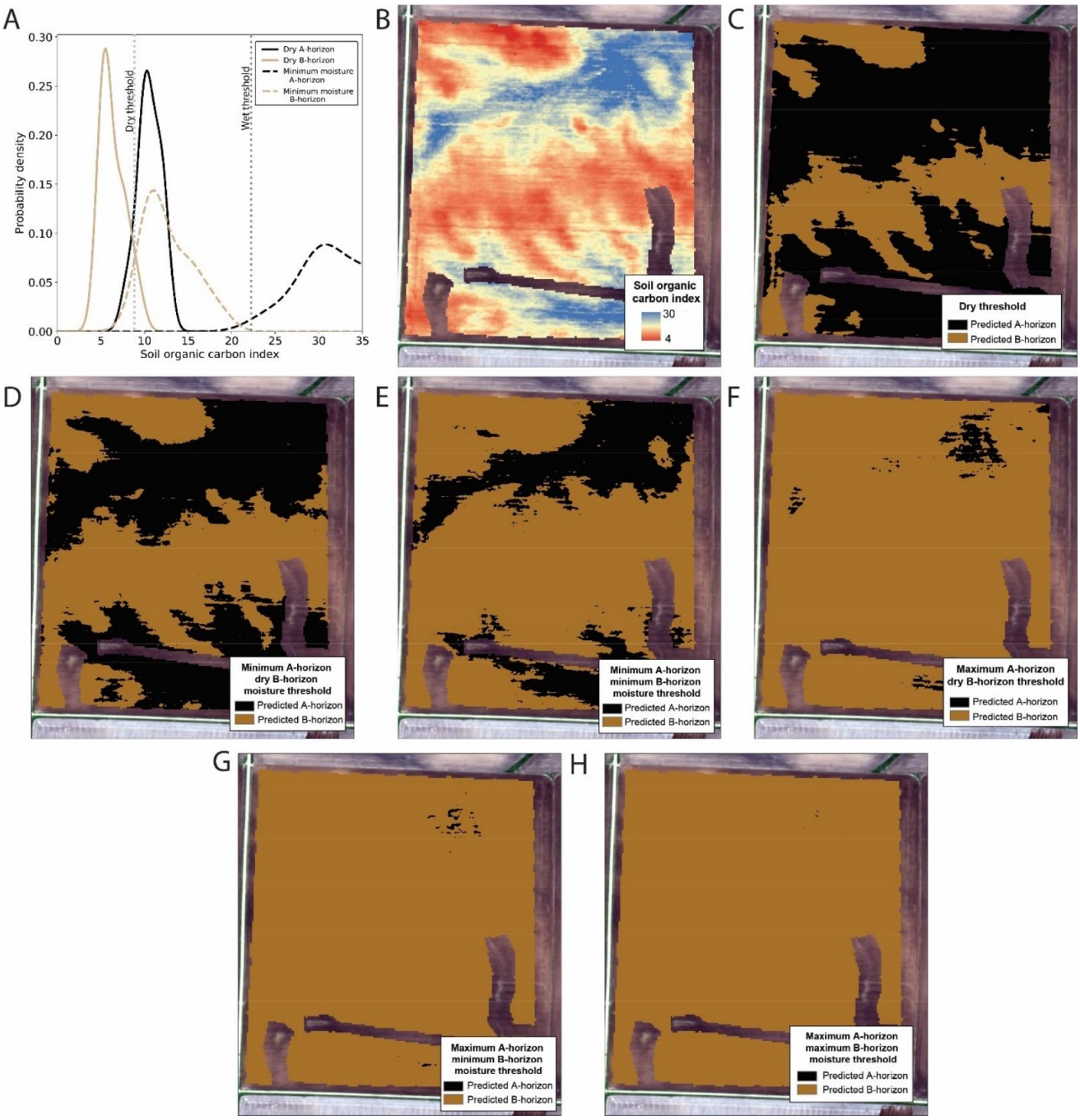

Fig. S11. An example of the threshold sensitivity to soil moisture using data from Site 2. A) Distribution of the A-horizon (black) and B-horizon (tan) soil organic carbon index (SOCI) values for the RaCA samples within 50 km of the field. The SOCI values for dry soils are shown as solid lines, and the SOCI values adjusted for soil moisture are shown as dashed lines. In this example, both the A- and B-horizon SOCI values were increased by a factor of three and two, respectively, which is the minimum response to soil moisture (from Fig. S10). Vertical dashed lines show the SOCI value which represents the 50% probability threshold of a sample being B-horizon for the dry (light gray) and wet (dark gray) distributions. The SOCI values less than the threshold are classified as B-

horizon. B) The SOCI values calculated from the satellite image, where red pixels indicate low SOCI values and blue pixels represent high SOCI values. Panels C-H demonstrate the influence of moisture-induced threshold changes on the classification of pixels. C) Pixel classification using threshold from dry samples, which is the method used in our study. D) Pixel classification using A-horizon samples shifted by the minimum moisture effect and dry B-horizon samples. E) Pixel classification using A- and B-horizon samples shifted by the minimum moisture effect. F) Pixel classification using A-horizon samples shifted by the maximum moisture effect and dry B-horizon samples. G) Pixel classification using A-horizon samples shifted by the maximum moisture effect and B-horizon samples shifted by the minimum moisture effect. H) Pixel classification using A- and B-horizon samples shifted by the maximum moisture effect. In all cases (D-H) the addition of soil moisture increases the proportion of pixels classified as B-horizon relative to the calibration based on spectra from dry soil samples (C). Image credit: ©2013 DigitalGlobe, Inc., a Maxar company, NextView License

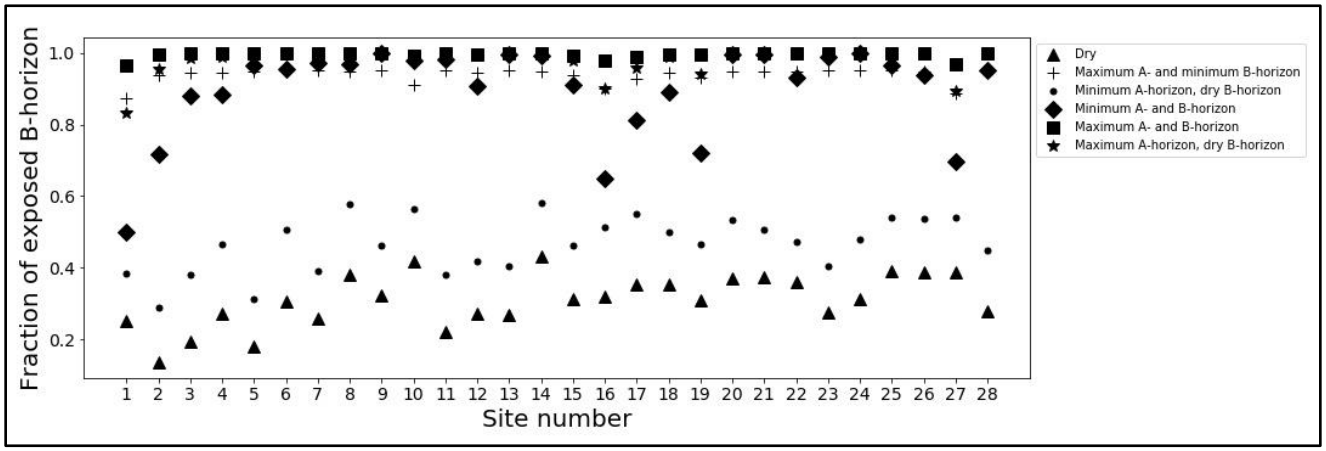

Fig. S12. The fraction of exposed B-horizon soils for each site calculated using a range of A- and B-horizon probability thresholds determined by adjusting the SOCI values measured on USDA Rapid Carbon Assessment (RaCA) soil samples to account for varying degrees of soil saturation.
Triangles represent predicted B-horizon exposure using a threshold calculated from dry samples (non-adjusted values from the RaCA dataset) and are the values reported in the main text. The threshold was also calculated using soil organic carbon values adjusted for the maximum and minimum effects of soil saturation on A- and B-horizon samples (from Fig. S10). With any adjustment to the threshold to simulate moisture effects, the fraction of exposed B-horizon increases above that determined using the threshold calculated from the dry samples, indicating that our reported estimates of B-horizon exposure loss would be minimum values if the visible spectra recorded in the images we used were influenced by soil moisture.

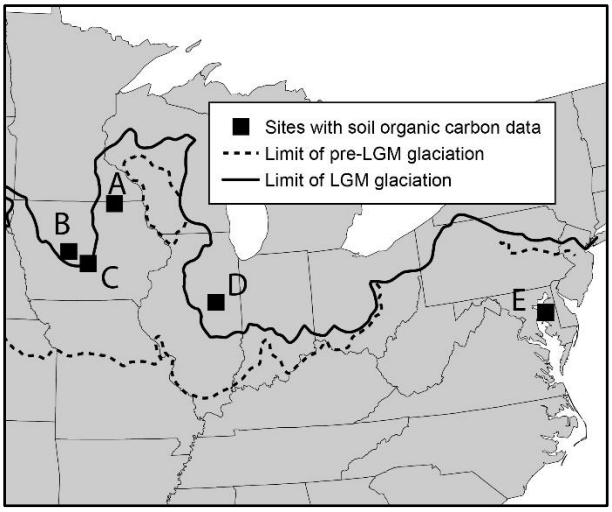

Fig. S13. Map showing locations of sites with field samples of soil organic carbon with satellite images of plowed fields with bare soil. Letters correspond to Fig. S14.

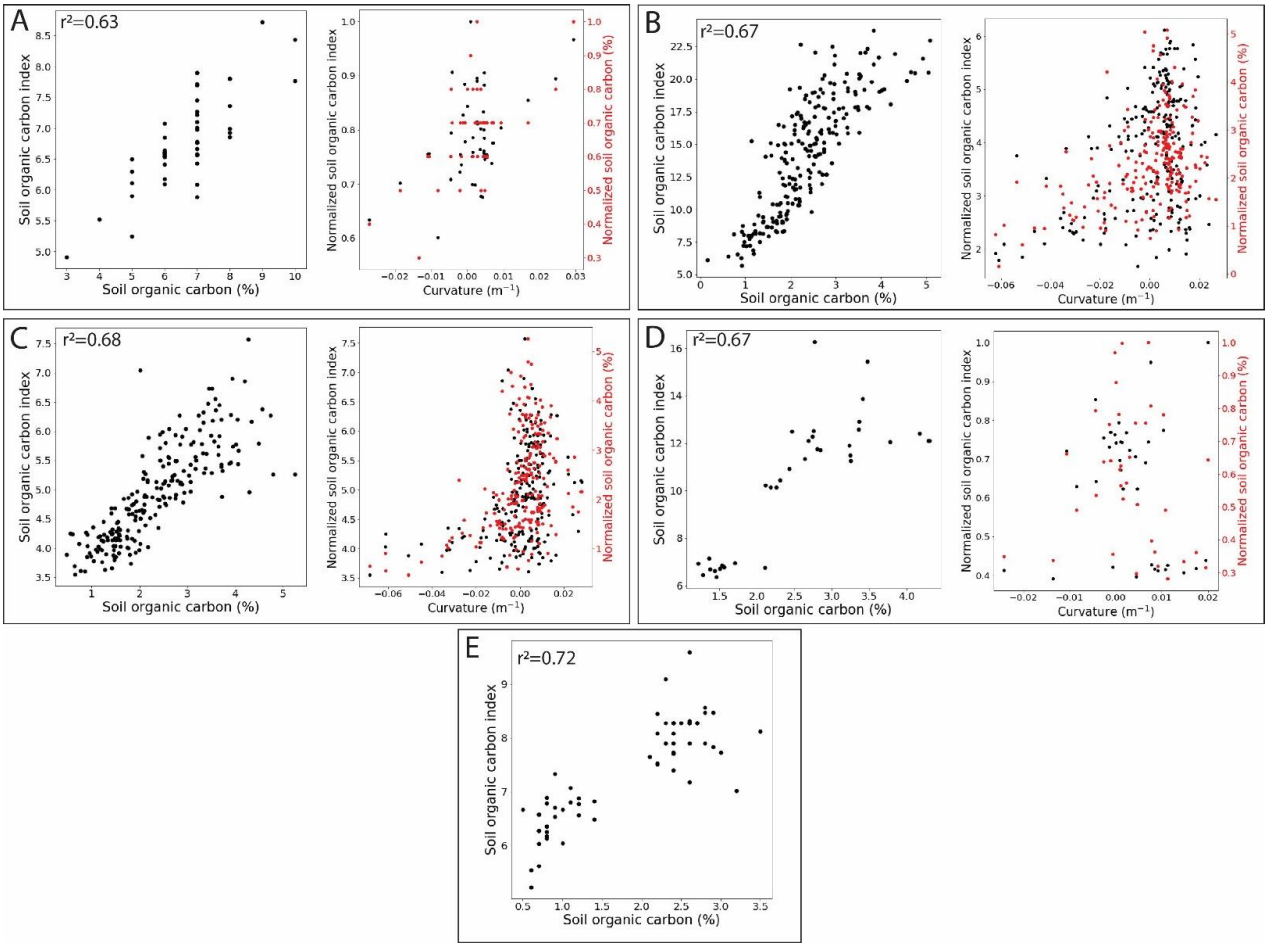

Fig. S14. The soil organic carbon index (SOCI) versus soil organic carbon (SOC) (left plot in each set) for sites A-E in Fig. S13. The normalized SOCI and normalized SOC versus topographic curvature for sites A-D (right plot in each set). The SOCI and SOC data were normalized by their maximum values to display their covariation with topographic curvature. Low soil organic carbon values are observed on convex hilltops (negative curvature), and the highest soil organic carbon values are found on concave topography (positive curvature). The R^2 values for the relationships between SOC versus curvature and the SOCI versus curvature are: Site A: 0.32 ($p < 0.01$) and 0.27 ($p < 0.01$), respectively; Site B: 0.15 ($p < 0.01$) and 0.14 ($p < 0.01$), respectively; Site C: 0.16 ($p < 0.05$) and 0.13 ($p < 0.05$), respectively; Site D: 0.1 ($p < 0.05$) and 0.1 ($p < 0.05$), respectively. Number of points for each site: A=51, B=228, C=217, D= 36, E=75.

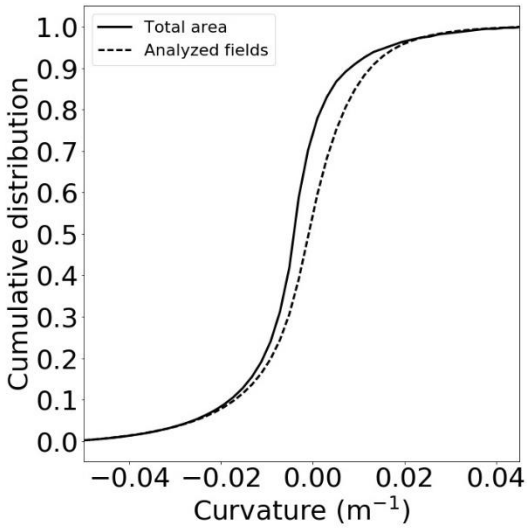

Fig. S15. Cumulative area of topographic curvature for the entire study region (solid line) and the analyzed fields (dashed line). 77% of the pixels in the full study region are located on convex topography, and 50% of pixels in the 210 km^2 of fields that were analyzed are on convex topography.

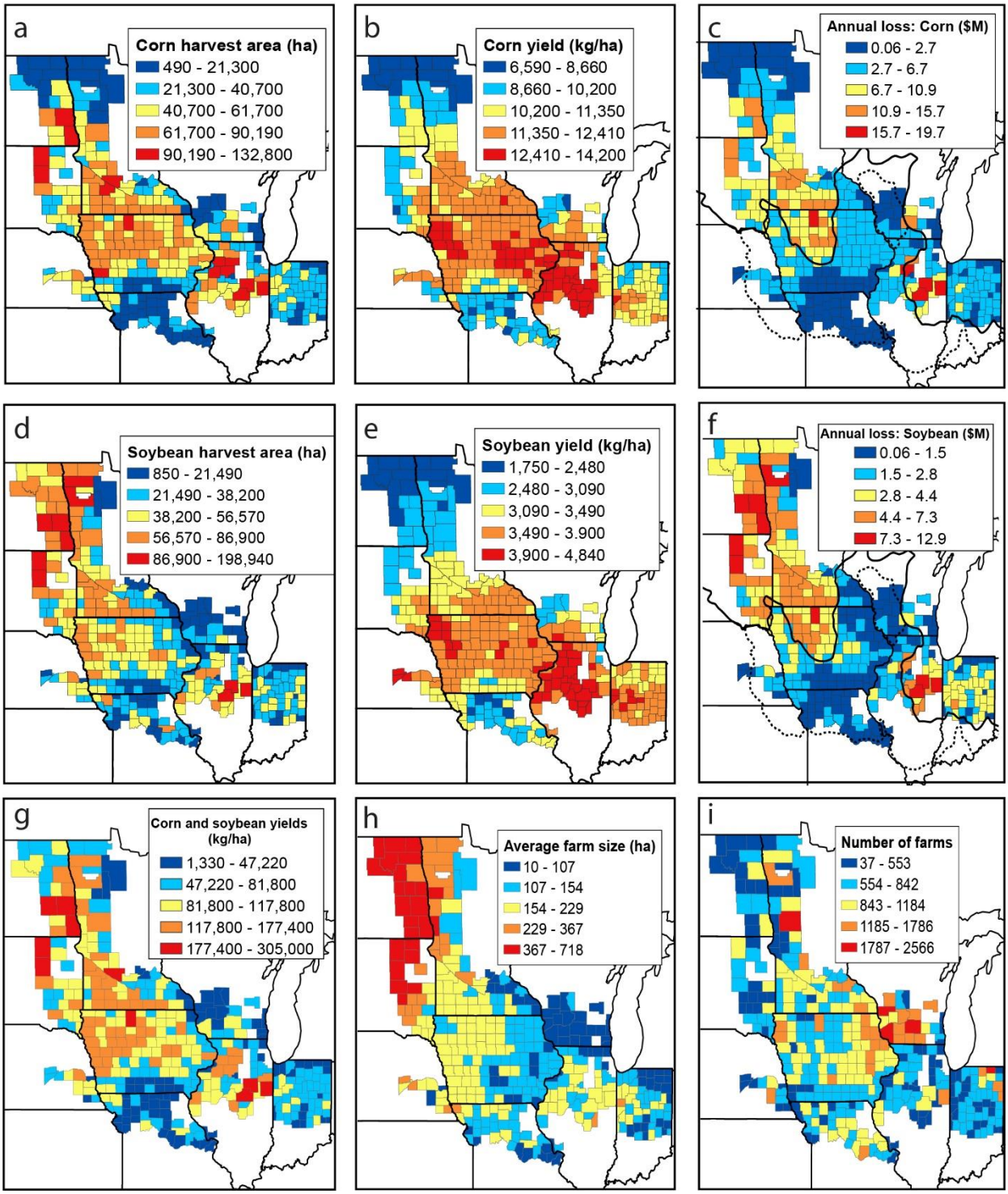
a
Corn harvest area (ha)
490 - 21,300
21,300 - 40,700
40,700 - 61,700
61,700 - 90,190
90,190 - 132,800
b
Corn yield (kg/ha)
6,590 - 8,660
8,660 - 10,200
10,200 - 11,350
11,350 - 12,410
12,410 - 14,200
c
Annual loss: Corn ($M)
0.06 - 2.7
2.7 - 6.7
6.7 - 10.9
10.9 - 15.7
15.7 - 19.7
d
Soybean harvest area (ha)
850 - 21,490
21,490 - 38,200
38,200 - 56,570
56,570 - 86,900
86,900 - 198,940
e
Soybean yield (kg/ha)
1,750 - 2,480
2,480 - 3,090
3,090 - 3,490
3,490 - 3.900
3,900 - 4,840
f
Annual loss: Soybean ($M)
0.06 - 1.5
1.5 - 2.8
2.8 - 4.4
4.4 - 7.3
7.3 - 12.9
g
Corn and soybean yields (kg/ha)
1,330 - 47,220
47,220 - 81,800
81,800 - 117,800
117,800 - 177,400
177,400 - 305,000
h
Average farm size (ha)
10 - 107
107 - 154
154 - 229
229 - 367
367 - 718
i
Number of farms
37 - 553
554 - 842
843 - 1184
1185 - 1786
1787 - 2566

Fig. S16. Mean harvest area, mean crop yields, and mean annual economic losses for corn (a-c) and soybeans (d-f), the combined yields of corn and soybeans (g), the average farm size (h), and the number of farms in each county (i). Harvest area, yield data, number of farms are from the USDA (20). The glacial extent prior to the LGM and the extent during the LGM are shown as dashed and solid lines, respectively.

Fig. S17. [Below] Examples of B-horizon exposure and topographic curvature from each of our 28 study sites. The left panel is a true-color image with black polygons surrounding light-colored areas predicted to have exposed B-horion soil, and white polygons indicate ±1 S.D. of the predicted area of B-horizon exposure. The right panel is a topographic curvature map where red pixels denote negative curvature (convex topography) and blue pixels denote positive curvature (concave topography). The exposure of B-horizon soils is readily observable within each field, as is the spatial correlation between B-horizon exposure and negative curvature, which demonstrates the validity of our method. Image credit: ©2013-2016 DigitalGlobe, Inc., a Maxar company, NextView License.

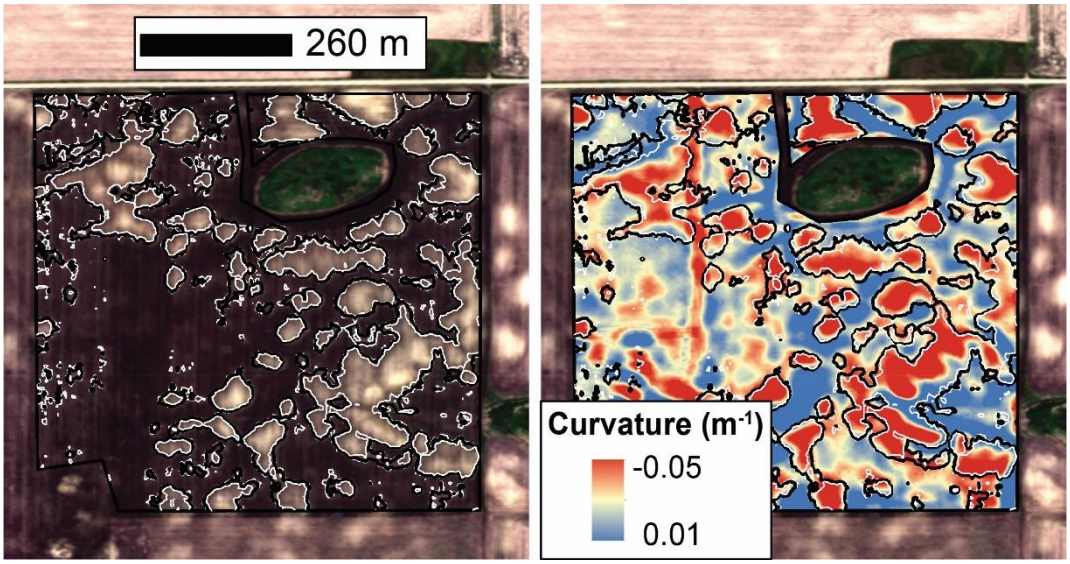

Site 1

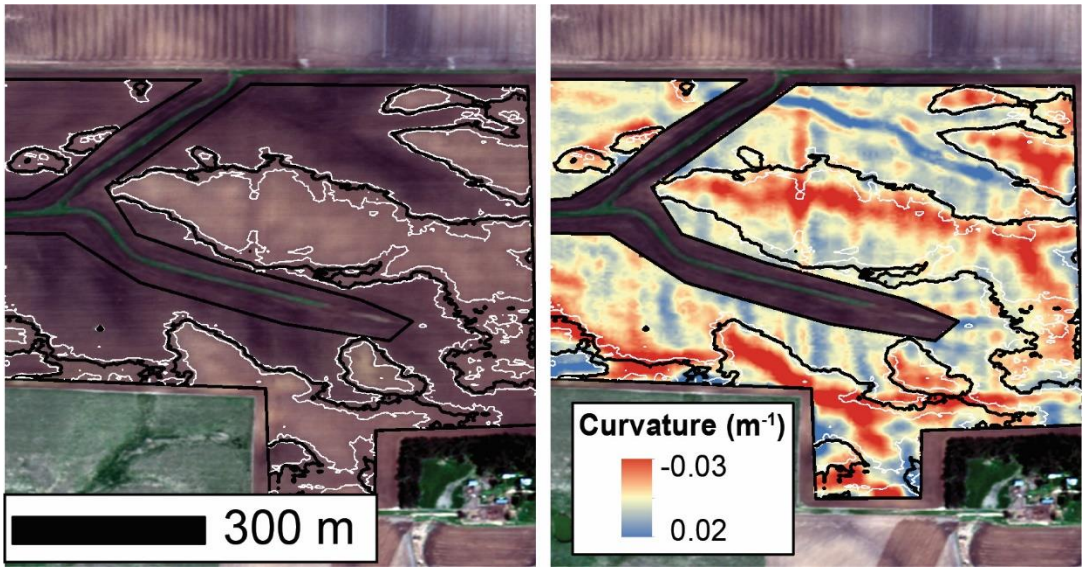

Site 2

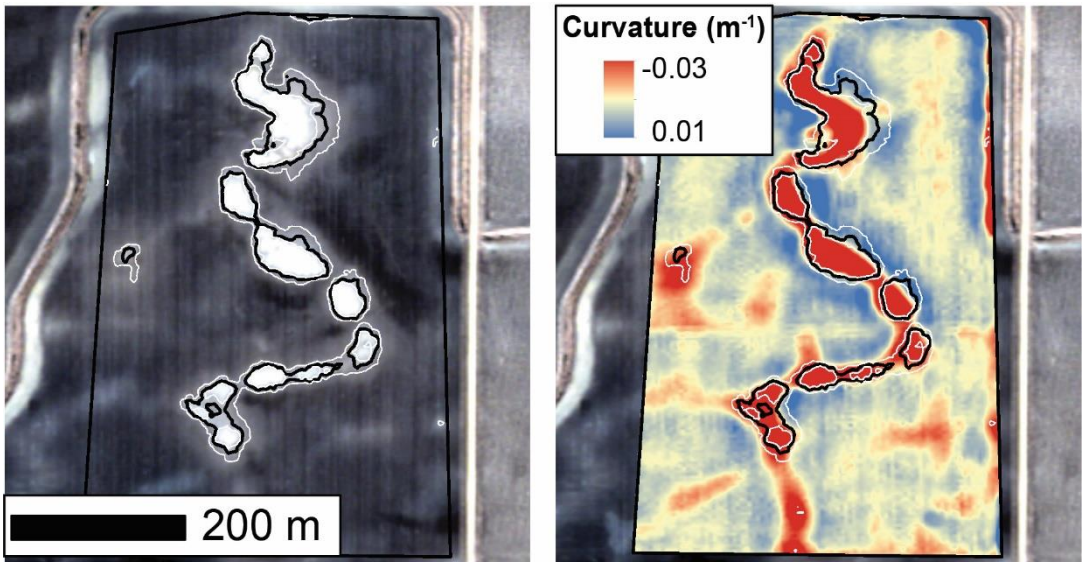

Site 3

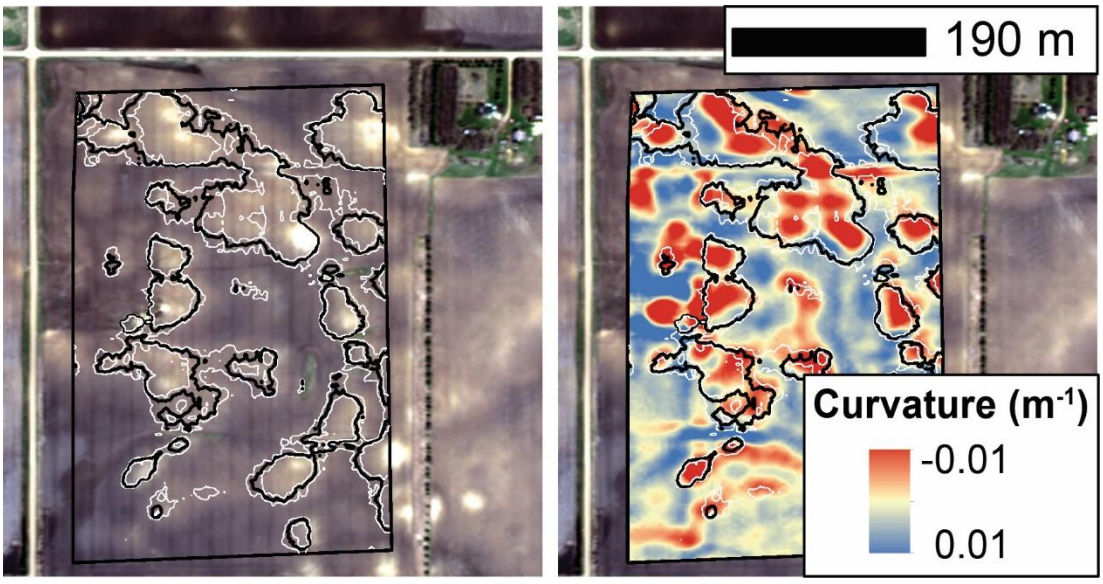

Site4

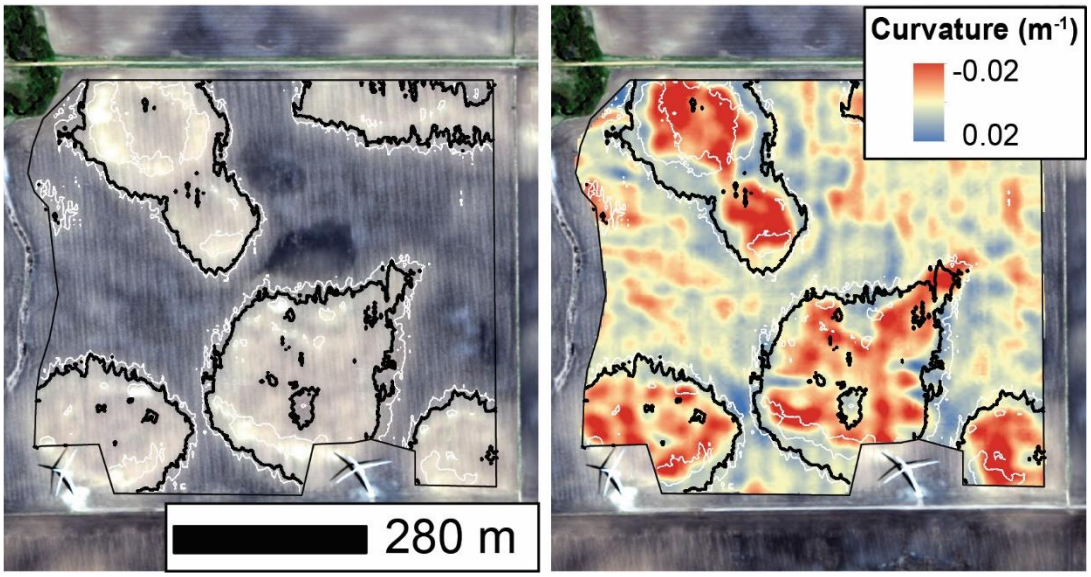

Site5

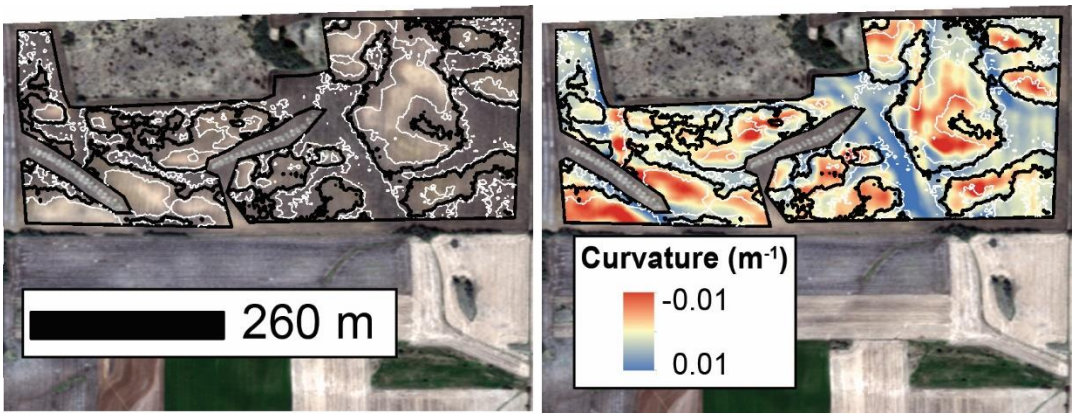

Site6

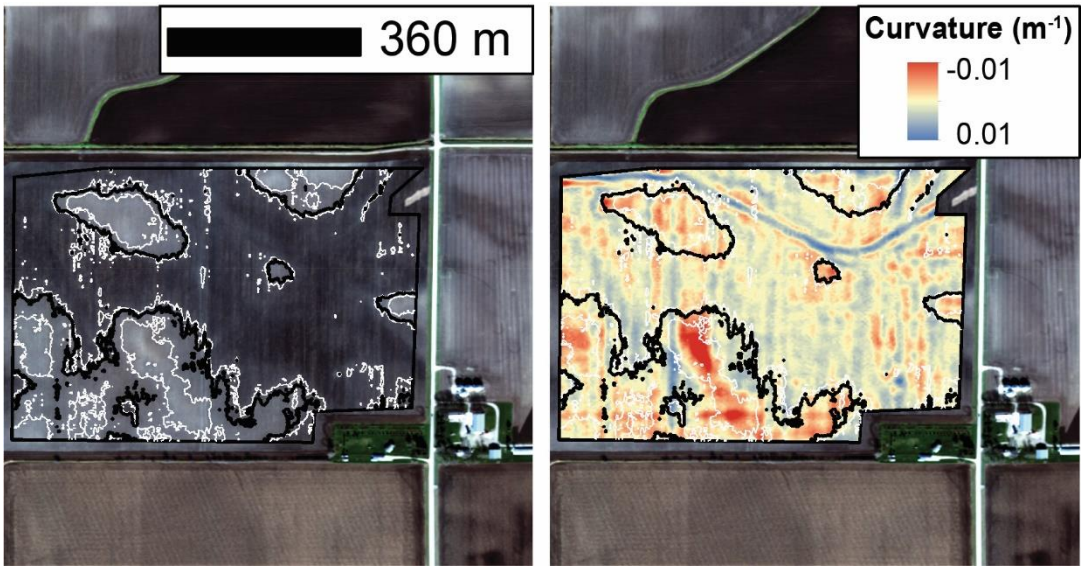

Site7

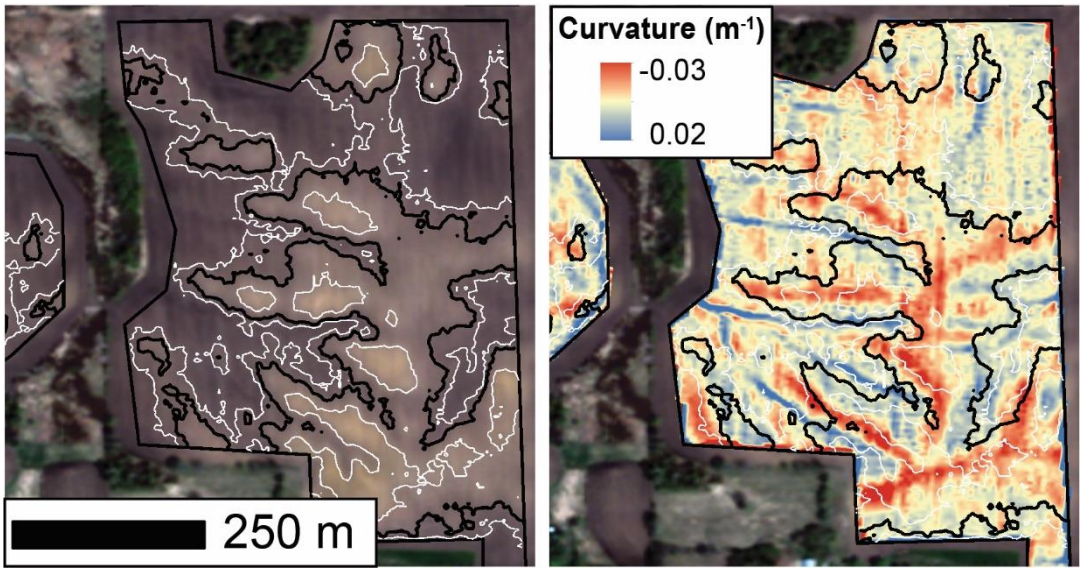

Site8

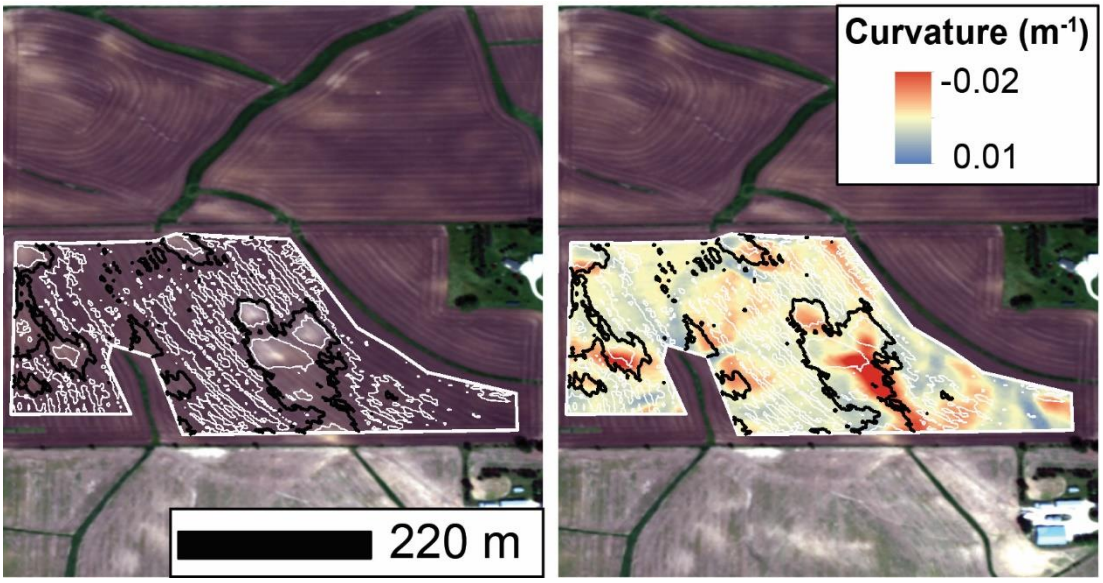

Site 9

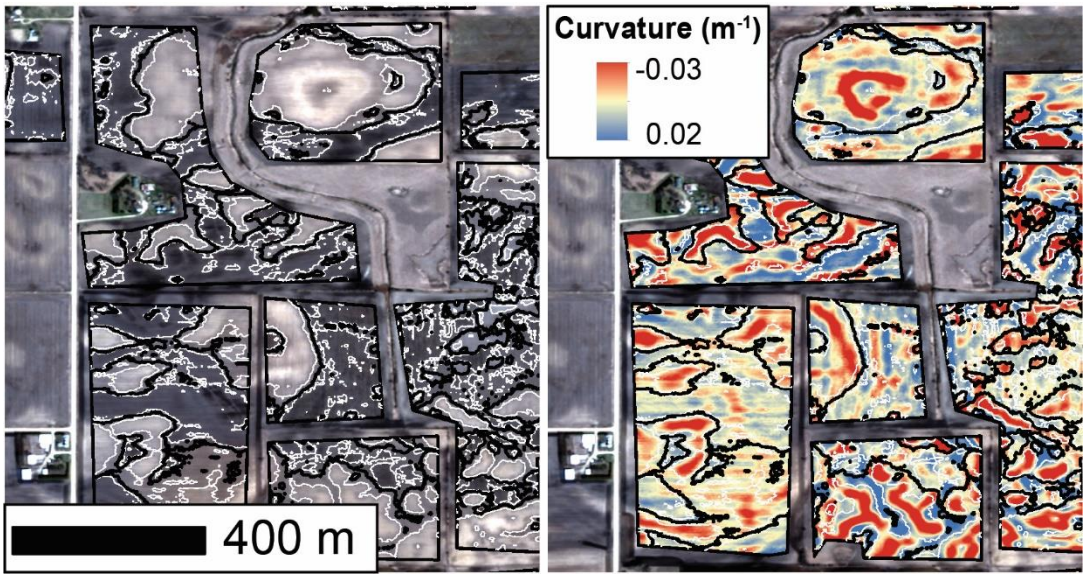

Site 10

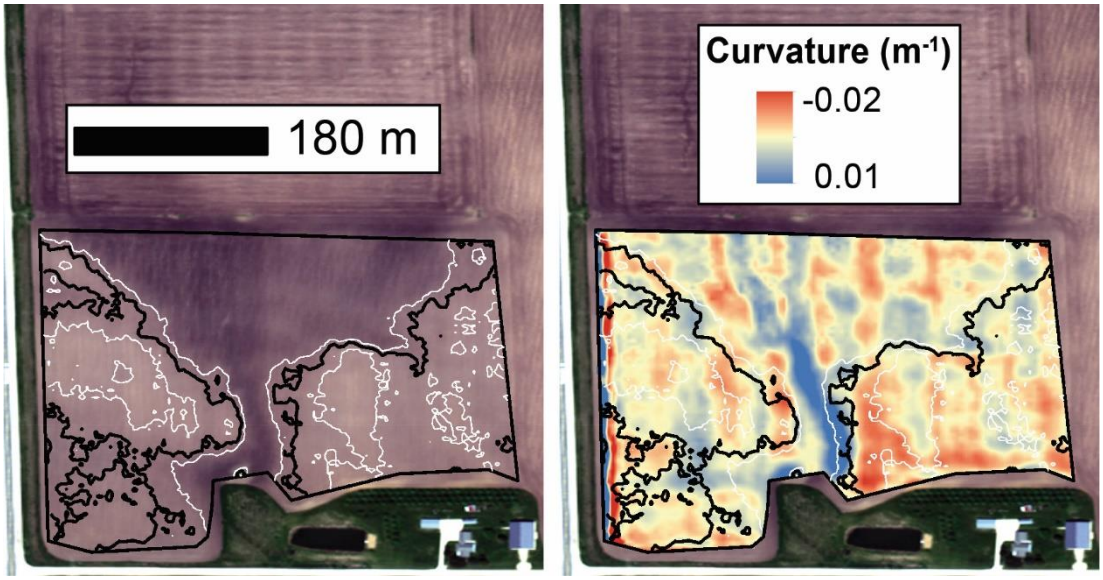

Site 11

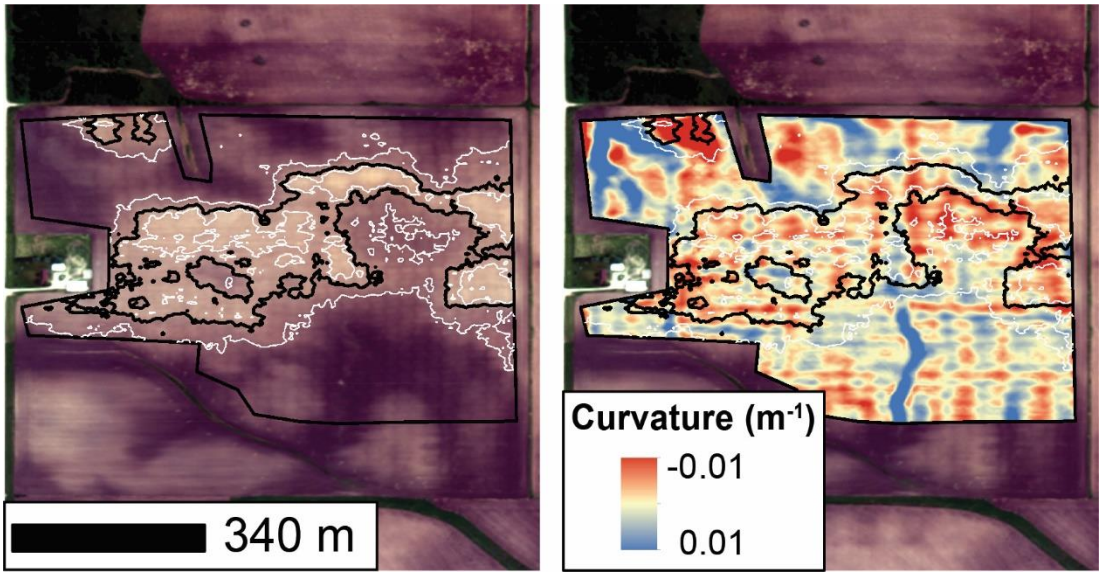

Site 12

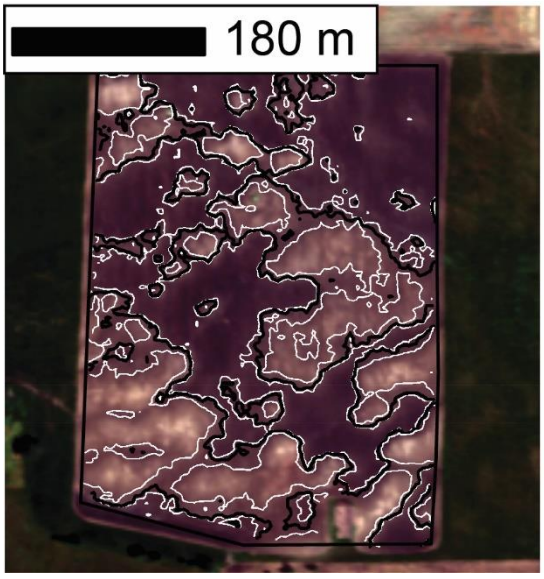

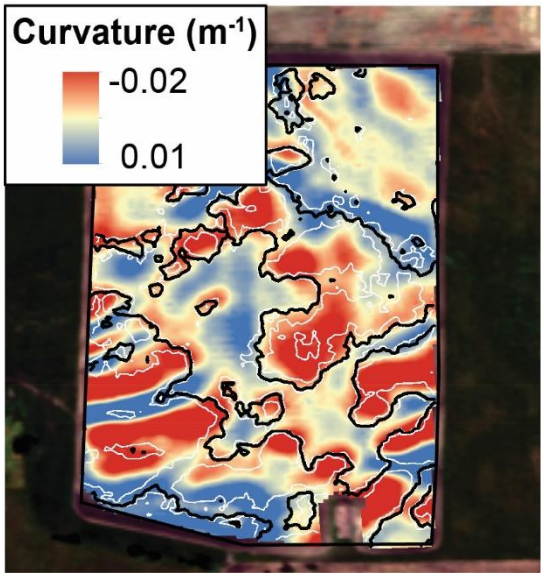

Site 13

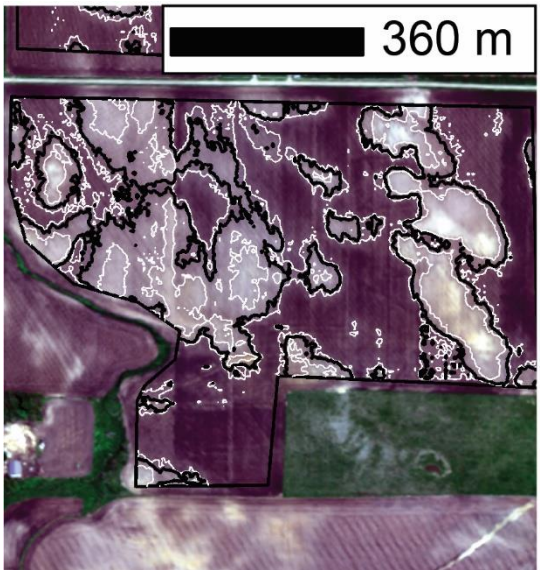

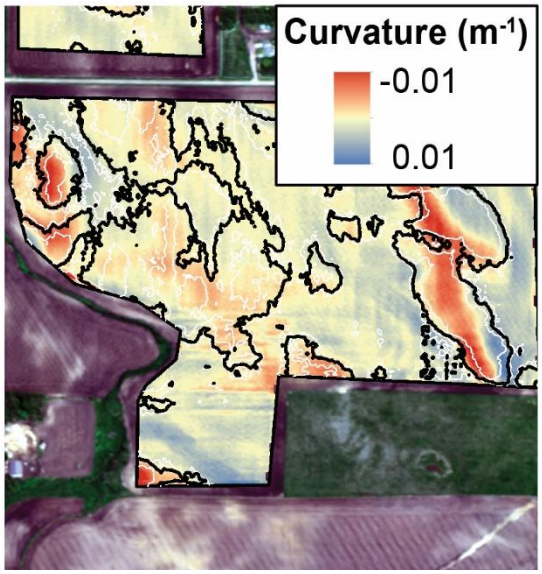

Site 14

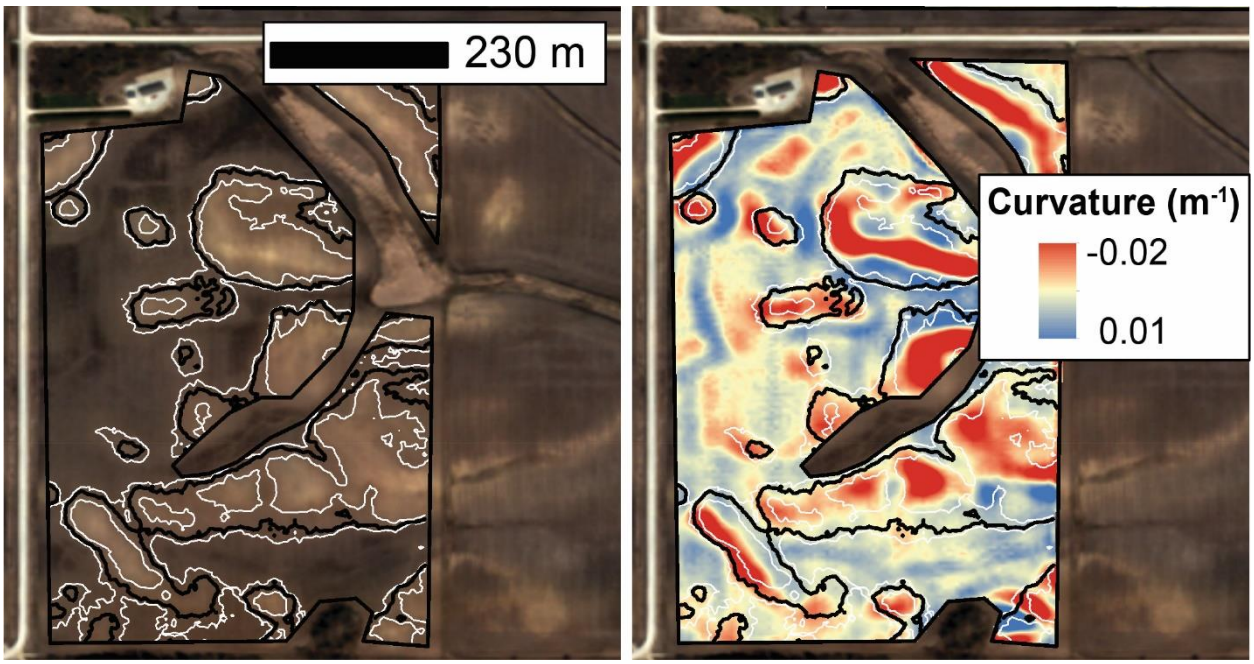

Site 15

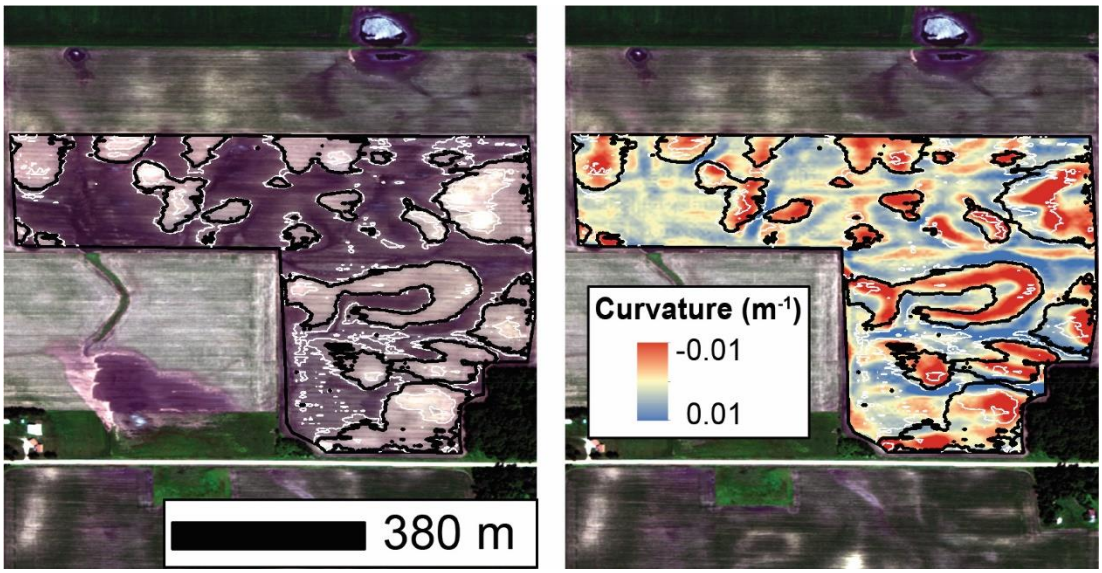

Site 16

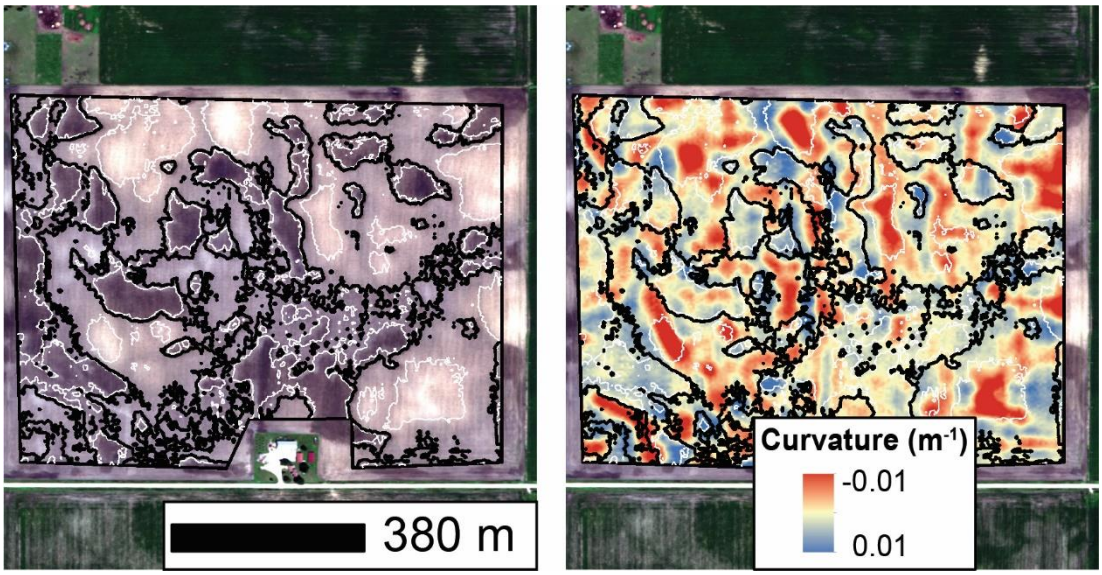

Site 17

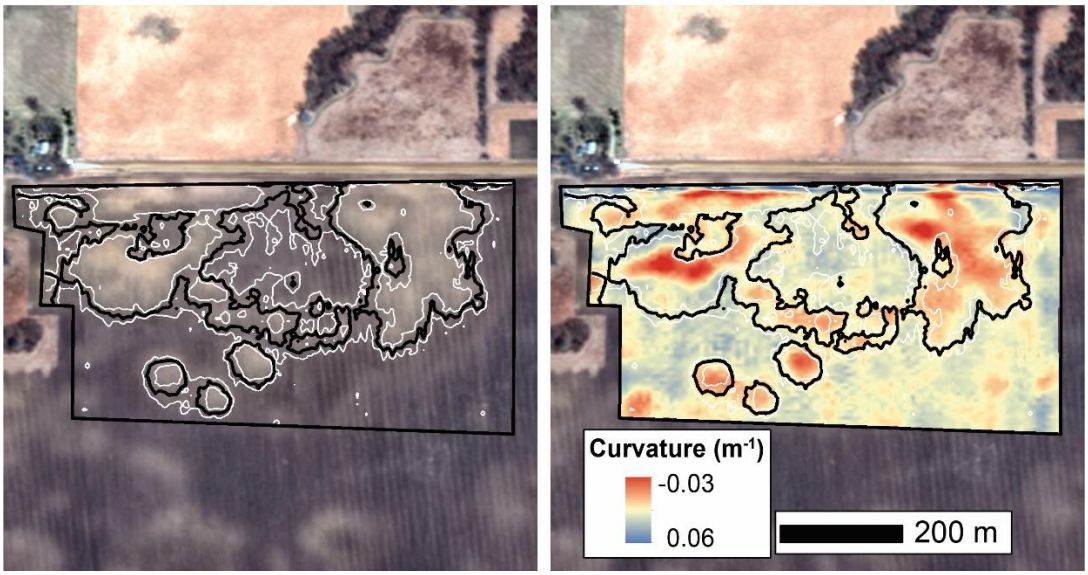

Site 18

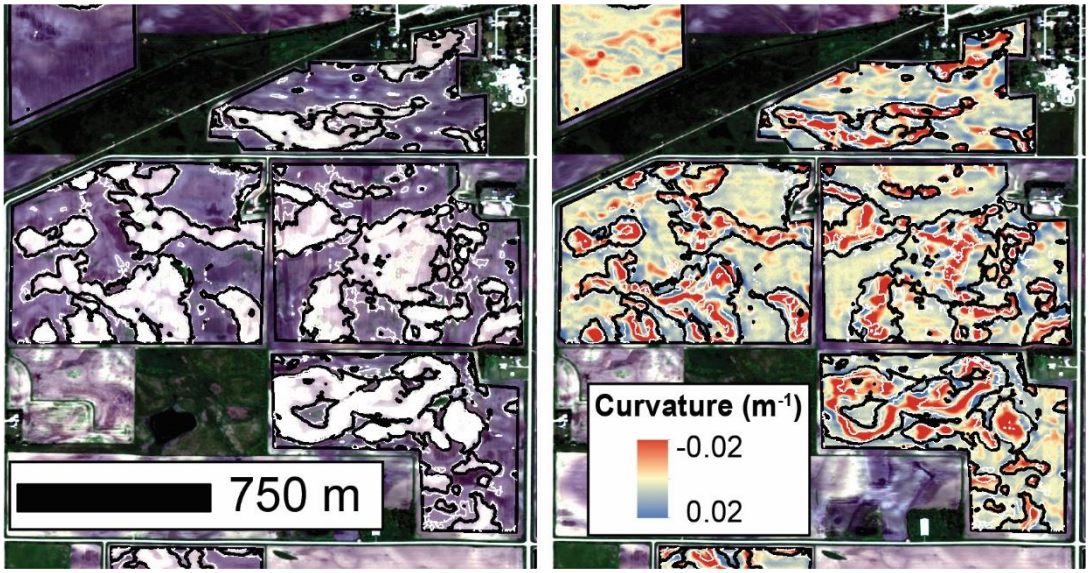

Site 19

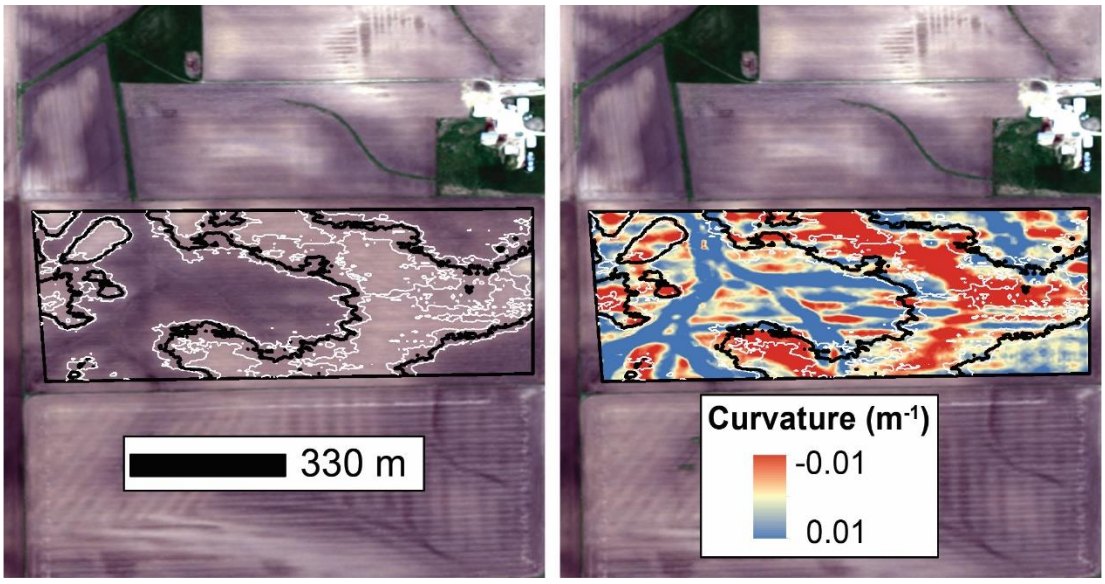

Site 20

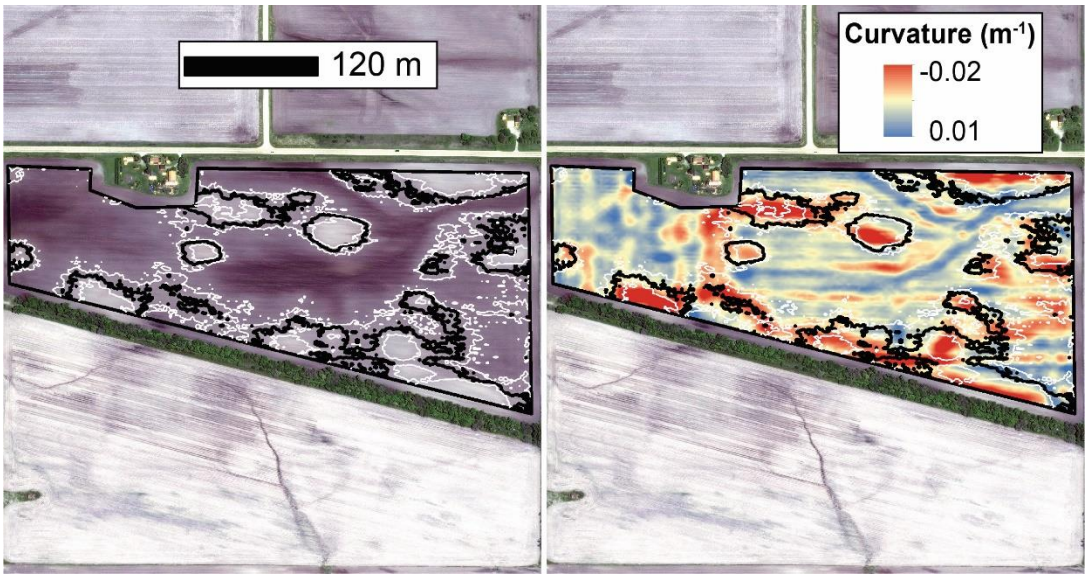

Site 21

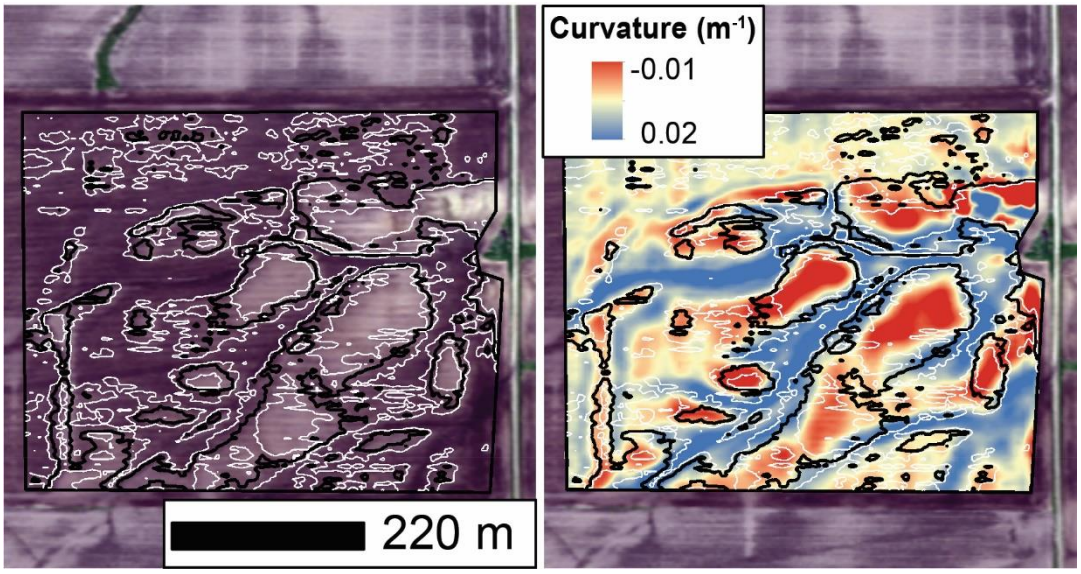

Site 22

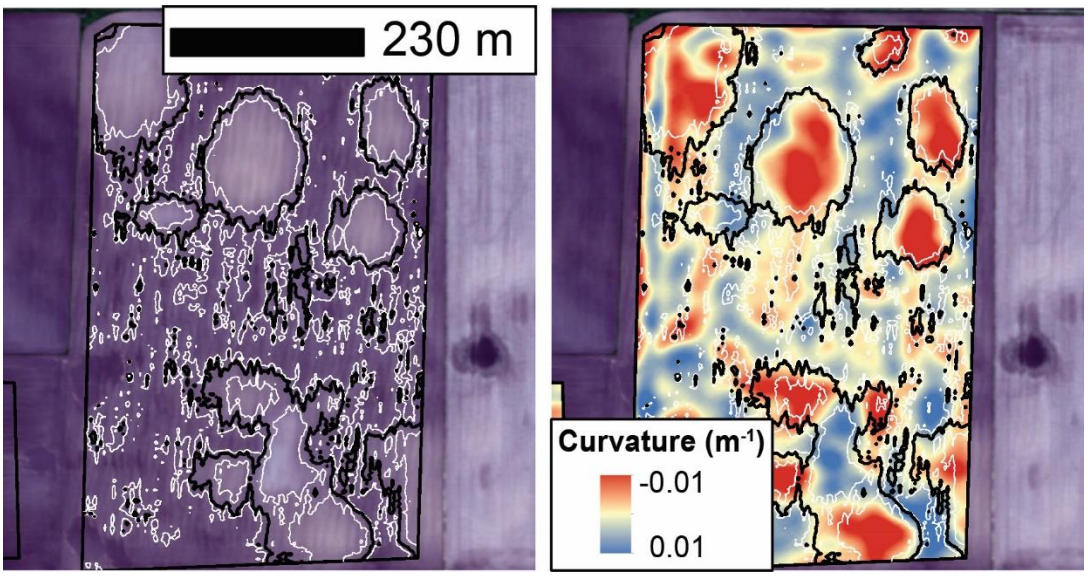

Site 23

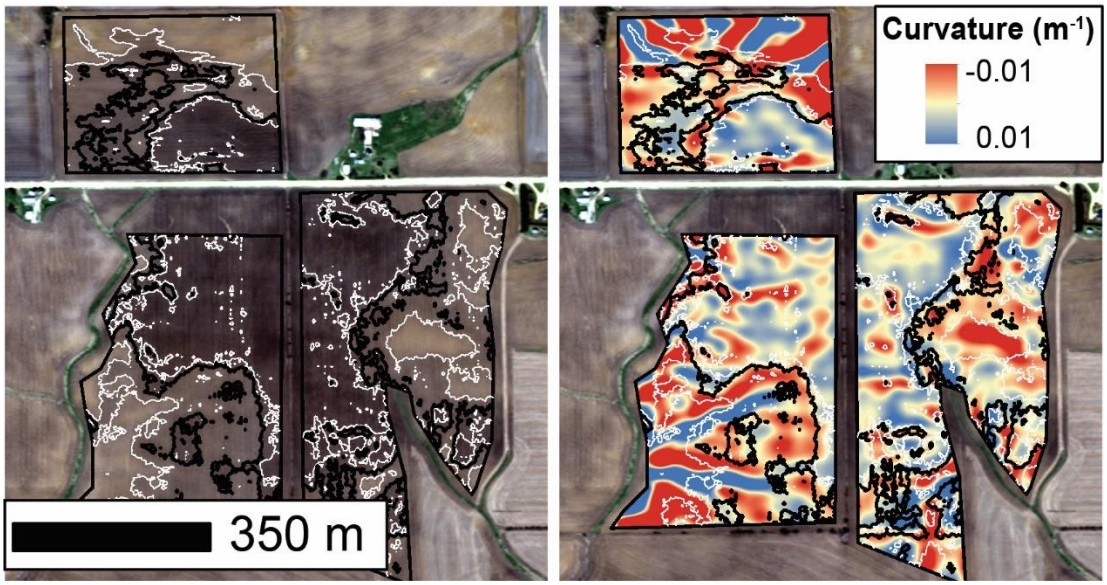

Site 24

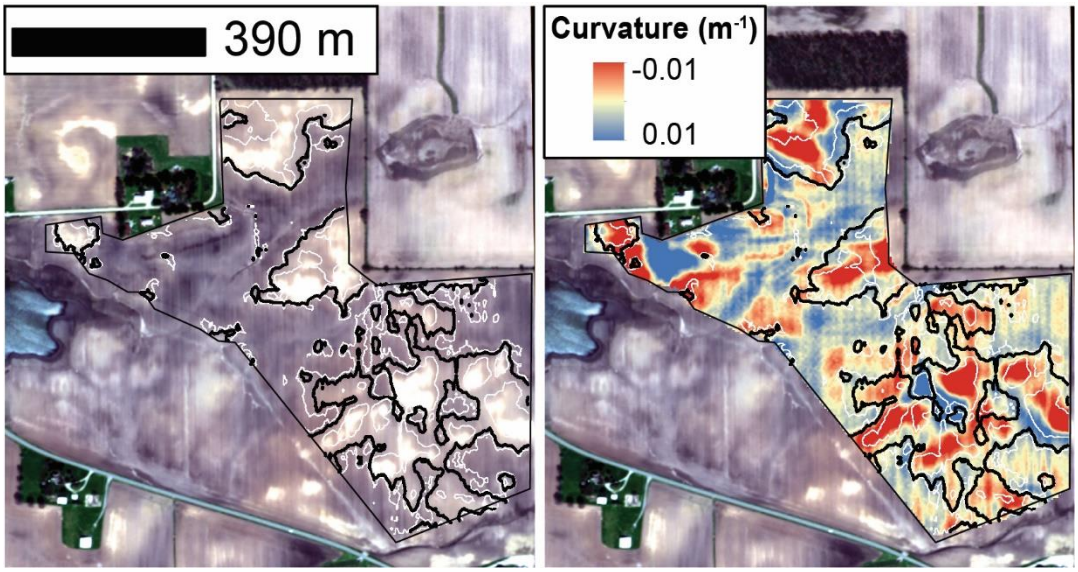

Site 25

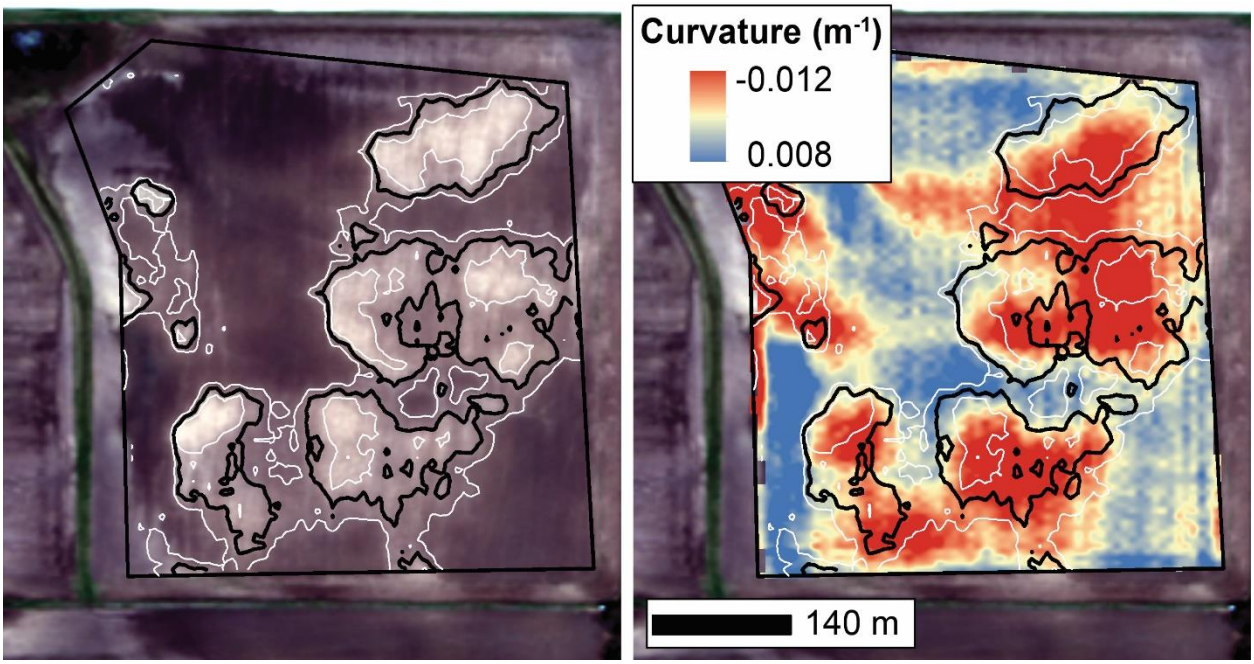

Site 26

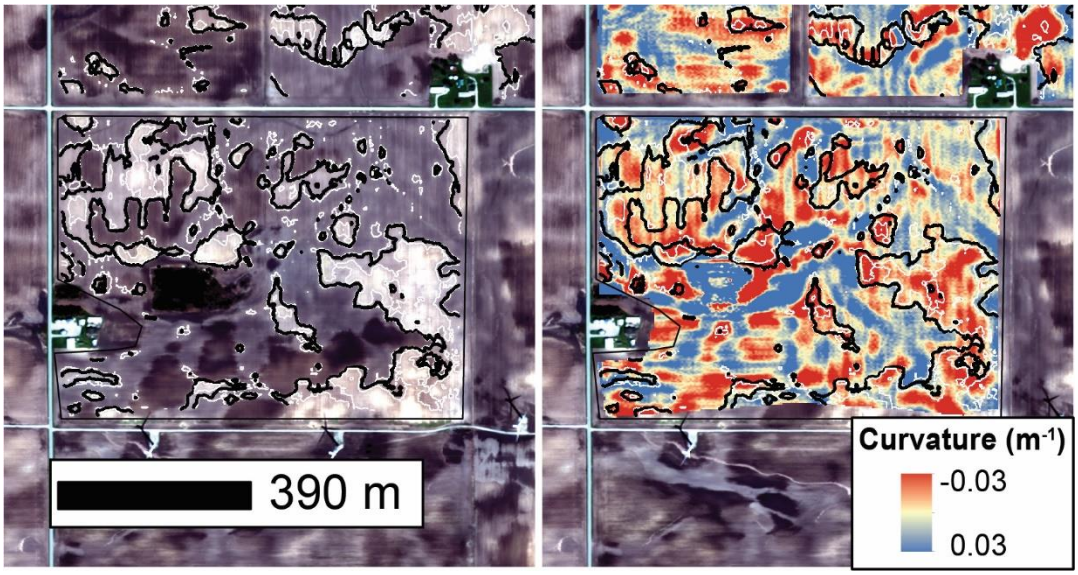

Site 27

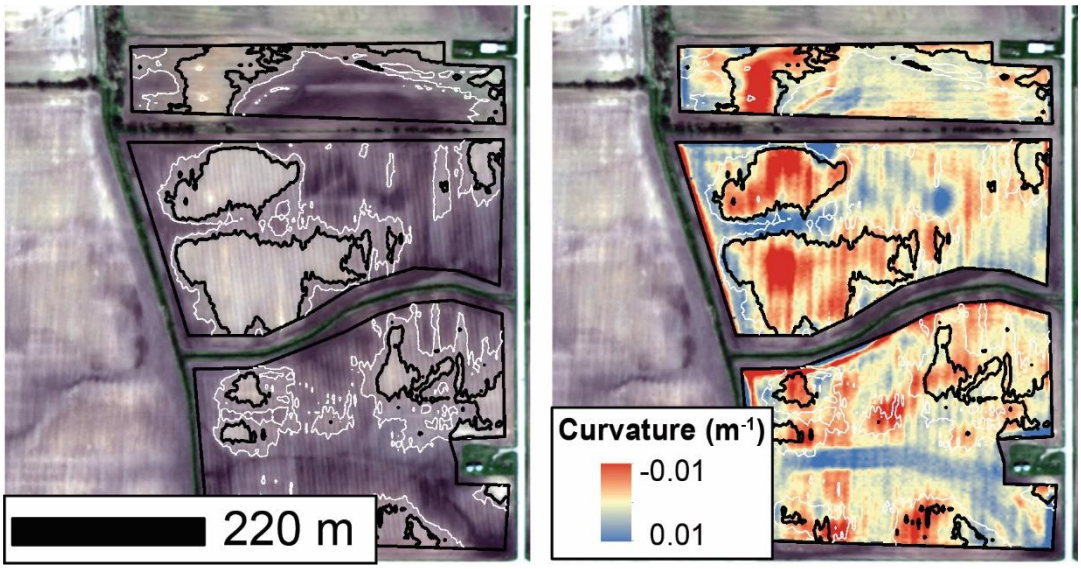

Site 28

Table B1. Citations, locations, and A-horizon thicknesses for 28 samples collected in native tallgrass prairies. The mean A-horizon thickness is 37 cm.

Study	Location	A-horizon thickness (cm)
Weaver and Hanson, 1941 (27)	Nebraska	45
Bockheim and Hartemink, 2017 (28)	Wisconsin	36 25 51 23
Blank and Fosberg, 1989 (29)	South Dakota	25
Steiger, 1930 (30)	Nebraska	43
Hirmas et al., 2013 (31)	Kansas	16
Rusle and Engle, 1925 (32)	Nebraska	30
Wills, 2005 (33)	Iowa	43 30 35 48 55 24 46 48 26 42 39 47 41 44 35 39 32 36 40 40 38

APPENDIX C

THE OTHER APPENDIX

Supplementary Materials for

Rates of historical anthropogenic soil erosion in the Midwestern United States

Evan A. Thaler[1], Isaac J. Larsen[1], Jeffrey S. Kwang[1], Brendon J. Quirk[1], and Caroline Lauth[1]

[1]*Department of Geosciences, University of Massachusetts, Amherst, MA 01003. 233 Morrill Science Center.*

Correspondence to: thaler.evan@gmail.com

This PDF file includes:

Figs. S1 to S4

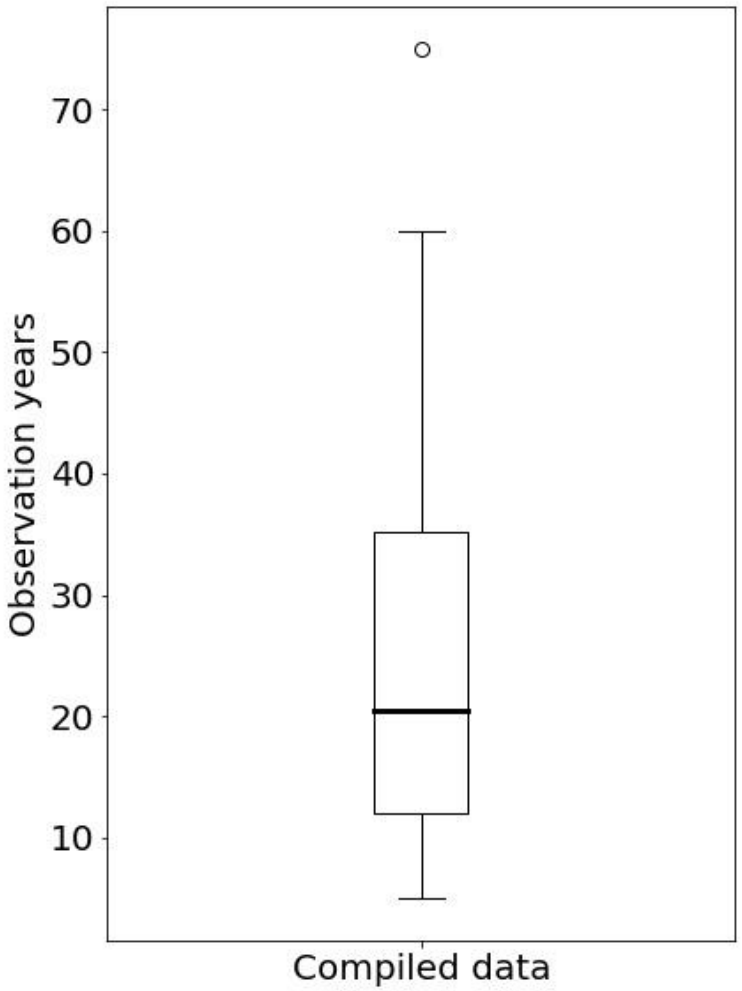

Fig S1. Boxplot of number of years of observations for the compilation of erosion rate estimates shown in Fig. 3c. The box spans the interquartile range; the black line is the median, and the bottom and top whiskers represent 5th and 95th percentiles, respectively. Outliers are shown as open circles.

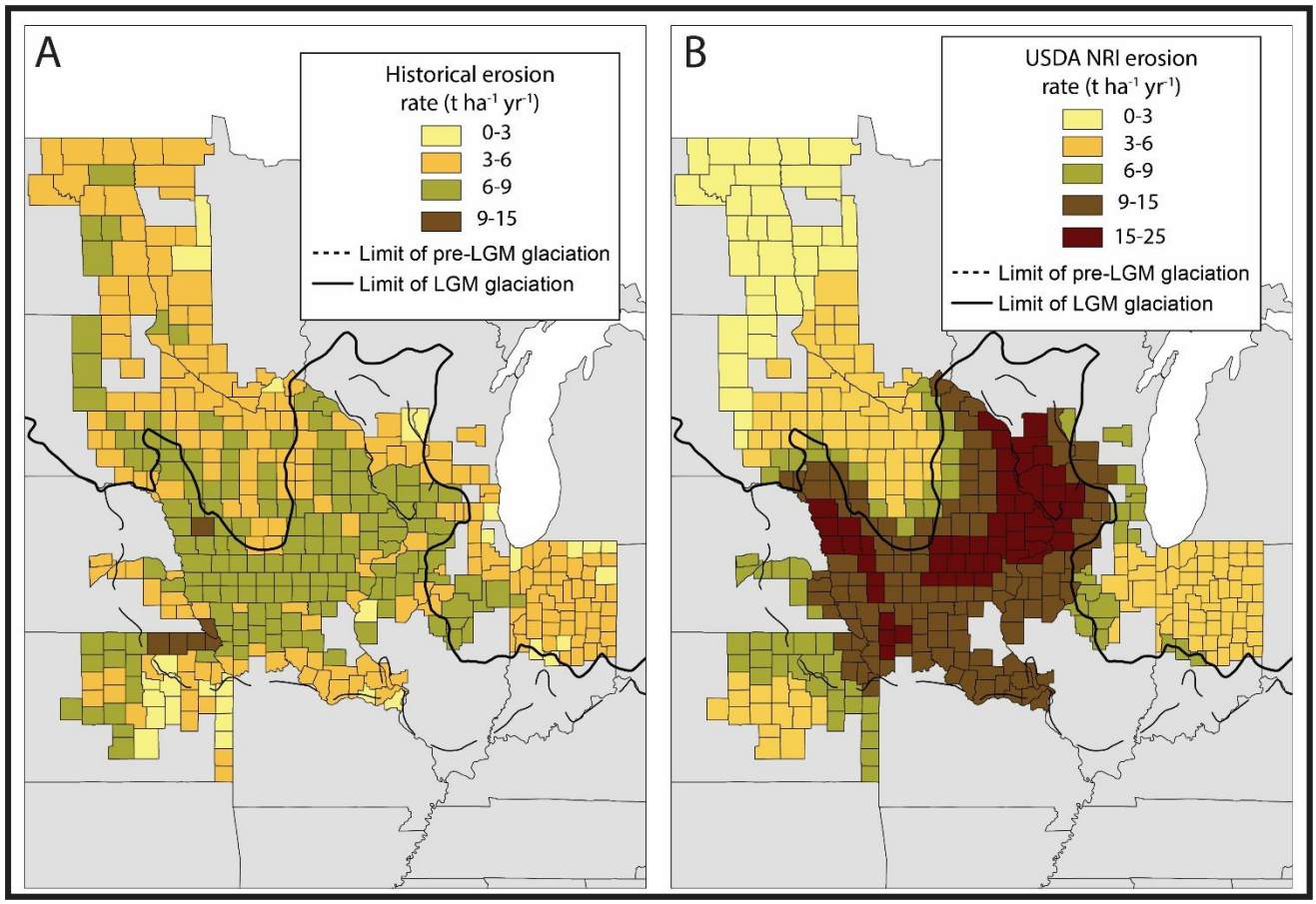

Fig S2. Maps of historical and present-day erosion rates. (A) County-level estimates of historical erosion rates (t ha^{-1} yr^{-1}) and **(B)** county-level estimates from the U.S. Department of Agriculture National Resources Assessment (USDA NRI).

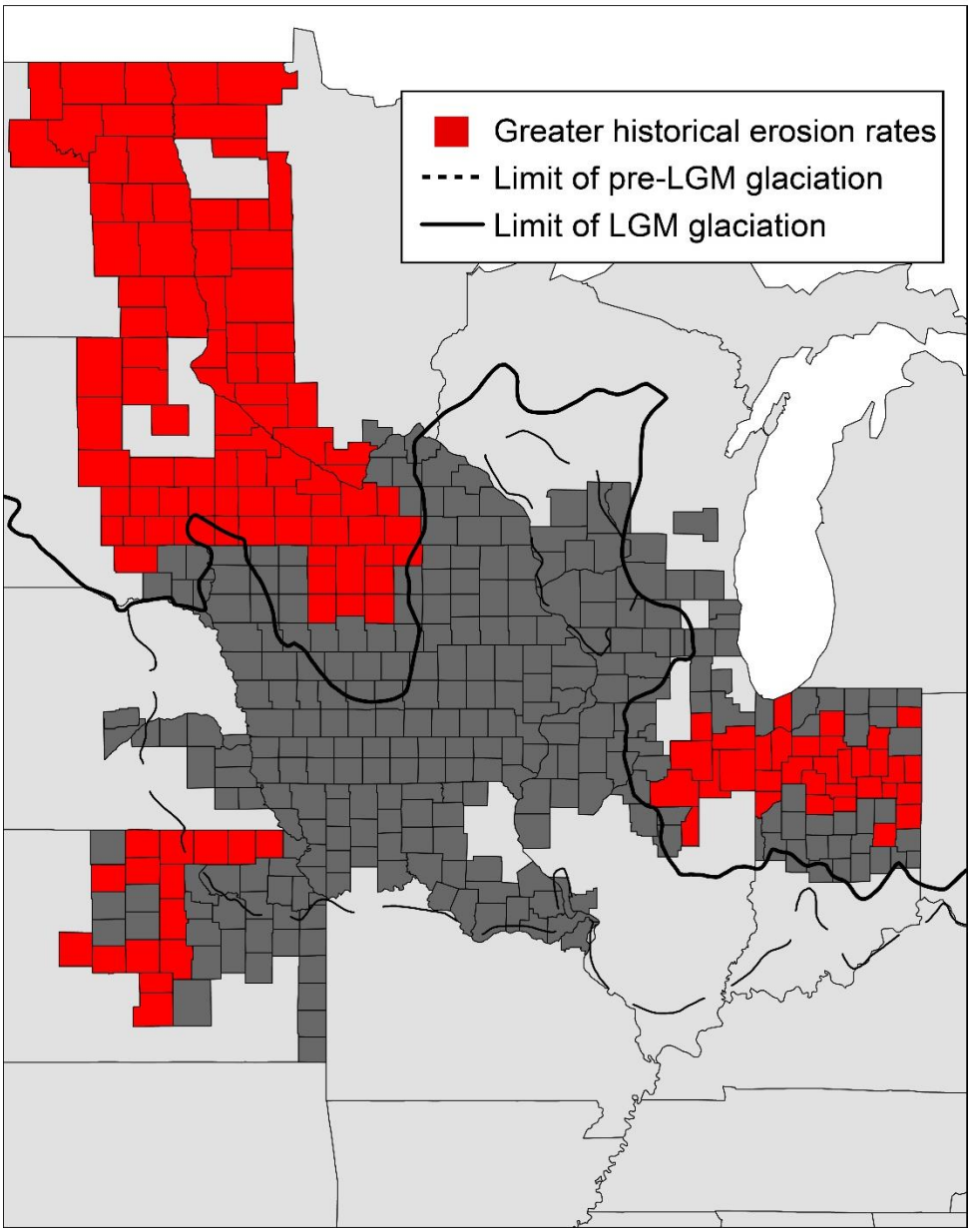

Fig S3. Map of counties where historical erosion rates predicted by our method exceed erosion rates estimated by the USDA NRI. The NRI estimates are lower than the historically averaged rates for counties in red. The solid line indicates the limit of the last glacial maximum (LGM) extent, and the dashed line indicates the maximum ice extent of previous glaciations. 115 of the 130 counties where NRI estimates are lower than the historically averaged rates are north of the LGM.

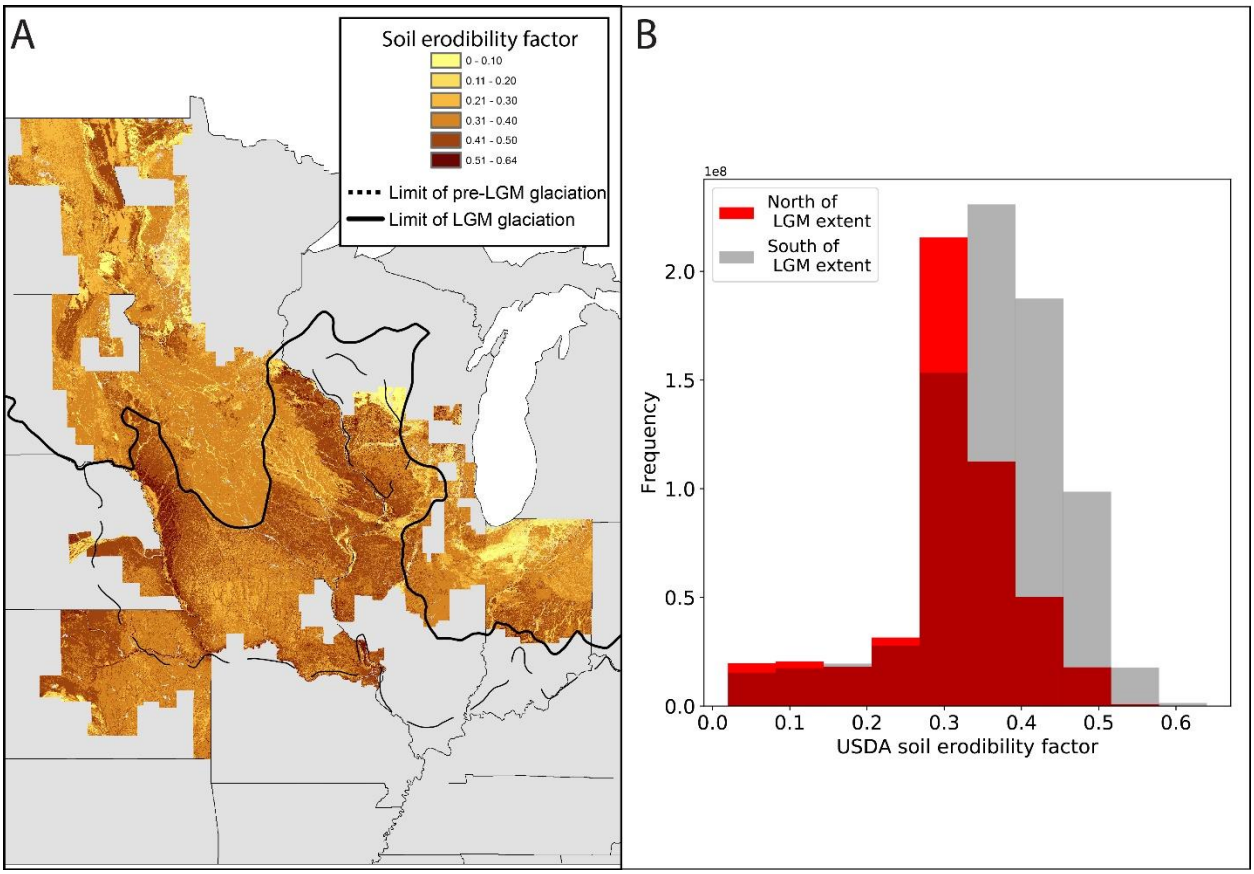

Fig S4. USDA Soil erodibility factor in relation to the last glacial maximum ice extent. A) Map of the USDA soil erodibility factor for the Midwestern U.S. Light-colored pixel indicate lower soil erodibility values, while higher values are indicated by darker pixels. The solid line indicates the limit of the last glacial maximum (LGM) extent, and the dashed line indicates the maximum ice extent of previous glaciations. B) Histogram of USDA soil erodibility factor values for all pixels north of the LGM extent (red bars) and south of the LGM extent (gray bars).

BIBLIOGRAPHY

Adams J.B., Smith M.O. and Johnson P.E. 1986. Spectral mixture modeling: A new analysis of rock and soil types at the Viking Lander 1 site. Journal of Geophysical Research: Solid Earth 91:8098-8112.

Aldana-Jague E., Heckrath G., Macdonald A., van Wesemael B. and Van Oost K. 2016. UAS-based soil carbon mapping using VIS-NIR (480–1000 nm) multi-spectral imaging: Potential and limitations. Geoderma 275:55-66.

Amundson R., Berhe A.A., Hopmans J.W., Olson C., Sztein A.E. and Sparks D.L. 2015. Soil science. soil and human security in the 21st century. Science 348:1261071.

Amundson R. and Biardeau L. 2018. Opinion: Soil carbon sequestration is an elusive climate mitigation tool. Proceedings of the National Academy of Sciences 115:11652-11656.

Bachofer F., Quénéhervé G., Hochschild V. and Maerker M. 2015. Multisensoral topsoil mapping in the semiarid Lake Manyara region, northern Tanzania. Remote Sensing 7:9563-9586.

Baldridge A., Hook S., Grove C. and Rivera G. 2009. The ASTER spectral library version 2.0. Remote Sens. Environ. 113:711-715.

Bartholomeus H., Schaepman M., Kooistra L., Stevens A., Hoogmoed W. and Spaargaren O. 2008. Spectral reflectance based indices for soil organic carbon quantification. Geoderma 145:28-36.

Basso B., Shuai G., Zhang J. and Robertson G.P. 2019. Yield stability analysis reveals sources of large-scale nitrogen loss from the US midwest. Scientific Reports 9:1-9.

Ben-Dor E. and Banin A. 1995. Near-infrared analysis as a rapid method to simultaneously evaluate several soil properties. Soil Sci. Soc. Am. J. 59:364-372.

Bennett H.H. 1948. Soil conservation. US Soil Conservation Service

Berhe A.A., Harte J., Harden J.W. and Torn M.S. 2007. The significance of the erosion-induced terrestrial carbon sink. Bioscience 57:337-346.

Bettis III E.A., Muhs D.R., Roberts H.M. and Wintle A.G. 2003. Last glacial loess in the conterminous USA. Quaternary Science Reviews 22:1907-1946.

Bureau of Land Management. "Land patent search." database and images. 2021

Cambardella C., Moorman T., Parkin T., Karlen D., Novak J., Turco R. and Konopka A. 1994. Field-scale variability of soil properties in central Iowa soils. Soil Sci. Soc. Am. J. 58:1501-1511.

Capehart W.J. and Carlson T.N. 1997. Decoupling of surface and near-surface soil water content: A remote sensing perspective. Water Resour. Res. 33:1383-1395.

Chang C., Laird D.A., Mausbach M.J. and Hurburgh C.R. 2001. Near-infrared reflectance spectroscopy–principal components regression analyses of soil properties. Soil Sci. Soc. Am. J. 65:480-490.

Chen F., Kissel D.E., West L.T. and Adkins W. 2000. Field-scale mapping of surface soil organic carbon using remotely sensed imagery. Soil Sci. Soc. Am. J. 64:746-753.

Chikhaoui M., Bonn F., Bokoye A.I. and Merzouk A. 2005. A spectral index for land degradation mapping using ASTER data: Application to a semi-arid mediterranean catchment. International Journal of Applied Earth Observation and Geoinformation 7:140-153.

Daily G.C., Matson P.A. and Vitousek P.M. 1997. Ecosystem services supplied by soil. Nature Services: Societal Dependence on Natural Ecosystems113-132.

De Vente J., Poesen J., Arabkhedri M. and Verstraeten G. 2007. The sediment delivery problem revisited. Prog. Phys. Geogr. 31:155-178.

Doetterl S., Berhe A.A., Nadeu E., Wang Z., Sommer M. and Fiener P. 2016. Erosion, deposition and soil carbon: A review of process-level controls, experimental tools and models to address C cycling in dynamic landscapes. Earth-Sci. Rev. 154:102-122.

Dogan H.M. and Kılıç O.M. 2013. Modelling and mapping some soil surface properties of Central Kelkit Basin in Turkey by using Landsat-7 ETM images. Int. J. Remote Sens. 34:5623-5640.

Escadafal R. 1993. Remote sensing of soil color: Principles and applications. Remote Sens. Rev. 7:261-279.

Farr T.G., Rosen P.A., Caro E., Crippen R., Duren R., Hensley S., Kobrick M., Paller M., Rodriguez E. and Roth L. 2007. The shuttle radar topography mission. Rev. Geophys. 45:.

Fenton T.E., Kazemi M. and Lauterbach-Barrett M.A. 2005. Erosional impact on organic matter content and productivity of selected iowa soils. Soil Tillage Res. 81:163-171.

Fernandes N.F. and Dietrich W.E. 1997. Hillslope evolution by diffusive processes: The timescale for equilibrium adjustments. Water Resour. Res. 33:1307-1318.

Food and Agriculture Organization of the United Nations. 2017. FAOSTAT statistics database. Fao.

Frazier, B.E., and Y. Cheng. 1989. Remote sensing of soils in the Eastern Palouse region with landsat thematic mapper. Remote Sens. Environ. 28: 317–325. doi: 10.1016/0034-4257(89)90123-5.

García-Ruiz J.M., Beguería S., Nadal-Romero E., González-Hidalgo J.C., Lana-Renault N. and Sanjuán Y. 2015. A meta-analysis of soil erosion rates across the world. Geomorphology 239:160-173.

Geological Survey, (U. S.). 2004. National hydrography dataset.

Gomez, C., R.A. Viscarra Rossel, and A.B. McBratney. 2008. Soil organic carbon prediction by hyperspectral remote sensing and field vis-NIR spectroscopy: An Australian case study. Geoderma 146(3–4): 403–411. doi: 10.1016/j.geoderma.2008.06.011.

Govers G., Quine T.A., Desmet P.J. and Walling D.E. 1996. The relative contribution of soil tillage and overland flow erosion to soil redistribution on agricultural land. Earth Surf. Process. Landforms 21:929-946.

Gran K.B., Belmont P., Day S.S., Jennings C., Johnson A., Perg L. and Wilcock P.R. 2009. Geomorphic evolution of the le sueur river, minnesota, USA, and implications for current sediment loading. Management and Restoration of Fluvial Systems with Broad Historical Changes and Human Impacts: Geological Society of America Special Paper 451:119-130.

Guo, L., H. Zhang, T. Shi, Y. Chen, Q. Jiang, et al. 2019. Prediction of soil organic carbon stock by laboratory spectral data and airborne hyperspectral images. Geoderma 337: 32–41. doi: 10.1016/j.geoderma.2018.09.003.

Guo L.B. and Gifford R.M. 2002. Soil carbon stocks and land use change: A meta analysis. Global Change Biol. 8:345-360.

Hernández D.L., Esch E.H., Alster C.J., McKone M.J. and Camill P. 2013. Rapid accumulation of soil carbon and nitrogen in a prairie restoration chronosequence. Soil Sci. Soc. Am. J. 77:2029-2038.

Huete A. and Escadafal R. 1991. Assessment of biophysical soil properties through spectral decomposition techniques. Remote Sens. Environ. 35:149-159.

Horowitz J.K., Ebel R.M. and Ueda K. 2010. No title. " No-Till" Farming is a Growing Practice.

Jelinski N.A. and Yoo K. 2016. The distribution and genesis of eroded phase soils in the conterminous united states. Geoderma 279:149-164.

Jelinski N.A., Campforts B., Willenbring J.K., Schumacher T.E., Li S., Lobb D.A., Papiernik S.K. and Yoo K. 2019. Meteoric beryllium-10 as a tracer of erosion due to postsettlement land use in west-central minnesota, USA. Journal of Geophysical Research: Earth Surface 124:874-901.

Johnson L.C. 1987. Soil loss tolerance: Fact or myth? J. Soil Water Conserv. 42:155-160.

Kemp D.B., Sadler P.M. and Vanacker V. 2020. The human impact on north american erosion, sediment transfer, and storage in a geologic context. Nature Communications 11:1-9.

Knox J.C. 1977. Human impacts on wisconsin stream channels. Ann. Assoc. Am. Geogr. 67:323-342.

Kumar P., Le P.V., Papanicolaou A.T., Rhoads B.L., Anders A.M., Stumpf A., Wilson C.G., Bettis III E.A., Blair N. and Ward A.S. 2018. Critical transition in critical zone of intensively managed landscapes. Anthropocene 22:10-19.

Lai J. and Anders A.M. 2018. Modeled postglacial landscape evolution at the southern margin of the laurentide ice sheet: Hydrological connection of uplands controls the pace and style of fluvial network expansion. Journal of Geophysical Research: Earth Surface 123:967-984.

Lal R., Griffin M., Apt J., Lave L. and Morgan M.G. 2004. Ecology. managing soil carbon. Science 304:393.

Lal R. 2005a. Soil Erosion and Carbon Dynamics.

Lal R. 2005b. Enhancing crop yields in the developing countries through restoration of the soil organic carbon pool in agricultural lands. Land Degrad. Dev. 17:197-209.

Lal R. 2004. Soil carbon sequestration impacts on global climate change and food security. Science 304:1623-1627.

Langdale G.W. and Shrader W.D. 1982. Soil erosion effects on soil productivity of cultivated cropland 1. Determinants of Soil Loss Tolerance41-51.

Larsen I.J., Montgomery D.R. and Greenberg H.M. 2014. The contribution of mountains to global denudation. Geology 42:527-530.

Li C., Fultz L.M., Moore-Kucera J., Acosta-Martínez V., Horita J., Strauss R., Zak J., Calderón F. and Weindorf D. 2017. Soil carbon sequestration potential in semi-arid grasslands in the conservation reserve program. Geoderma 294:80-90.

Li D., Chen X., Peng Z., Chen S., Chen W., Han L. and Li Y. 2012. Prediction of soil organic matter content in a litchi orchard of south China using spectral indices. Soil Tillage Res. 123:78-86.

Li H., Cruse R.M., Bingner R.L., Gesch K.R. and Zhang X. 2016. Evaluating ephemeral gully erosion impact on zea mays L. yield and economics using AnnAGNPS. Soil Tillage Res. 155:157-165.

Li L., Du S., Wu L. and Liu G. 2009. An overview of soil loss tolerance. Catena 78:93-99.

Li X., McCarty G.W., Karlen D.L. and Cambardella C.A. 2018. Topographic metric predictions of soil redistribution and organic carbon in iowa cropland fields. Catena 160:222-232.

Lilliefors H.W. 1969. On the Kolmogorov-Smirnov test for the exponential distribution with mean unknown. Journal of the American Statistical Association 64:387-389.

Lindstrom M.J., Nelson W.W., Schumacher T.E. and Lemme G.D. 1990. Soil movement by tillage as affected by slope. Soil Tillage Res. 17:255-264.

Lobell, D.B., and G.P. Asner. 2002. Moisture Effects on Soil Reflectance. SOIL SCI SOC AM J 66: 6.

McCarty G.W. and Reeves J.B. 2006. Comparison of near infrared and mid infrared diffuse reflectance spectroscopy for field-scale measurement of soil fertility parameters. Soil Sci. 171:94-102.

Minasny, B., A.B. McBratney, V. Bellon-Maurel, J.-M. Roger, A. Gobrecht, et al. 2011. Removing the effect of soil moisture from NIR diffuse reflectance spectra for the prediction of soil organic carbon. Geoderma 167–168: 118–124. doi: 10.1016/j.geoderma.2011.09.008.

Mishra U., Lal R., Slater B., Calhoun F., Liu D. and Van Meirvenne M. 2009. Predicting soil organic carbon stock using profile depth distribution functions and ordinary kriging. Soil Sci. Soc. Am. J. 73:614-621.

Montgomery D.R. 2007. Soil erosion and agricultural sustainability. Proc. Natl. Acad. Sci. U. S. A. 104:13268-13272.

Montgomery D.R. 2017. Growing a revolution: Bringing our soil back to life. WW Norton & Company

Montgomery D.R. 2012. Dirt: The erosion of civilizations. Univ of California Press.

Morgan R., Quinton J.N., Smith R.E., Govers G., Poesen J., Auerswald K., Chisci G., Torri D. and Styczen M.E. 1998. The european soil erosion model (EUROSEM): A dynamic approach for predicting sediment transport from fields and small catchments. Earth Surface Processes and Landforms: The Journal of the British Geomorphological Group 23:527-544.

Mulder V., De Bruin S., Schaepman M. and Mayr T. 2011. The use of remote sensing in soil and terrain mapping—A review. Geoderma 162:1-19.

Mulla D.J. 2013. Twenty five years of remote sensing in precision agriculture: Key advances and remaining knowledge gaps. Biosystems Engineering 114:358-371.

Nanni M.R. and Demattê J.A.M. 2006. Spectral reflectance methodology in comparison to traditional soil analysis. Soil Sci. Soc. Am. J. 70:393-407.

Nearing M.A., Foster G.R., Lane L.J. and Finkner S.C. 1989. A process-based soil erosion model for USDA-water erosion prediction project technology. Trans. ASAE 32:1587-1593.

Nearing M.A., Romkens M., Norton L.D., Stott D.E., Rhoton F.E., Laflen J.M., Flanagan D.C., Alonso C.V., Binger R.L. and Dabney S.M. 2000. Measurements and models of soil loss rates. Science 290:1300-1301.

Nearing M.A., Xie Y., Liu B. and Ye Y. 2017. Natural and anthropogenic rates of soil erosion. International Soil and Water Conservation Research 5:77-84.

Neigh C.S., Masek J.G. and Nickeson J.E. 2013. High-resolution satellite data open for government research. Eos, Transactions American Geophysical Union 94:121-123.

Nocita M., Stevens A., Noon C. and van Wesemael B. 2013. Prediction of soil organic carbon for different levels of soil moisture using vis-NIR spectroscopy. Geoderma 199:37-42.

Olson K.R., Norton L.D., Fenton T.E. and Lal R. 1994. Quantification of soil loss from eroded soil phases. J. Soil Water Conserv. 49:591-596.

Omernik J.M. 1987. Ecoregions of the conterminous United States. Ann. Assoc. Am. Geogr. 77:118-125.

Palacios-Orueta A. and Ustin S.L. 1998. Remote sensing of soil properties in the Santa Monica Mountains I. Spectral analysis. Remote Sens. Environ. 65:170-183.

Papiernik S.K., Schumacher T.E., Lobb D.A., Lindstrom M.J., Lieser M.L., Eynard A. and Schumacher J.A. 2009. Soil properties and productivity as affected by topsoil movement within an eroded landform. Soil Tillage Res. 102:67-77.

Peón, J., C. Recondo, S. Fernández, J. F. Calleja, E. De Miguel, et al. 2017. Prediction of Topsoil Organic Carbon Using Airborne and Satellite Hyperspectral Imagery. Remote Sens. 9(12): 1211. doi: 10.3390/rs9121211.

Pimentel D., Terhune E.C., Dyson-Hudson R., Rochereau S., Samis R., Smith E.A., Denman D., Reifschneider D. and Shepard M. 1976. Land degradation: Effects on food and energy resources. Science 194:149-155.

Pimentel D., Harvey C., Resosudarmo P., Sinclair K., Kurz D., McNair M., Crist S., Shpritz L., Fitton L. and Saffouri R. 1995. Environmental and economic costs of soil erosion and conservation benefits. Science-AAAS-Weekly Paper Edition 267:1117-1122.

Pimentel D. 2006. Soil erosion: A food and environmental threat. Environ. Dev. Sustainability 8:119-137.

Poesen J. 2017. Soil erosion in the anthropocene: Research needs. Earth Surf. Process. Landforms.

Ramankutty N. and Foley J.A. 1998. Characterizing patterns of global land use: An analysis of global croplands data. Global Biogeochem. Cycles 12:667-685.

Reeves D. 1997. The role of soil organic matter in maintaining soil quality in continuous cropping systems. Soil Tillage Res. 43:131-167.

Renard K.G., Foster G.R., Weesies G.A., McCool D.K. and Yoder D.C. 1997. Predicting soil erosion by water: A guide to conservation planning with the revised universal soil loss equation (RUSLE). United States Department of Agriculture Washington, DC.

Ritchie J.C., McCarty G.W., Venteris E.R. and Kaspar T.C. 2007. Soil and soil organic carbon redistribution on the landscape. Geomorphology 89:163-171.

Roger, J.-M., F. Chauchard, and V. Bellon-Maurel. 2003. EPO–PLS external parameter orthogonalisation of PLS application to temperature-independent measurement of sugar content of intact fruits. Chemom. Intell. Lab. Syst. 66(2): 191–204. doi: 10.1016/S0169-7439(03)00051-0.

Rossel R.V. and Behrens T. 2010. Using data mining to model and interpret soil diffuse reflectance spectra. Geoderma 158:46-54.

Rossel R.V., Walvoort D., McBratney A., Janik L.J. and Skjemstad J. 2006. Visible, near infrared, mid infrared or combined diffuse reflectance spectroscopy for simultaneous assessment of various soil properties. Geoderma 131:59-75.

Roy D.P., Wulder M., Loveland T.R., Woodcock C., Allen R., Anderson M., Helder D., Irons J., Johnson D. and Kennedy R. 2014. Landsat-8: Science and product vision for terrestrial global change research. Remote Sens. Environ. 145:154-172.

Sampson F. and Knopf F. 1994. Prairie conservation in north america. Other Publications in Wildlife Management41.

Sanderman J., Hengl T. and Fiske G.J. 2017. Soil carbon debt of 12,000 years of human land use. Proc. Natl. Acad. Sci. U. S. A. 114:9575-9580.

Schilling K.E. and Spooner J. 2006. Effects of watershed-scale land use change on stream nitrate concentrations. J. Environ. Qual. 35:2132-2145.

Schlesinger W.H. and Amundson R. 2019. Managing for soil carbon sequestration: Let's get realistic. Global Change Biol. 25:386-389.

Schulze, D. G., J. L. Nagel, G. E. Van Scoyoc, T. L. Henderson, M. F. Baumgardner, D.E. Stott 1993. Significance of Organic Matter in Determining Soil Colors. In: J. M. Bigham, E. J. Ciolkosz, editors, Soil Color, SSSA Spec. Publ. 31. SSSA, Madison, WI. p. 71-90. doi:10.2136/sssaspecpub31.c5

Schumacher J.A., Kaspar T.C., Ritchie J.C., Schumacher T.E., Karlen D.L., Venteris E.R., McCarty G.W., Colvin T.S., Jaynes D.B. and Lindstrom M.J. 2005. Identifying spatial patterns of erosion for use in precision conservation. J. Soil Water Conserv. 60:355-362

Sequeira C.H., Wills S.A., Grunwald S., Ferguson R.R., Benham E.C. and West L.T. 2014. Development and update process of VNIR-based models built to predict soil organic carbon. Soil Sci. Soc. Am. J. 78:903-913.

Skidmore E.L. 1982. Soil loss tolerance. Determinants of Soil Loss Tolerance 45:87-93.

Smith G.M. and Milton E.J. 1999. The use of the empirical line method to calibrate remotely sensed data to reflectance. Int. J. Remote Sens. 20:2653-2662.

Soil Science Division Staff. 2017. Soil survey manual. USDA Handbook 18120-131.

Soil Survey Staff. 1999. A basic system of soil classification for making and interpreting soil surveys. 2nd edition. national resource conservation service.

Soil Survey Staff. 2013 Rapid Carbon Assessment (RaCA) project. United States Department of Agriculture, Natural Resources Conservation Service. Available online. June 1, 2013 (FY2013 official release).

Soil Survey Staff. 2019. Gridded national soil survey geographic (gNATSGO) database for the conterminous united states.

Stallard R.F. 1998. Terrestrial sedimentation and the carbon cycle: Coupling weathering and erosion to carbon burial. Global Biogeochem. Cycles 12:231-257.

Steiner F. 1987. Soil conservation policy in the united states. Environ. Manage. 11:209-223.

Stevens A., Udelhoven T., Denis A., Tychon B., Lioy R., Hoffmann L. and Van Wesemael B. 2010. Measuring soil organic carbon in croplands at regional scale using airborne imaging spectroscopy. Geoderma 158:32-45.

Stoner E.R. and Baumgardner M. 1981. Characteristic variations in reflectance of surface soils 1. Soil Sci. Soc. Am. J. 45:1161-1165.

Thaler E.A., Larsen I.J. and Yu Q. 2019. A new index for remote sensing of soil organic carbon based solely on visible wavelengths. Soil Sci. Soc. Am. J. 83:1443-1450.

Thaler, E.A., I.J. Larsen, and Q. Yu. 2021. The extent of soil loss across the US Corn Belt. Proc. Natl. Acad. Sci. 118(8): e1922375118. doi: 10.1073/pnas.1922375118.

Tilman D., Cassman K.G., Matson P.A., Naylor R. and Polasky S. 2002. Agricultural sustainability and intensive production practices. Nature 418:671.

Tomer M.D., James D.E. and Sandoval-Green C.M. 2017. Agricultural conservation planning framework: 3. land use and field boundary database development and structure. J. Environ. Qual. 46:676-686.

Trimble S.W. 1981. Changes in sediment storage in the coon creek basin, driftless area, Wisconsin, 1853 to 1975. Science 214:181-183.

Trimble S.W. and Lund S.W. 1982. Soil conservation and the reduction of erosion and sedimentation in the coon creek basin, wisconsin. US Government Printing Office,

Turner R.E. and Rabalais N.N. 1994. Coastal eutrophication near the mississippi river delta. Nature 368:619.

Trimble S.W. and Crosson P. 2000. U.S. soil erosion rates--myth and reality. Science 289:248-250.

U.S. Department of Agriculture. 2018. Summary report: 2015 national resources inventory, natural resources conservation service, washington, DC, and center for survey statistics and methodology, iowa state university, ames, iowa. http://Www.nrcs.usda.gov/technical/nri/15summary.

U.S. Department of Agriculture. 2017. Crop production. Rep. ISSN:1936-3737.

U.S. Department of Agriculture. Economic research service. tillage intensity and conservation cropping in the united states, EIB-197.

U.S. Department of Agriculture. 2017. Crop production. Rep. ISSN:1936-3737.

U.S. Geological Survey. 2014. USGS national transportation dataset .

Van Oost K., Quine T.A., Govers G., De Gryze S., Six J., Harden J.W., Ritchie J.C., McCarty G.W., Heckrath G., Kosmas C., Giraldez J.V., da Silva J.R. and Merckx R. 2007. The impact of agricultural soil erosion on the global carbon cycle. Science 318:626-629.

Van Oost K., Govers G., De Alba S. and Quine T.A. 2006. Tillage erosion: A review of controlling factors and implications for soil quality. Prog. Phys. Geogr. 30:443-466.

Vanacker V., von Blanckenburg F., Govers G., Molina A., Poesen J., Deckers J. and Kubik P. 2007. Restoring dense vegetation can slow mountain erosion to near natural benchmark levels. Geology 35:303-306.

Viscarra Rossel, R.A., D.J.J. Walvoort, A.B. McBratney, L.J. Janik, and J.O. Skjemstad. 2006. Visible, near infrared, mid infrared or combined diffuse reflectance spectroscopy for simultaneous assessment of various soil properties. Geoderma 131(1–2): 59–75. doi: 10.1016/j.geoderma.2005.03.007.

Wang Z., Hoffmann T., Six J., Kaplan J.O., Govers G., Doetterl S. and Van Oost K. 2017. Human-induced erosion has offset one-third of carbon emissions from land cover change. Nature Climate Change 7:345-349.

Weidong L., Baret F., Xingfa G., Qingxi T., Lanfen Z. and Bing Z. 2002. Relating soil surface moisture to reflectance. Remote Sens. Environ. 81:238-246.

West T.O. and Post W.M. 2002. Soil organic carbon sequestration rates by tillage and crop rotation. Soil Sci. Soc. Am. J. 66:1930-1946.

Weyer P.J., Cerhan J.R., Kross B.C., Hallberg G.R., Kantamneni J., Breuer G., Jones M.P., Zheng W. and Lynch C.F. 2001. Municipal drinking water nitrate level and cancer risk in older women: The iowa women's health study. Epidemiology327-338.

Wijewardane N.K., Ge Y., Wills S. and Loecke T. 2016. Prediction of soil carbon in the conterminous United States: Visible and near infrared reflectance spectroscopy analysis of the rapid carbon assessment project. Soil Sci. Soc. Am. J. 80:973-982.

Wijewardane, N.K., Y. Ge, and C.L.S. Morgan. 2016. Moisture insensitive prediction of soil properties from VNIR reflectance spectra based on external parameter orthogonalization. Geoderma 267: 92–101. doi: 10.1016/j.geoderma.2015.12.014.

Wills S., Loecke T., Sequeira C., Teachman G., Grunwald S. and West L.T. 2014. Overview of the US rapid carbon assessment project: Sampling design, initial summary and uncertainty estimates. p. 95-104. *In* Overview of the US rapid carbon

assessment project: Sampling design, initial summary and uncertainty estimates. Soil carbon. Springer

Woodruff N.P. and Siddoway F.H. 1965. A wind erosion equation. Soil Sci. Soc. Am. J. 29:602-608.

Wu, C.-Y., A.R. Jacobson, M. Laba, and P.C. Baveye. 2009. Alleviating Moisture Content Effects on the Visible Near-Infrared Diffuse-Reflectance Sensing of Soils. Soil Sci. 174(8). https://journals.lww.com/soilsci/Fulltext/2009/08000/Alleviating_Moisture_Content_Effects_on_the.6.aspx.